

Analysis of ATOFMS datasets for apportionment of PM_{2.5} in California

Final Report to California Air Resources Board
Contract No. 07-357

Prepared for the California Air Resources Board and the California
Environmental Protection Agency

May 15, 2010

Principal Investigator

Kimberly Prather

Contributors

Andrew P. Ault

Cassandra Gaston

Kerri A. Pratt

Steve M. Toner

Department of Chemistry & Biochemistry
University of California San Diego
9500 Gilman Drive MC 0314
La Jolla, CA 92093-0314

DISCLAIMER

1 The statements and conclusions in this Report are those of the contractor and not
2 necessarily those of the California Air Resources Board. The mention of commercial
3 products, their source, or their use in connection with material reported herein is not to be
4 construed as actual or implied endorsement of such products.

5

6

7

8

ACKNOWLEDGEMENTS

9
10
11
12
13
14
15
16
17
18

We thank Drs. William Vance and Eileen McCauley (CARB) for their assistance and advice during this contract.

This Report was submitted in fulfillment of Contract No. 07-357, “Analysis of ATOFMS datasets for apportionment of PM_{2.5} in California” under the sponsorship of the California Air Resources Board. Work was completed as of May 15, 2010.

19
20
21
22
23
24
25
26
27
28
29
30
31
32
33
34
35
36
37
38
39
40
41
42
43
44
45
46
47
48
49
50
51
52
53
54
55
56
57
58
59
60
61
62
63
64
65
66
67
68
69

TABLE OF CONTENTS

DISCLAIMER	2
ACKNOWLEDGEMENTS	3
TABLE OF CONTENTS	4
LIST OF FIGURES	6
ABSTRACT	8
EXECUTIVE SUMMARY	9
Background:.....	9
Methods:.....	9
Results and Conclusions:.....	9
Applying the ATOFMS technique to new research topics was a focus of this report. Methanesulfonic acid (MSA) is formed from the oxidation of dimethyl sulfide (DMS) and since it does not have an anthropogenic source it is an ideal marker for ocean-derived biogenic sulfur. MSA was observed at an inland location (Riverside) and the high levels observed may have been due, in part, to vanadium in mixed particles catalyzing MSA formation. In Riverside organic carbon often is a significant fraction of the particles observed by ATOFMS measurements and secondary species such as ammonium nitrate, ammonium sulfate, and amines account for >50% by of these organic carbon particles. Analysis of thermal denuder – ATOFMS measurements shows that at 230 °C particle spectra resemble those of freshly emitted particles as secondary species are vaporized. This allows sources to be determined even in highly aged environments. Using the ATOFMS sources library shows that in 2 urban areas outside of California (Athens, Greece and Mexico City, Mexico) dust and biomass burning are significant sources of atmospheric particles. In the larger Mexico City the particles are observed to be more aged with secondary species. The research shown in this report displays the broad applicability of ATOFMS studies to tackle a multitude of different areas of interest in air quality and climate studies.....	9
BODY OF REPORT	11
A. Introduction.....	11
1. <i>Research Objectives</i>	11
2. <i>Summary of Chapters</i>	11
i. Introduction.....	11
ii. Materials and Methods.....	11
iii. Results and Conclusions.....	11
B. Materials and Methods.....	12
1. <i>Instrumentation</i>	12
3. <i>Data Analysis Methods</i>	16
C. Results.....	19
1. <i>Real-time detection and mixing state of methanesulfonate in single particles at an inland urban location during a phytoplankton bloom</i>	19
i. Introduction.....	19
iii. Results and Discussion.....	22
iv. Acknowledgements.....	33
2. <i>Real-time, single-particle volatility, size, and chemical composition measurements of aged urban aerosols</i>	34
i. Introduction.....	34
ii. Experimental.....	35
iii. Results and Discussion.....	36
iv. Acknowledgements.....	55
3. <i>Source apportionment of PM_{2.5} in Athens (Greece) and Mexico City using an ATOFMS derived mass spectral source library</i>	56
i. Introduction.....	56
ii. Experimental.....	57
iii. Results and Discussion.....	58

70	iv. Acknowledgements.....	73
71	D. References.....	74
72	E. Publications produced	88
73		
74		
75		
76		
77		
78		

LIST OF FIGURES

79		
80	Figure 1: Instrument schematic diagrams of the (a) ATOFMS and (b) UF-ATOFMS.	14
81	Figure 2: (a) Schematic of the A-ATOFMS illustrating the dometop alignment interface, aerodynamic	
82	sizing region, desorption/ ionization laser alignment, and dual-polarity Z-TOF mass spectrometer. (b)	
83	Schematic of dual polarity Z-TOF mass spectrometer illustrating ion extraction region and ion	
84	trajectory.	16
85	Figure 3: Average positive and negative ion mass spectra for the OC-V-sulfate particle type containing	
86	MSA (m/z -95) during SOAR-1.	23
87	Figure 4: (a) Time series showing the fraction of MSA-containing submicron (red line) and supermicron	
88	(blue line) particles during SOAR-1 and chlorophyll concentrations (green line) taken from the	
89	Newport Beach station (33.6°N, 117.9°W) at 3 m depth. Gaps in chlorophyll data occur from August	
90	2-4. Inset shows typical HYSPLIT 48 hour back-trajectories for air masses arriving to the sampling	
91	site during different time periods in addition to the locations of the automated chlorophyll stations.	
92	Each trajectory is taken at 500 m altitude, and each point on the trajectory corresponds to a 12-hour	
93	increment. (b) Time series showing the corresponding wind speed (black line) and direction (pink	
94	line).	24
95	Figure 5: Chlorophyll data at 3 m depth from the Newport Beach (33.6°N, 117.9°W) and SIO Pier	
96	(32.87°N, 117.3°W) automated stations. Inset is chlorophyll data measured at the surface of the SIO	
97	Pier.	25
98	Figure 6: MSA-containing particle types plotted as a function of size. Submicron (0.2-1.0 μm) particles are	
99	plotted in 0.05 μm bins while supermicron (1.0-3.0 μm) particles are plotted in 0.1 μm bins.	27
100	Figure 7: Size distributions of all hit particles (black line) during SOAR-1 and only MSA-containing	
101	particles (blue line).	28
102	Figure 8: Temporal profile of ATOFMS counts of submicron MSA- (red line), HMS- (green line), sulfate-	
103	(black line) and V- (brown line) containing particles. Relative humidity (RH) is also shown (dashed	
104	blue line).	29
105	Figure 9: Average peak area of MSA (m/z -95) for MSA-containing submicron particle types mixed with V	
106	(light blue triangles) and submicron particles containing no V (orange triangles) are shown in the top	
107	panel. The average peak area of MSA on supermicron particles containing V (dark blue diamonds)	
108	and containing no V (red diamonds) are shown in the bottom panel. The vertical bars correspond to	
109	95% confidence intervals associated with the peak areas.	31
110	Figure 10: Representative average aged sea salt positive and negative ion mass spectra of particles (a)	
111	mixed with and (b) without V.	32
112	Figure 11: Size-resolved chemical composition of a) unheated and b) 230°C heated particles. Size	
113	resolution is 10 nm and 50 nm for the ranges of 100-350 nm and 350-1000 nm, respectively.	
114	Relative fractions of 230°C particle cores are illustrated for c) 100-150 nm, d) 200-250 nm, and e)	
115	750-800 nm.	37
116	Figure 12: Average ATOFMS representative mass spectra and size-resolved number concentrations of	
117	unheated and 230°C heated particles for a) aged OC, b) EC, c) vanadium, and d) biomass burning	
118	particle classes.	38
119	Figure 13: Average ATOFMS representative mass spectra and size-resolved number concentrations of	
120	unheated and 230°C heated particles for the following particle types: a) aromatic, b) amine, c)	
121	ammonium-rich, d) ECOC, e) inorganic-ECOC, f) aged sea salt, g) dust, h) metals (Zn-rich shown).	
122	A size distribution is not shown for the ammonium-rich particle class due to low ATOFMS particle	
123	counts.	41
124	Figure 14: Representative average positive and negative mass spectra of 230°C heated particles for four	
125	metal-rich particle types: a) Ba-rich, b) Pb-rich, c) Mo-rich, and d) Sn-rich.	43
126	Figure 15: Average size-resolved number concentrations with ~50 nm size bins ($d_{va} = 103-995$ nm) as	
127	measured by the SMPS from Nov. 2-13 for ambient temperature to 230°C. Variation over the course	
128	of the study is shown by standard error bars.	43
129	Figure 16: a) Size-resolved number concentrations of unheated and heated (54-230°C) aged OC particles.	
130	b) Fractions of ammonium, nitrate, and sulfate remaining at different TD temperatures (54-230°C)	
131	for aged OC particles with respect to the vaporization temperature ranges of ammonium nitrate (94)	
132	and ammonium sulfate (72).	44

133	Figure 17: a) Size-resolved number concentrations of unheated and heated (54-230°C) vanadium-	
134	containing particles. b) Fractions of ammonium, nitrate, and sulfate at different TD temperatures (54-	
135	230°C) for vanadium-containing particles with respect to the vaporization temperature ranges of	
136	ammonium nitrate (94) and ammonium sulfate (72).....	46
137	Figure 18: a) Size-resolved number concentrations of unheated and heated (54-230°C) biomass burning	
138	particles. b) Fractions of ammonium, nitrate, and sulfate at different TD temperatures (54-230°C) for	
139	biomass burning particles with respect to the vaporization temperature ranges of ammonium nitrate	
140	(94) and ammonium sulfate (72).....	47
141	Figure 19: Fractions of ammonium, nitrate, and sulfate at different TD temperatures (54-230°C) for a) aged	
142	sea salt and b) dust particles with respect to the vaporization temperature ranges of ammonium nitrate	
143	(94) and ammonium sulfate (72).....	48
144	Figure 20: Size-resolved chemical composition for the 13 general particle types for: a) unheated, b) 54°C,	
145	c) 83°C, d) 113°C, e) 142°C, f) 171°C, g) 201°C, and h) 230°C. Size resolution is 10 nm and 50 nm	
146	for the ranges of 100-350 nm and 350-1000 nm, respectively.....	51
147	Figure 21: Dot product comparisons of mass spectral signatures of freshly emitted source particles (light	
148	duty vehicles (LDV), heavy duty diesel vehicles (HDDV), wildfire, sea salt, and dust) with unheated	
149	and 230°C heated SOAR-2 particles.....	54
150	Figure 22: Temporal series of the mass spectral source library matching results for Athens, Greece ambient	
151	A) submicron particles; and B) supermicron particles.....	60
152	Figure 23: Percent of Athens, Greece particles matched to the mass spectral source library at different	
153	match-ART-2a Vigilance Factors (VF)	62
154	Figure 24: Size resolved source apportionment of the ATOFMS detected ambient particles for Athens,	
155	Greece.	62
156	Figure 25: The top matching mass spectral source signatures for each source for Athens, Greece ATOFMS	
157	data.....	64
158	Figure 26: The top matching non-source specific mass spectral signatures for each type for Athens, Greece	
159	ATOFMS data.....	65
160	Figure 27: Temporal series of the mass spectral source library matching results for Mexico City ambient A)	
161	submicron particles; and B) supermicron particles.	66
162	Figure 28: Percent of Mexico City particles matched to the mass spectral source library at different match-	
163	ART-2a Vigilance Factors (VF).	68
164	Figure 29: Size resolved source apportionment of the ATOFMS detected ambient particles for Mexico City.	
165	68
166	Figure 30: The top matching mass spectral source signatures for each source for Mexico City ATOFMS	
167	data.....	70
168	Figure 31: The top matching non-source specific mass spectral signatures for each type for Mexico City	
169	ATOFMS data.....	71
170		
171		
172		

173

ABSTRACT

174

175

176

177

178

179

180

181

182

183

184

185

186

187

188

189

190

191

192

193

194

195

196

The development of aerosol time-of-flight mass spectrometry (ATOFMS) as a source apportionment tool for atmospheric particulate matter using California Air Resources Board funding has focused on the differentiation of sources by identifying the unique mass spectra of single particles produced in source tests and the atmosphere. By acquiring both the positive and negative spectra of each particle, significant progress has been made in quantifying the contributions from both natural and anthropogenic particles that impact California air quality. Specifically, studies have shown how heavy duty diesel vehicles, gasoline vehicles, biomass burning, ships, sea spray, and dust impact air quality in many regions. This report details efforts to expand the boundaries for on-line chemical analysis methods, such as ATOFMS, that will allow their general implementation in many areas in an effort to increase our understanding of particle sources and processes in the atmosphere. A major focus of one project in this report involves investigating the sources of sulfate and the interplay between anthropogenic and biogenic sources of SO₂, sulfate, and particle mass concentrations. To investigate the primary sources of PM, the results of tandem thermal denuder-ATOFMS measurements are described that give information on the volatility and fractions of secondary components within the aerosol including sulfate, nitrate, and organic carbon species. Lastly, the application of the source library that has been developed to match studies to specific sources is tested in two urban areas outside of California to show the broad applicability of this method for source apportionment. Taken together the results of this report demonstrate the level of new information on particle sources that on-line mass spectrometry can provide when applied in new and innovative ways.

EXECUTIVE SUMMARY

198 ***Background:***

199 Aerosol time-of-flight mass spectrometry data provide a complex picture of
200 particle mixing state providing new insights into the major sources and processes
201 impacting particulate matter concentrations. Herein, we focus on unraveling the impact of
202 biogenic contributions to California's sulfate loading that has been difficult to isolate
203 from anthropogenic contributions. One unique finding involves the detection of
204 methanesulfonic acid (MSA), sulfate, and the highlighted the catalytic role of metals on
205 enhanced sulfate formation. Surprisingly, MSA was shown to be a dominant component
206 of aerosols at an inland urban location in Riverside, CA, showing biogenic sources of
207 sulfate can contribute significantly to PM mass concentrations particularly during periods
208 with large oceanic blooms. The relative contributions from secondary species, such as
209 sulfate, are difficult to study due to their transient nature, but results presented herein
210 explore secondary species such as ammonium sulfate, ammonium nitrate, and organic
211 carbon. This was achieved through thermal denuder/ATOFMS measurements. Lastly,
212 improving our ability to accurately apportion ATOFMS data is an ongoing goal of our
213 research and study data from Mexico City, Mexico and Athens, Greece were used to
214 validate source matching software developed in source and ambient studies conducted in
215 California.

216 ***Methods:***

217 ATOFMS was the primary instrument utilized in the studies discussed below.
218 Additional techniques utilized in these studies include gas phase instrumentation (SO₂,
219 NO_x, CO, O₃) and particle phase instrumentation (SMPS, APS, CPC, aethalometer, and
220 TEOM). In addition, data were used from CARB monitoring stations, mostly from the
221 Rubidoux site. One portion of this report focuses on results from tandem measurements
222 with a thermal denuder interfaced with an ATOFMS.

223 ***Results and Conclusions:***

224 Applying the ATOFMS technique to new research topics was a focus of this project.
225 Methanesulfonic acid (MSA) is formed from the oxidation of dimethylsulfide (DMS).
226 DMS is an ideal tracer for ocean-derived biogenic sulfur. MSA was observed at an inland
227 location (Riverside) and the high levels observed may have been due, in part, to
228 vanadium in mixed particles emitted from ships burning bunker oil catalyzing MSA
229 formation. In Riverside, organic carbon often represents a significant fraction of the
230 particles observed by ATOFMS measurements and secondary species such as ammonium
231 nitrate, ammonium sulfate, and amines account for >50% by of these particles. Analysis
232 of thermal denuder – ATOFMS measurements shows that at 230 °C particle spectra
233 resemble those of freshly emitted primary particles as secondary species are vaporized.
234 This thermal denuder approach allows sources to be determined even in highly aged
235 environments. Using the ATOFMS source library shows that in two urban areas outside
236 of California (Athens, Greece and Mexico City, Mexico), dust and biomass burning
237 represent significant sources of atmospheric particles. In Mexico City, the particles are
238 observed to be more aged, containing large fractions of secondary species. The research

239 shown in this report displays the broad applicability of ATOFMS studies to address many
240 different areas of interest in air quality and climate studies. Given the recent emphasis on
241 long range transport of pollutants through our atmosphere, understanding different
242 sources on a more global scale is an area of increasing importance.

243

244

245

BODY OF REPORT

246 *A. Introduction*

247 **1. Research Objectives**

248 This project focused on a number of data analysis tasks that were identified as
249 ways to gain as much value out of the investment in aerosol time-of-flight mass
250 spectrometer (ATOFMS) field study data that the Air Resources Board has made over the
251 past decade. One task involved investigating methanesulfonic acid (MSA), sulfate, and
252 the potential catalytic effects of metals on formation processes. A second objective was to
253 explore secondary species such as ammonium sulfate, ammonium nitrate, and organic
254 carbon. This was achieved through thermal denuder/ATOFMS measurements. Lastly, to
255 test the general applicability of the source data, field data from Mexico City, Mexico and
256 Athens, Greece were used to validate the source matching script to allow for quick and
257 accurate apportionment of field study data in a non-California location.

258 **2. Summary of Chapters**

259 **i. Introduction**

260 Chapter 1 introduces the goals of the project and motivation behind them, as well
261 as the objectives and deliverables provided within the report. The aerosol time-of-flight
262 mass spectrometer is then introduced as well as the trailer that was developed to transport
263 it during this project. Previously developed as well as novel data analysis techniques are
264 then described. Lastly, a brief summary of each chapter of the report is included.

265 **ii. Materials and Methods**

266 The aerosol time-of-flight mass spectrometer is introduced. The application of
267 previously developed data analysis techniques is described.

268 **iii. Results and Conclusions**

269 Chapter 1 discusses methanesulfonic acid (MSA). Dimethyl sulfide (DMS),
270 produced by oceanic phytoplankton, is oxidized to form methanesulfonic acid (MSA) and
271 sulfate, which influence particle chemistry and hygroscopicity. Unlike sulfate, MSA has
272 no known anthropogenic sources making it a useful tracer for ocean-derived biogenic
273 sulfur. Despite numerous observations of MSA, predominately in marine environments,
274 the production pathways of MSA have remained elusive highlighting the need for
275 additional measurements, particularly at inland locations. During the Study of Organic
276 Aerosols in Riverside, CA from July-August 2005 (SOAR-1), MSA was detected in
277 submicron and supermicron particles using real-time, single-particle mass spectrometry.
278 MSA was detected due to blooms of DMS-producing organisms along the California
279 coast. The detection of MSA depended on both the origin of the sampled air mass as well
280 as the concentration of oceanic chlorophyll present. MSA was mainly mixed with
281 coastally emitted particle types implying that partitioning of MSA occurred before
282 transport to Riverside. Importantly, particles containing vanadium had elevated levels of
283 MSA compared to particles not containing vanadium, suggesting a possible catalytic role

284 of vanadium in MSA formation. This study demonstrates how anthropogenic, metal-
285 containing aerosols can enhance the atmospheric processing of biogenic emissions, which
286 need to be considered when modeling coastal as well as urban locations.

287 Chapter 2 described how aerosol particles undergo significant atmospheric
288 processing within the Los Angeles basin. To assess the major sources and extent of
289 aging, ambient particle volatility, size, and chemical composition were measured
290 concurrently in real-time during the Study of Organic Aerosols conducted in Riverside,
291 CA in November 2005. A thermal denuder (TD) was coupled to an aerosol time-of-flight
292 mass spectrometer (ATOFMS) to characterize the chemistry of the individual submicron
293 particle cores remaining after heating. At 230°C, aged organic carbon (OC) particles had
294 smaller particle cores (mode <100 nm) compared to biomass burning particles (~180
295 nm). Aged OC particles contained >50% by volume secondary species, primarily
296 ammonium nitrate, ammonium sulfate, and amines. At 230°C, the chemistry of the
297 remaining cores at 100-150 nm were elemental carbon (29% by number), OC (27%), and
298 biomass burning (15%). Sea salt (47%) and dust (15%) were the major contributors at
299 the larger sizes (750-800 nm). Many particle cores at 230°C possessed similar signatures
300 to fresh vehicle emissions, biomass burning, sea salt, and dust particles, showing that the
301 TD-ATOFMS method can be used to apportion particles in highly aged environments to
302 their original sources, while providing insight into the relative contributions of primary
303 and secondary species.

304 Chapter 3 discusses how using a variation of the ART-2a algorithm along with an
305 aerosol time-of-flight mass spectrometry (ATOFMS) derived mass spectral source
306 library, source apportionment of ambient aerosols for two major global cities (Athens,
307 Greece and Mexico City, Mexico) was carried out. From these results, it was found that
308 the ambient primary aerosols at both locations show a strong influence from biomass
309 burning and dust. The Athens site also shows strong contributions from both diesel and
310 gasoline powered vehicle emissions, sea salt, and a combination of elemental carbon and
311 vanadium particles that could be due to ship emissions. While the aerosols at both sites
312 show signs of aging and associations with secondary organic carbon, nitrate, sulfate, and
313 ammonium, the Mexico City site was found to have more aged aerosols than Athens, and
314 (along with biomass burning and dust) shows contributions from diesel and gasoline
315 vehicle emissions, industrial emissions, meat cooking, and non-source specific amines,
316 PAH's, aged organic and elemental carbon. The results obtained with the source
317 signature matching technique are compared to general particle classification results and
318 show that the source signature matching technique is applicable to worldwide ambient
319 ATOFMS data.

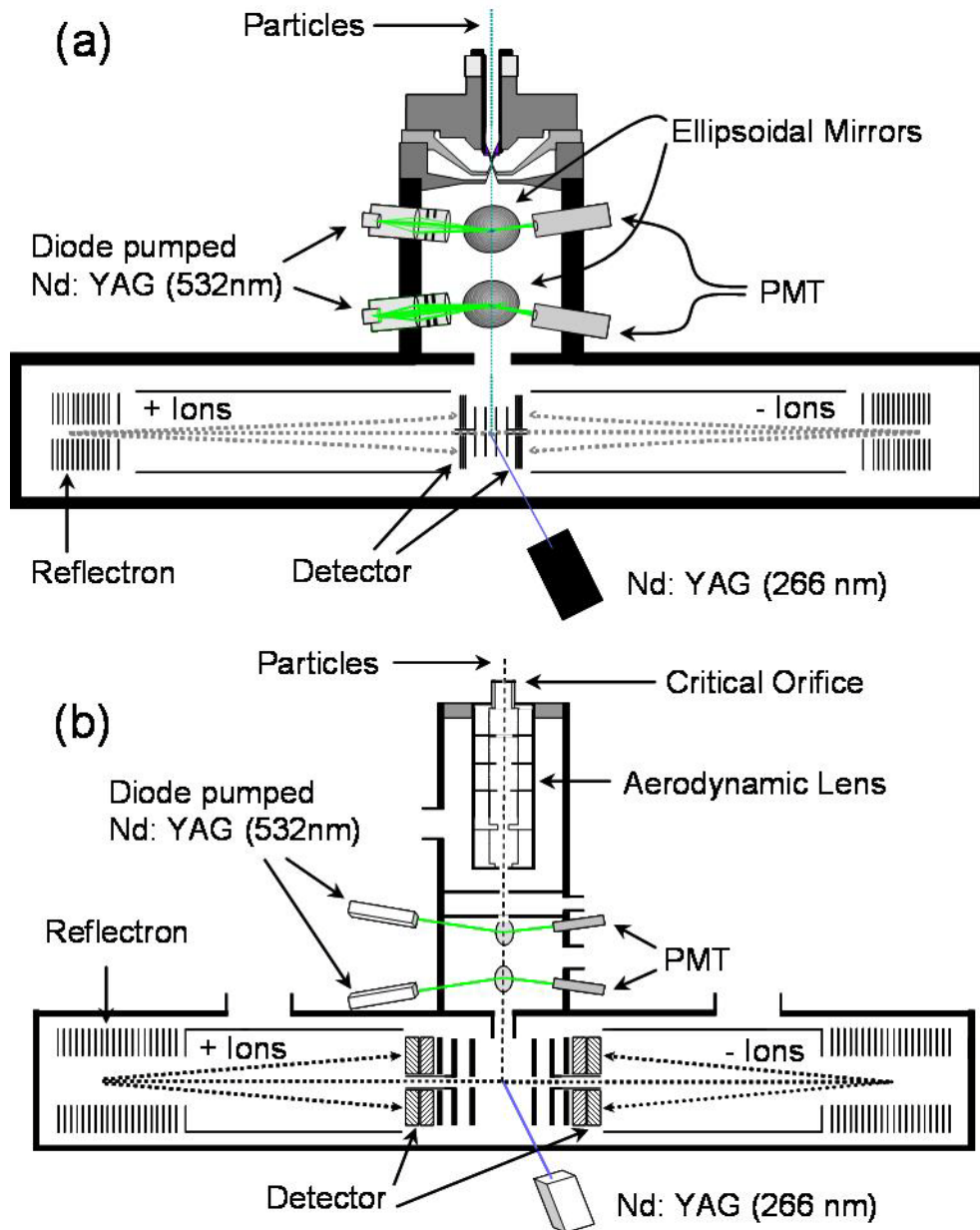
320

321 ***B. Materials and Methods***

322 **1. Instrumentation**

323 The principal sampling technique for ambient particles used throughout this
324 dissertation is aerosol time-of-flight mass spectrometry (ATOFMS). ATOFMS
325 simultaneously acquires positive and negative ion spectra, as well as size information, for
326 single particles in real-time. A detailed description of operation and performance of the
327 transportable version of this instrument has been provided previously (1), though a brief

328 explanation is included here. A schematic diagram of the standard inlet ATOFMS is
329 given in Figure 1. The inlet region consists of a converging nozzle, followed by two
330 skimmers. Similar to the APS, the particles undergo supersonic expansion upon
331 introduction into vacuum and are accelerated to velocities dependent on their
332 aerodynamic sizes. The different regions separated by skimmers fulfill two primary
333 functions: to permit differential pumping from atmospheric pressures to the pressures
334 necessary to operate the mass spectrometer and to collimate the particle beam by
335 removing those particles which do not follow a straight trajectory. The particle beam next
336 enters the light-scattering region, which includes two continuous-wave 532 nm diode
337 pumped Nd:YAG lasers. These lasers are positioned orthogonally to the particle beam, so
338 that when a particle passes through the laser beam, its scattered light is focused onto
339 PMTs by means of ellipsoidal mirrors. The PMTs send pulses to an electronic timing
340 circuit that measures the time the particle takes to travel the known distance (6 cm)
341 between the two laser beams. The velocity of the particle is calculated with the particle
342 time of flight and the distance and is converted to a physical aerodynamic diameter via an
343 external size calibration with particles of known size. With the determined particle
344 velocity, the timing circuit counts down to when the tracked particle will reach the center
345 of the ion source region of the mass spectrometer and sends a signal to a pulsed Nd:YAG
346 laser (frequency quadrupled to 266 nm) to fire. Through direct laser desorption/ionization
347 (LDI), the laser pulse produces ions, which are then mass analyzed in a dual-ion
348 reflectron time-of-flight mass spectrometer. The dual polarity permits simultaneous
349 acquisition of positive and negative ion spectra for an individual particle, which is unique
350 as most SPMS techniques can only obtain spectra of single polarity at a given time. The
351 standard ATOFMS instrument can analyze single particles with aerodynamic diameters
352 over a broad size range from approximately 200 to 3000 nm.



353

354

Figure 1: Instrument schematic diagrams of the (a) ATOFMS and (b) UF-ATOFMS.

355

356

357

358

359

360

361

362

363

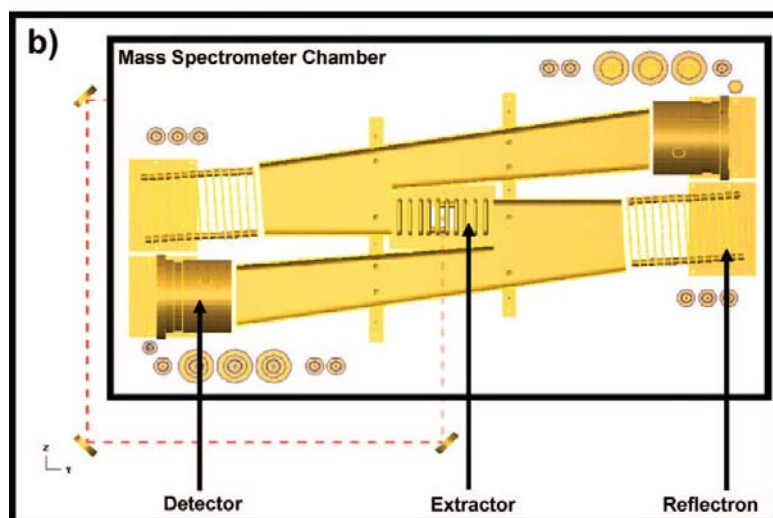
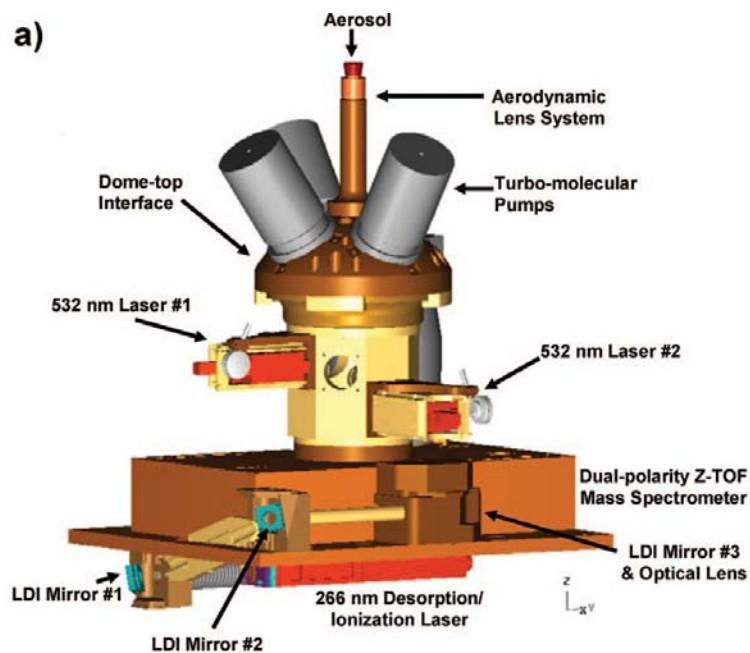
364

365

Ultrafine aerosol time-of-flight mass spectrometry (UF-ATOFMS) has improved detection efficiency for small particles (< 300 nm) over the standard ATOFMS by replacing the converging nozzle inlet with an aerodynamic lens inlet (2). Figure 1b shows the schematic diagram of the UF-ATOFMS instrument. The lens system tightly collimates the particle beam, so that smaller ultrafine particles will be more efficiently transmitted in the instrument (3-4). Upon exiting the aerodynamic lens, the gas molecules undergo supersonic expansion, accelerating the particles to terminal velocities based on their aerodynamic diameter – just as with standard inlet ATOFMS. UF-ATOFMS also has enhanced light-scattering detection by incorporating a focusing lens to tighten the continuous laser beams, increasing the laser beam power density, and by employing a fast amplifier to improve the signal-to-noise ratio. All of these

366 enhancements, in addition to the aerodynamic lens systems, are necessary to improve the
367 minimum optical detection size of ~100 nm down to 50 nm. Together, standard
368 ATOFMS and UF-ATOFMS cover an aerodynamic size range of ~50 to 3000 nm when
369 sampling side-by-side.

370 To gain further insight into the size-resolved chemistry of individual atmospheric
371 particles, a smaller aerosol time-of-flight mass spectrometer (ATOFMS) with increased
372 data acquisition capabilities was developed for aircraft-based studies (5). Compared to
373 previous ATOFMS systems, the new instrument has a faster data acquisition rate with
374 improved ion transmission and mass resolution, as well as reduced physical size and
375 power consumption (Figure 2). In addition, real-time source apportionment software
376 allows the immediate identification and classification of individual particles to guide
377 sampling decisions while in the field. The aircraft (A)-ATOFMS was field-tested on the
378 ground during the Study of Organic Aerosols in Riverside, CA (SOAR).



379
380
381
382

Figure 2: (a) Schematic of the A-ATOFMS illustrating the dometop alignment interface, aerodynamic sizing region, desorption/ ionization laser alignment, and dual-polarity Z-TOF mass spectrometer. (b) Schematic of dual polarity Z-TOF mass spectrometer illustrating ion extraction region and ion trajectory.

383 3. Data Analysis Methods

384 ATOFMS generates large quantities of data; the instrumentation is capable of
385 collecting size and chemical information on greater than 500 individual particles per
386 minute, depending upon the atmospheric concentrations. While simple laboratory
387 experiments may run for only a few hours, ambient monitoring studies with ATOFMS
388 may operate for weeks. Therefore, continuous sampling during a single ambient study
389 can yield tens of millions of individual spectra – far too many to analyze by hand. For
390 efficient analysis of such a volume of data, an ideal data analysis technique must perform
391 automatic sorting and classification of individual particles. There are a number of
392 available mathematical algorithms that have been adapted to cluster mass spectral data,

393 such as fuzzy *c*-means clustering, *k*-means clustering, hierarchical clustering, and
394 artificial neural networks (6-10). The two main data analysis methods used in this
395 dissertation are described in the next sections. Any adjustments to these methods or
396 alternative approaches will be discussed in subsequent chapters. The adaptive resonance
397 theory-based neural network algorithm, ART-2a, has been used to analyze ATOFMS data
398 for several years. In a benchmark test against other clustering methods, ART-2a has been
399 shown to yield comparable results (9). A modification of ART-2a analysis involves
400 matching to predefined seeds, such as a source signature library described below.

401 Though more detailed descriptions of the ART-2a algorithm have been provided
402 elsewhere (11-13), a brief description is included here. Using the mass spectral ion
403 patterns and peak intensities, ART-2a separates particles into distinct classes (clusters) of
404 chemically similar particles within large ATOFMS data sets and generates new clusters
405 whenever a data point (mass spectrum) falls outside the proximity to all existing classes.
406 Thereby, ART-2a provides the advantage of determining the contributions from
407 previously detected particle classes while also introducing information on new particle
408 types. For each particle, ART-2a combines all of the ion peak patterns and intensities in
409 the positive and negative spectra to form an *n*-dimensional weight vector (normally 350
410 *m/z* units for each polarity, making 700 units total), in which the ion intensity at each *m/z*
411 ratio is normalized with respect to the maximum peak intensity present in the vector. In
412 the classification process, particles are selected randomly and their spectral information is
413 compared to each particle cluster (weight vector) by calculating the dot product of the
414 particle vector and cluster weight vector. The dot product value ranges from 0 to 1,
415 where 1 represents identical vectors. If the dot product value between the particle vector
416 and any of the existing weight vectors is above the user-defined threshold (vigilance
417 factor - VF), that particle is added to the cluster with the highest dot product value. If a
418 learning rate is defined, that cluster will slightly weight its vector toward the newly added
419 particle. If the dot product value is below the VF, the particle defines a new cluster.
420 Once all of the particles have been assigned, ART-2a then compares each particle against
421 the entire set of created clusters to ensure proper placement. This final step is repeated
422 for a number of set iterations (usually 20).

423 Upon completion of the ART-2a analysis, there may be hundreds to thousands of
424 resulting clusters based on the complexity of the data and the VF used. For example, a
425 low VF (≤ 0.5) will yield a low number of clusters with limited homogeneity, whereas a
426 high VF (≥ 0.7) will yield a large number of clusters with high homogeneity. The user
427 then visually inspects the ART-2a clusters to manually classify and label them based on
428 their spectral characteristics. Some clusters may be combined by hand if they have
429 similar spectral characteristics or key class features, in order to reduce the total number of
430 clusters to a more manageable size.

431 One of the features of ART-2a is that it can compare the ambient particle vectors
432 to a set of predefined weight vectors, known as seeds. In direct analogy to the procedure
433 described in the previous section, the dot product of each particle vector is crossed with
434 each seed weight vector. The particle is placed into the seed cluster that produces the
435 highest dot product, assuming it is above the user-defined VF. The main difference
436 between this matching method and the normal ART-2a procedure is that if no dot product
437 value exceeds the VF, the particle is placed into an “unmatched” category, rather than

438 initiating a new particle class. In addition, this method has no learning rate parameter, so
439 the vectors of the seeds remain constant as particles are matched to them.

440 The matching function is ideal for apportioning individual ambient particles to
441 specific sources using a source signature library. The recently developed source
442 signature library is described in detail elsewhere (14), but a brief description is given
443 here. The size-segregated library combines the carefully identified mass spectral source
444 signatures from a series of source (such as vehicle dynamometer studies) and ambient
445 characterization studies to serve as the predefined cluster seeds. Designed to expand as
446 the ATOFMS signatures for particles from new sources are obtained, the library presently
447 contains source fingerprints for heavy duty diesel vehicle (HDDV) and light duty
448 gasoline vehicle (LDV) exhaust emissions, dust, sea salt, biomass, and meat cooking. It
449 also has non-source specific signatures acquired in ambient studies, including aged
450 elemental carbon (EC), aged organic carbon (OC), amine-containing particles,
451 ammonium-rich particles, vanadium-rich particles, EC, and polycyclic aromatic
452 hydrocarbon (PAH)-containing particles. The major advantages of using this data
453 analysis technique are the elimination of user bias in labeling and the speed in which it
454 can apportion particles.

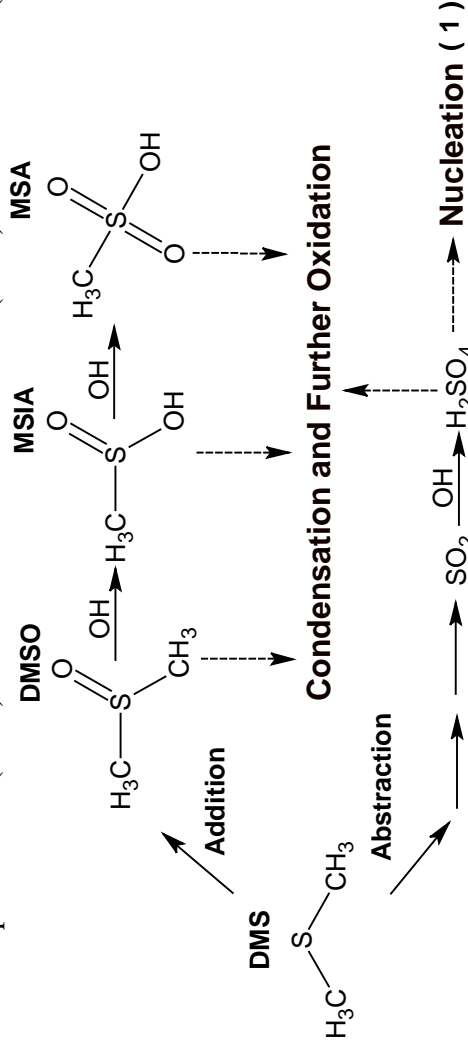
455

457 1. Real-time detection and mixing state of methanesulfonate in single particles

458 at an inland urban location during a phytoplankton bloom

459 i. Introduction

460 Aerosols contribute significantly to climate change by directly scattering and
 461 absorbing incoming solar radiation and acting as cloud condensation nuclei (CCN) (15).
 462 Sulfate is an aerosol species of particular climatic importance from a scattering
 463 perspective in addition to enhancing the cloud forming potential of aerosols (16). In
 464 Riverside, CA, sulfate comprises up to 13-20% of the mass of particles ranging in size
 465 from 0.1-2.5 μm (17). Sulfate derives from sulfur dioxide (SO_2) oxidation forming
 466 sulfuric acid (H_2SO_4), which condenses onto particles; sources of sulfate include both
 467 anthropogenic (18) and biogenic sources with the most important biogenic sulfate source
 468 being the oxidation of dimethyl sulfide (DMS) (19). DMS is produced from the
 469 enzymatic cleavage of dimethylsulphoniopropionate (DMSP), a compound produced by
 470 oceanic phytoplankton (19-20). A simplified reaction scheme of DMS oxidation adopted
 471 from Hopkins et al. (2008) and von Glasow and Crutzen (2004) is shown below (21-22).



Condensation and Further Oxidation

472 **Sulfur Dioxide Sulfuric Acid**
 473 Sulfate formation from DMS primarily derives from the OH-abstraction path (18,21)
 474 leading to sulfate formation on pre-existing particles or the homogeneous nucleation of
 475 particles, which act as a new source of CCN potentially increasing cloud droplet number
 476 (21,23). Organosulfur compounds such as dimethyl sulfoxide (DMSO), methanesulfonic
 477 acid (MSIA), and methanesulfonic acid (MSA), as well as other products, are also
 478 produced from DMS oxidation via the OH-addition pathway. DMSO primarily
 479 condenses onto pre-existing particles and droplets where oxidation to form the
 480 intermediate MSIA and the more stable product, MSA, takes place; aqueous phase
 481 processing enhances the kinetics of these oxidation processes (18,21,24). MSA can also
 482 be oxidized in the condensed phase leading to the formation of additional sulfate;
 483 however, this is slower and less efficient than the abstraction pathway (18,24). Since
 484 condensation and aqueous phase processing is favored over nucleation, organosulfur
 485 compounds are not known to act as a new source of CCN (18,21,23). Because of the
 486 opposing influence that different sulfur compounds can have on cloud droplet number, it

487 is important to distinguish between these species to understand their formation and
488 evolution in atmospheric aerosols.

489 Previous measurements of DMS oxidation products, primarily sulfate and MSA,
490 typically used off-line bulk analysis techniques. These measurements revealed that
491 particle mass concentrations of both sulfate and MSA peak during the summer, and the
492 ratio of the two species depend on factors such as temperature, presence of clouds,
493 presence of NO_x, and contribution of anthropogenic sulfate (21,25-27). Because sulfate
494 has anthropogenic and biogenic sources, MSA is also measured alone as an indicator of
495 biogenic sulfur. Using on-line instrumentation, Phinney et al. (2006) and Zorn et al.
496 (2008) quantified MSA at sea using an aerosol mass spectrometer (AMS) showing
497 diurnal trends in particulate MSA concentrations and correlations with oceanic biological
498 activity demonstrating the importance of real-time measurements (28-29). Single particle
499 observations of the mixing state of MSA-containing particles have primarily shown MSA
500 to be in the form of sodium and ammonium salts (21,30). While each of these studies has
501 contributed significantly to our understanding of the conditions when MSA formation
502 occurs, the impacts of intense oceanic blooms on MSA and sulfate concentrations at
503 inland locations remains unexplored. A number of important questions exist with regards
504 to MSA in inland urban locations: (i) how much of a contribution does biogenic sulfur
505 make to urban aerosols during periods of high biological oceanic activity?, (ii) what
506 degree of interaction occurs between ocean-derived biogenic emissions and
507 anthropogenic aerosols?, and (iii) how is MSA distributed within individual particles?
508 The goal of this study is to shed further light on these questions by performing real-time,
509 single-particle measurements of MSA-containing aerosols at an inland, urban
510 environment.

511 During the summer of 2005 as part of the Study of Organic Aerosols in Riverside,
512 CA (SOAR-1), real-time mass spectrometry measurements detected individual ambient
513 aerosols with MSA. Furthermore, co-located AMS measurements corroborated the
514 presence of organosulfur species (MSA) during SOAR-1 (31). The summer Riverside
515 aerosol showed the largest impacts from the ocean when daily westerly winds transported
516 coastal emissions across the Los Angeles (LA) Basin to Riverside (32). In the summer of
517 2005, intense blooms of *L. polyedrum* prevailed off the coast of southern California (33).
518 Because dinoflagellate species of phytoplankton such as *L. polyedrum* are known to
519 produce high concentrations of DMSP and DMSO (34), SOAR-1 was influenced by
520 anomalously high concentrations of ocean-derived biogenic sulfur. Single-particle, size-
521 resolved chemistry and diurnal trends of MSA are used herein to elucidate the influence
522 of elevated ocean-derived biological activity on aerosol chemistry at an inland urban
523 location.

524

525 **ii. Experimental**

526 During SOAR-1, ambient measurements were made on the University of
527 California, Riverside campus, approximately 60 miles inland from the Pacific Ocean
528 from July 30-August 15, 2005 ([http://cires.colorado.edu/jimenez-
529 group/Field/Riverside05/](http://cires.colorado.edu/jimenez-group/Field/Riverside05/)). Meteorological parameters including wind direction, wind
530 speed, and relative humidity (RH) were measured at the site. Chlorophyll data, which
531 serves as a proxy for oceanic biological activity, was obtained from the Southern
532 California Coastal Ocean Observing System (SCCOOS) (www.sccoos.org) from the

533 Newport Beach station at approximately 33.6°N, 117.9°W. Data was also obtained from
534 the Scripps Institution of Oceanography (SIO) Pier at 32.87°N, 117.3°W to supplement
535 data from the Newport Beach station by illustrating the high levels of biological activity
536 off the California coast from a historical perspective since this station has measured
537 chlorophyll for roughly 20 years. Data from the Newport Beach station is used for direct
538 comparison of chlorophyll concentrations with the detection of MSA based on the air
539 mass back trajectories, which indicate that the air masses traveled closer to this station
540 than the SIO Pier station before reaching Riverside, thus providing a more accurate proxy
541 of biological activity. Surface chlorophyll concentrations were measured twice a week at
542 the SIO Pier, and concentrations at ~3 m depth were measured every 4 minutes using
543 automated sensors at both the SIO Pier and the Newport Beach station. All data are
544 presented in Pacific Standard Time (PST), one hour behind local time.

545 The size-resolved chemical composition of individual aerosols was obtained in
546 real-time using an aerosol time-of-flight mass spectrometer (ATOFMS) with a size range
547 of 0.2-3.0 μm . The ATOFMS has been described in detail elsewhere (35). Briefly,
548 particles are sampled through a converging nozzle where they enter a differentially
549 pumped vacuum region causing the particles to be accelerated to their terminal velocity.
550 The particles next enter a light scattering region consisting of two continuous-wave lasers
551 (532 nm) located at a fixed distance from one another. The time required to traverse
552 these two lasers is correlated to the terminal velocity of the particle; the velocity is
553 converted to an aerodynamic diameter by calibrating with polystyrene latex spheres of a
554 known size. A 266 nm Nd:YAG laser desorbs and ionizes species from individual
555 particles producing both positive and negative ions that are analyzed in a dual-polarity
556 time-of-flight mass spectrometer.

557 A software toolkit, YAADA, was used to import ion peak lists into MATLAB
558 (The MathWorks) allowing for the analysis of ATOFMS data (36). Searches for MSA-
559 containing particles, characterized by an intense peak at m/z -95 (CH_3SO_3^-) (37-38), were
560 performed by selecting a peak area of 300 or above for m/z -95. Fresh sea salt particles
561 produce NaCl_2^- cluster ions at m/z -93, -95, and -97 (39), which could interfere with the
562 assignment of m/z -95 to MSA. However, almost all of the detected sea salt particles
563 (>99%) were aged as indicated by the strong presence of nitrate and sulfate that
564 heterogeneously displaced chloride (40) allowing for the unambiguous assignment of m/z
565 -95 to MSA. The measured particle mass spectra were then analyzed using a clustering
566 algorithm (ART-2a), which groups particles together based on mass spectral similarities
567 (41). ART-2a was run separately for submicron (0.2-1.0 μm) and supermicron (1.0-3.0
568 μm) particles. Using ART-2a with a vigilance factor of 0.8, over 90% of MSA-
569 containing particles and over 80% of non-MSA-containing particles were classified into
570 50 distinct clusters, providing a representative view of the aerosol composition during the
571 study. Naming schemes for the particle types presented in this paper are based on
572 previous work (32,42-43) and discussed in detail in the Supporting Information. Peak
573 identifications within this paper correspond to the most probable ions for a given m/z
574 ratio. The particle types observed were aged organic carbon (Aged OC), aged sea salt,
575 amines, Ca-containing, dust, elemental carbon (EC), elemental carbon mixed with
576 organic carbon (ECOC), ECOC and EC mixed with inorganic species (Inorganic ECOC
577 and Inorganic EC, respectively), biomass burning (K-combustion), NH_4 -containing,

578 vanadium from combustion sources (OC-V-sulfate), and polycyclic aromatic
579 hydrocarbons (PAH).

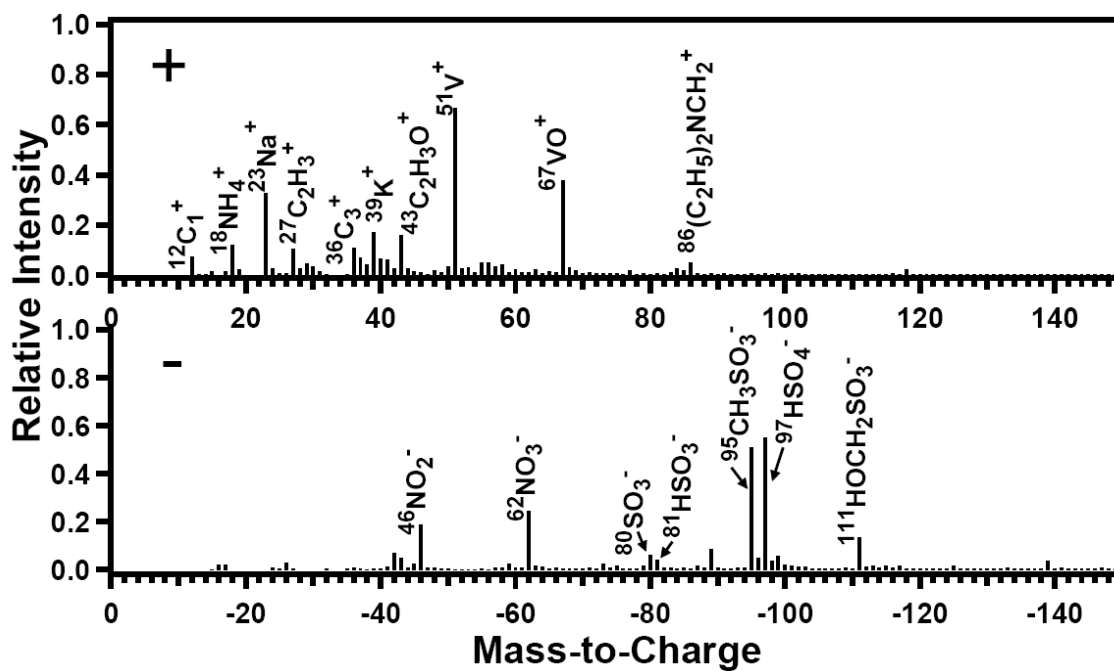
580 **iii. Results and Discussion**

581 **a. Temporal Trends of MSA-containing Particles and Biological Activity**

582 ATOFMS measurements during SOAR-1 indicate that up to ~67% of the
583 submicron (0.2-1.0 μm) and up to ~33% of supermicron (1.0-3.0 μm) particles by number
584 contained MSA. The average negative ion mass spectrum for a representative MSA-
585 containing particle type, shown in Figure S1, clearly shows a distinct ion marker at m/z -
586 95 indicative of MSA.

587 **1. Representative Mass Spectra of MSA-containing Particles and Naming Schemes of** 588 **Particle Types**

589 MSA-containing particles are characterized by an intense peak at m/z -95
590 (CH_3SO_3^-) (37-38). The average spectra of an OC-V-sulfate particle type mixed with
591 MSA is shown in Figure 3. MSA was found on nearly every particle type typical for the
592 Riverside area including local and transported particle types. Most of the particle types
593 observed in Riverside have undergone significant aging and have acquired secondary
594 species such as ammonium (m/z +18 (NH_4^+)), nitrate (m/z -62 (NO_3^-)), and sulfate (m/z -
595 97 (HSO_4^-)) (32,42). Aged organic carbon (aged OC) particles are characterized by
596 intense peaks at m/z +27 (C_2H_3^+), +29 (C_2H_5^+), +37 (C_3H^+), and +43 ($\text{C}_2\text{H}_3\text{O}^+$) (38,42).
597 Elemental carbon (EC) is characterized by carbon cluster ions such as m/z +12 (C_1^+), +24
598 (C_2^+), +36 (C_3^+),... C_n^+ (44). Elemental carbon organic carbon (ECOC) particles show
599 markers for both EC and OC (44). Aged sea salt particles are characterized by m/z +23
600 (Na^+), +62 (Na_2O^+), +63 (Na_2OH^+), (+81, +83 (Na_2Cl^+)), and +165 (Na_3SO_4^+) in addition
601 to markers of acquired secondary species such as nitrate (m/z -62 (NO_3^-)) and sulfate (m/z -
602 -97 (HSO_4^-)) in place of chloride (m/z -35, -37 (Cl^-)) (39). The amine particle type is
603 characterized by intense peaks at m/z +86 ($(\text{C}_2\text{H}_5)_2\text{NCH}_2^+$) and +118 ($(\text{C}_2\text{H}_5)_3\text{NOH}^+$)
604 (42,45). Dust particles are characterized by inorganic species such as $^{23}\text{Na}^+$, $^{24}\text{Mg}^+$,
605 $^{27}\text{Al}^+$, $^{39}\text{K}^+$, $^{40}\text{Ca}^+$, $^{56}\text{Fe}^+$, and silicates (46). Inorganic EC and inorganic ECOC particles
606 are EC or ECOC, respectively, associated with an intense inorganic (e.g. $^{39}\text{K}^+$ or $^{40}\text{Ca}^+$)
607 ion peak. Ca-containing particles contain an intense peak at m/z +40 (Ca^+), but are most
608 likely associated with combustion processes rather than dust due to their smaller size and
609 their association with carbonaceous ion markers (42,47). K-combustion particles are
610 characterized by an intense peak at m/z +39 (K^+) and lower intensity OC peaks (48).
611 NH_4 -containing particles contain an intense peak at m/z +18 (NH_4^+) and lower intensity
612 OC peaks (32,42). OC-V-sulfate particles are characterized by intense ion markers at m/z
613 +51 (V^+) and +67 (VO^+), lower intensity OC peaks, and sulfate (m/z -97 (HSO_4^-)) (42,49-
614 50). PAH particles contain intense peaks at m/z +39 (C_3H_3^+) and +43 ($\text{C}_2\text{H}_3\text{O}^+$) and
615 repetitive OC peaks of lower intensity (51).

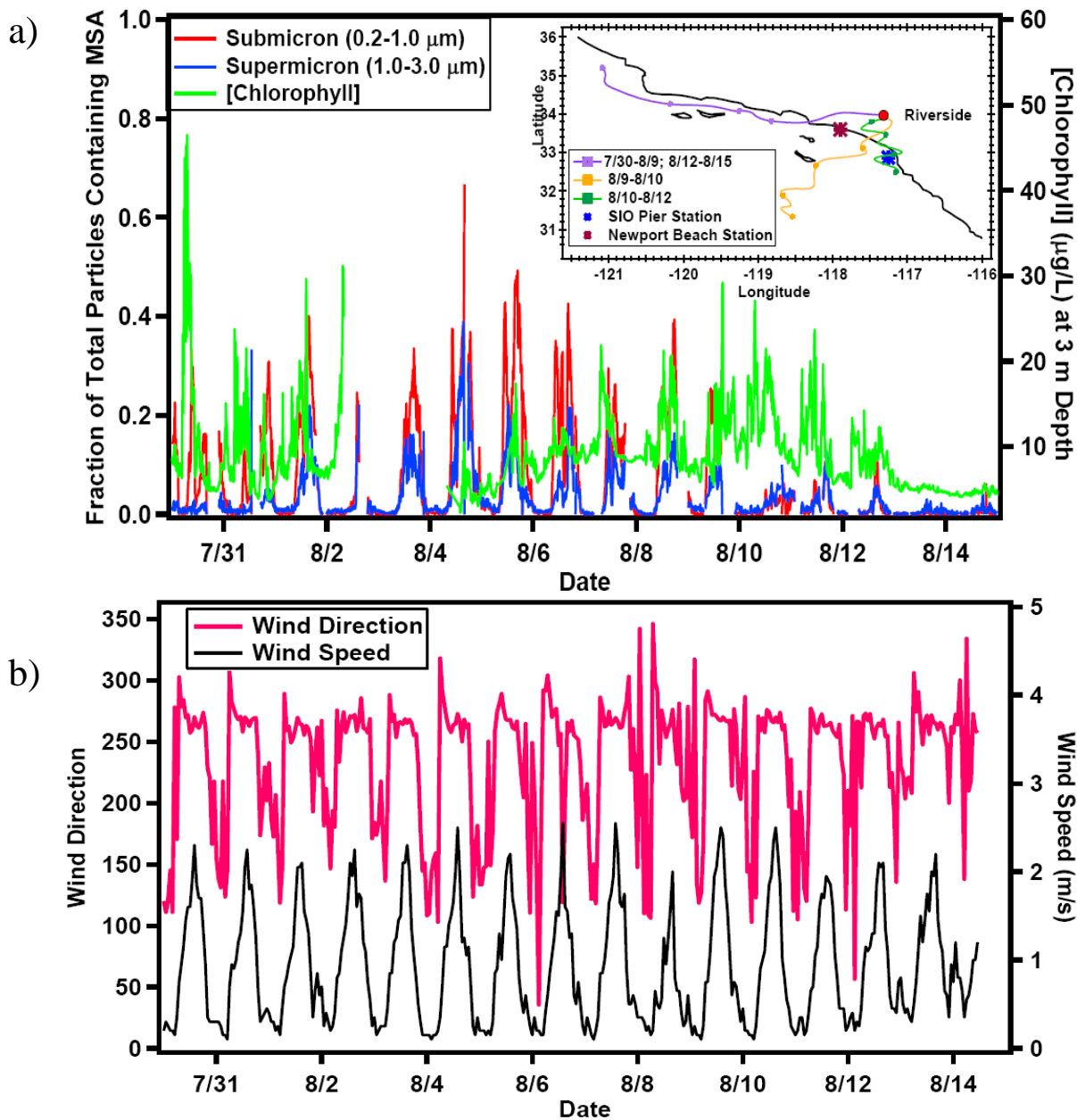


616

617

618

Figure 3: Average positive and negative ion mass spectra for the OC-V-sulfate particle type containing MSA (m/z -95) during SOAR-1.

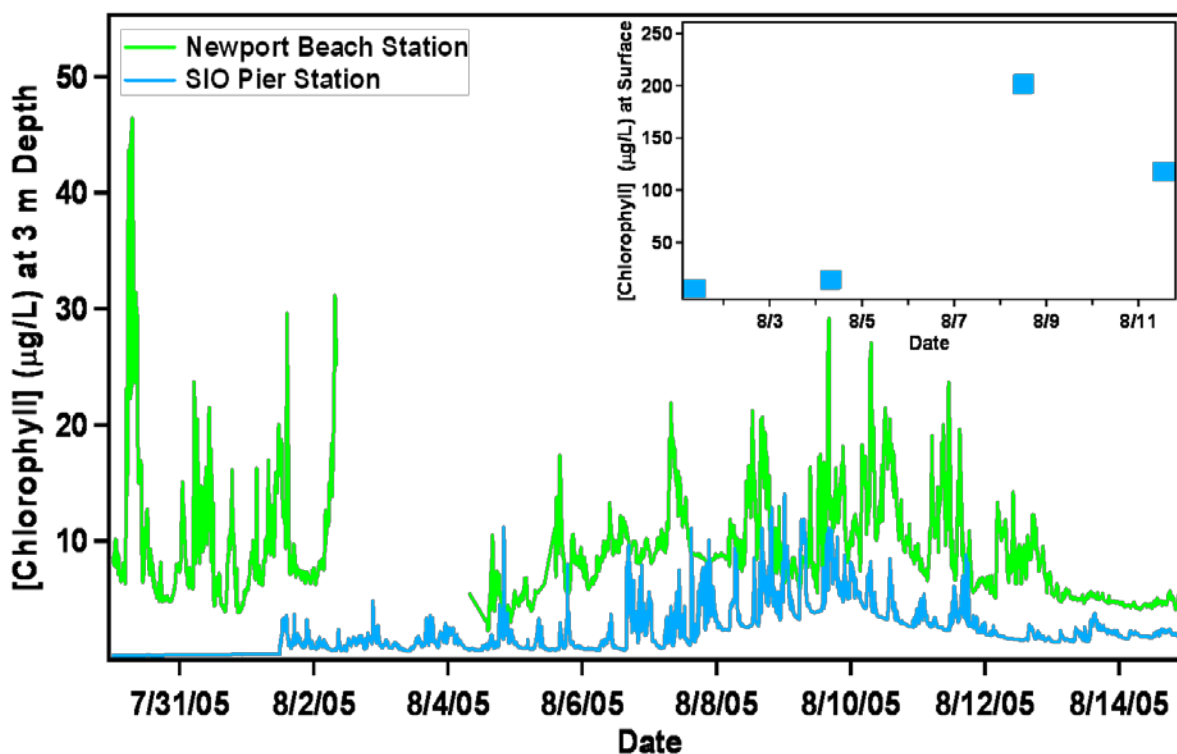


619

620 Figure 4: (a) Time series showing the fraction of MSA-containing submicron (red line) and
 621 supermicron (blue line) particles during SOAR-1 and chlorophyll concentrations (green line) taken
 622 from the Newport Beach station (33.6°N, 117.9°W) at 3 m depth. Gaps in chlorophyll data occur
 623 from August 2-4. Inset shows typical HYSPLIT 48 hour back-trajectories for air masses arriving to
 624 the sampling site during different time periods in addition to the locations of the automated
 625 chlorophyll stations. Each trajectory is taken at 500 m altitude, and each point on the trajectory
 626 corresponds to a 12-hour increment. (b) Time series showing the corresponding wind speed (black
 627 line) and direction (pink line).

628 In Figure 4a, the fractions of all submicron and supermicron particles containing
 629 MSA and chlorophyll concentrations taken from the Newport Beach station at 3 m depth
 630 from July 30-August 15, 2005 are shown. The inset in Figure 4a shows 48-hour
 631 HYSPLIT air mass back-trajectories (52) representative of those occurring over the

632 duration of the study in addition to the locations of the two automated stations collecting
 633 chlorophyll data. A comparison of the data collected at the two automated stations can be
 634 found in the Supporting Information (see Figure 5). Three main air mass trajectory
 635 patterns were observed with transport times estimated from HYSPLIT ranging from ~8
 636 hours to longer than a day (32,52): (i) “Coastal” occurred between July 30-August 9 and
 637 resumed August 12-15 with sampled air masses originating from the Pacific Ocean
 638 northwest of LA traversing near the Newport Beach station before arriving to Riverside,
 639 (ii) “Open Ocean” occurred August 9-10 and originated further from the coast toward the
 640 open ocean, and (iii) “Inland/Stagnant” occurred August 10-12 with limited oceanic
 641 transport resulting in an observed decrease in the fraction of MSA-containing particles on
 642 August 10 as shown in Figure 4a. Additionally, Figure 4b shows the corresponding wind
 643 speed and direction during this time period. Comparison of the time series in Figure 4a
 644 and 1b shows a strong diurnal trend with fractions of MSA-containing particles
 645 increasing ~6-8 hours following the onset of westerly winds and increased wind speed
 646 during coastal transport conditions, as verified by HYSPLIT air mass back trajectories
 647 (e.g. 7/30-8/9 as shown in Figure 4a). Day-to-day variations can be explained, in part, by
 648 changes in meteorological conditions.



649
 650 **Figure 5: Chlorophyll data at 3 m depth from the Newport Beach (33.6°N, 117.9°W) and SIO Pier**
 651 **(32.87°N, 117.3°W) automated stations. Inset is chlorophyll data measured at the surface of the**
 652 **SIO Pier.**

653 **2. Chlorophyll Data from the SIO Pier and the Newport Beach Stations**

654 The SIO Pier and Newport Beach automated stations record chlorophyll data at
 655 approximately 3 m depth every 4 minutes. Additionally, surface chlorophyll
 656 concentrations are measured twice per week at the SIO Pier. As seen in Figure 5, the

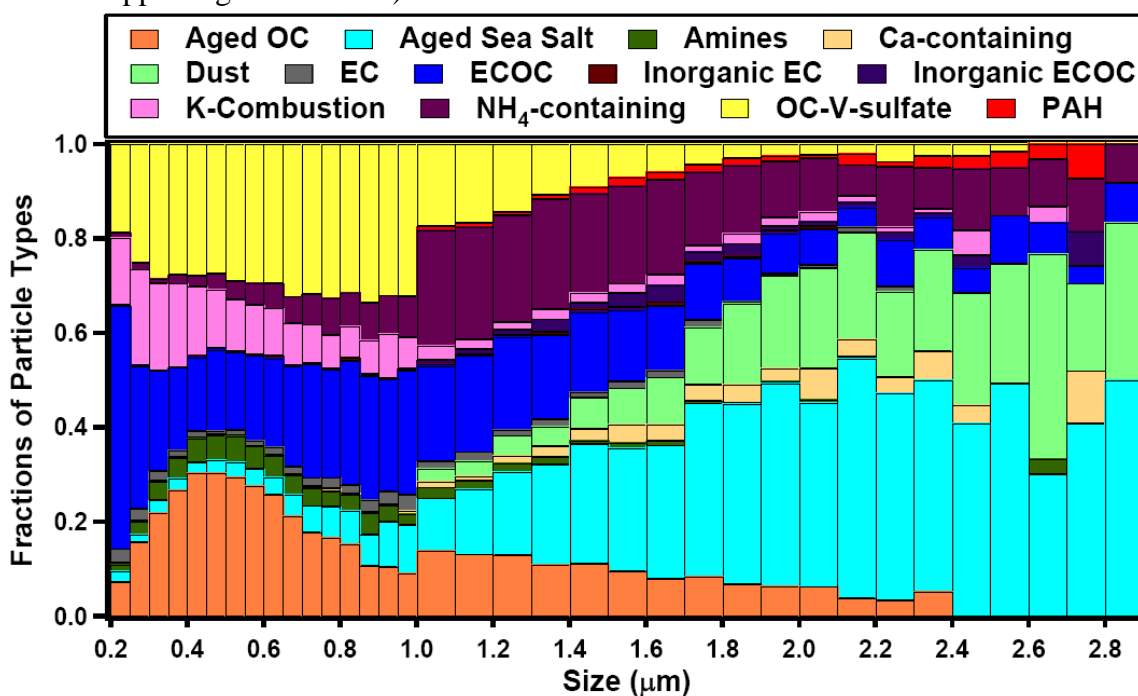
657 chlorophyll concentrations taken at 3 m depth for both stations are comparable showing
658 similarities in diurnal trends and similar magnitudes of chlorophyll concentrations. Inset
659 in this figure is the surface chlorophyll data taken at the SIO Pier. The chlorophyll
660 measurements show elevated concentrations and a diurnal pattern consistent with the
661 presence of a phytoplankton bloom. Although the SIO Pier station has two depths of
662 chlorophyll data and a longer continuous data set, the data from the Newport Beach
663 station was primarily used in this paper due to the fact that the air masses traveled closer
664 to this station than the SIO Pier station before reaching the sampling site as seen in Figure
665 4. Chlorophyll data from the SIO Pier station provided a historical context to base our
666 assertion that high levels of biological oceanic activity occurred during SOAR-1.

667 In addition to meteorology, oceanic biological activity also influenced the
668 observed fractions of MSA-containing particles. On August 12, the air masses follow the
669 “Coastal” trajectories; however, in contrast to July 30-August 9, the fractions of MSA
670 remained low (Figure 4a). This is attributed to an observed decrease in oceanic
671 chlorophyll concentrations to ≤ 5 $\mu\text{g/L}$ (Figure 4a), which followed the end of the major
672 phytoplankton bloom on August 11 (17). Prior to this, diurnal spikes in both the fraction
673 of MSA-containing particles and chlorophyll concentrations were observed with daily
674 chlorophyll concentrations typically reaching up to $\sim 25\text{-}30$ $\mu\text{g/L}$. Similar spikes in
675 chlorophyll were observed from the same depth at the SIO Pier in La Jolla, CA. At the
676 same time, surface chlorophyll concentrations measured twice per week at the SIO Pier
677 reached as high as ~ 200 $\mu\text{g/L}$. Analysis of 18 years of surface chlorophyll measured at
678 the SIO Pier yields an average of 2.5 $\mu\text{g/L}$ with a maximum of 218.95 $\mu\text{g/L}$ (53)
679 indicating that anomalously high levels of biological activity were occurring off the coast
680 of California during SOAR-1 resulting in the detection of large number fractions of
681 MSA-containing particles, as shown herein. Furthermore, we speculate that some of the
682 MSA detected in Riverside could oxidize completely impacting sulfate levels at locations
683 further inland; however, no measurements were made at these locations. The
684 contribution of biogenic sulfur during summer has been established for several coastal
685 locations (25-27); however, these are the first real-time, single-particle measurements of
686 MSA at an inland location during a period of intense biological activity establishing how
687 oceanic biological activity could impact both MSA and, potentially, sulfate levels at an
688 inland urban location in California under the proper meteorological conditions. This is
689 significant due to the interest in sorting out the major sources of sulfate in California and
690 determining the relative proportions from anthropogenic sources (i.e. ships, heavy duty
691 diesel vehicles) versus biogenic sources (i.e. oceanic biological activity).

692 **b. Single-Particle Mixing State of MSA-containing Particles**

693 Riverside is impacted by local sources including vehicle exhaust and nearby
694 Chino dairy farms, which contribute to ammonium, nitrate, carbonaceous, and amine
695 concentrations, in addition to transported particle types from the LA coast, which provide
696 a source of ocean-derived aerosol species and additional sources of combustion aerosols
697 (42-43,54). To gain further insight into the sources and processes contributing to the
698 presence of MSA, we examined the mixing state of MSA-containing particles. The size-
699 resolved, single-particle mixing state of MSA-containing particles is illustrated in Figure
700 6 for submicron and supermicron particles. While Figure 6 classifies MSA-containing
701 particles into general particle types based on the most prevalent ion peaks, it is important

702 to note that ~76% and ~45% of MSA-containing submicron particles, by number, were
 703 internally mixed with ammonium and sodium, respectively, and ~83% and ~71% of
 704 MSA-containing supermicron particles, by number, were internally mixed with
 705 ammonium and sodium, respectively. The prevalence of these two species with MSA is
 706 expected based on previous measurements of the mixing state of MSA-containing
 707 particles (21,30). Additionally, ~87% of MSA-containing submicron and ~82% of MSA-
 708 containing supermicron particles contained sulfate (m/z -97 (HSO_4^-)), which is expected
 709 since DMS and, to a lesser extent, MSA oxidation also produces sulfate (18,24). In sum,
 710 ~25% of all submicron and ~22% of all supermicron particles, by number, contained
 711 sulfate. However, since ATOFMS measurements cannot distinguish biogenic and
 712 anthropogenic sulfate contributions to m/z -97, the relative contribution of biogenic
 713 sulfate cannot be inferred herein. MSA was mixed primarily with transported and aged
 714 particle types, and a higher percentage of submicron particles contained MSA (up to
 715 67%) in comparison to the supermicron particles (up to 33%) likely due to the enhanced
 716 particle surface area in this size range (see Figure S3, which is discussed in further detail
 717 in the Supporting Information).



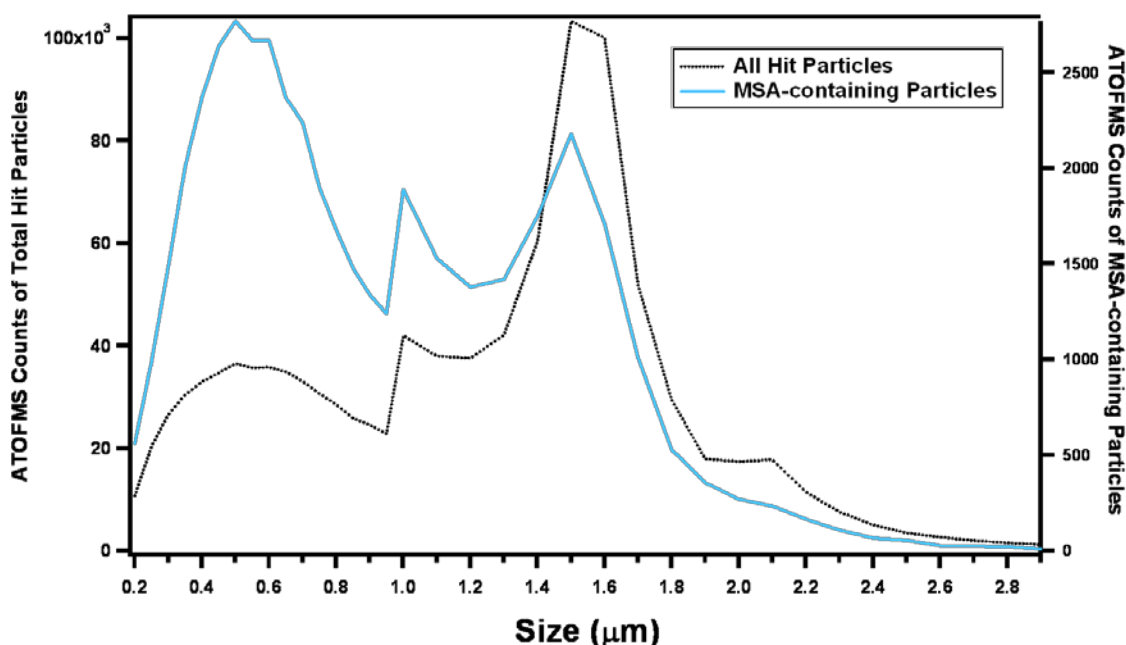
718

719 **Figure 6: MSA-containing particle types plotted as a function of size. Submicron (0.2-1.0 μm)**
 720 **particles are plotted in 0.05 μm bins while supermicron (1.0-3.0 μm) particles are plotted in 0.1 μm**
 721 **bins.**

722 **1. Enhancement of MSA-containing Particles in the Submicron Mode**

723 ATOFMS provides data of both single-particle chemical composition as well as
 724 particle size in real-time. Because of this, the size distribution of MSA-containing
 725 particles for SOAR-1 can be compared to all sampled particles. MSA and its
 726 organosulfur precursors are condensable species that contribute to particle growth rather
 727 than nucleation (18,23). MSA has typically been measured as sodium or ammonium salts
 728 associated with smaller aerosol particles ($d > 2 \mu\text{m}$) (30). Because our measurements have
 729 shown a wide variation in the mixing-state of particles containing MSA, the size

730 distribution of MSA-containing particles was examined and compared to the size
 731 distribution of the total hit particles during SOAR-1 (Figure 7). The particle detection
 732 efficiency of the ATOFMS depends on particle size. This is namely due to the
 733 transmission efficiency of the nozzle inlet, which creates a sharp peak at 1.7 μm (55-56).
 734 Ambient number concentrations of aerosols; however, display an opposing trend with
 735 higher number concentrations at smaller particle sizes (57). These two opposing factors
 736 result in a bimodal size distribution as seen in Figure 7, which is a representative size
 737 distribution of hit particles obtained from the ATOFMS. Comparison of the size
 738 distribution of the total hit particles and the size distribution of MSA-containing particles
 739 shows that a higher fraction of the submicron (0.2-1.0 μm) particles contained MSA (up
 740 to 67%) than the supermicron particles (up to 33%) showing a relative enrichment of
 741 MSA on submicron particles.



742

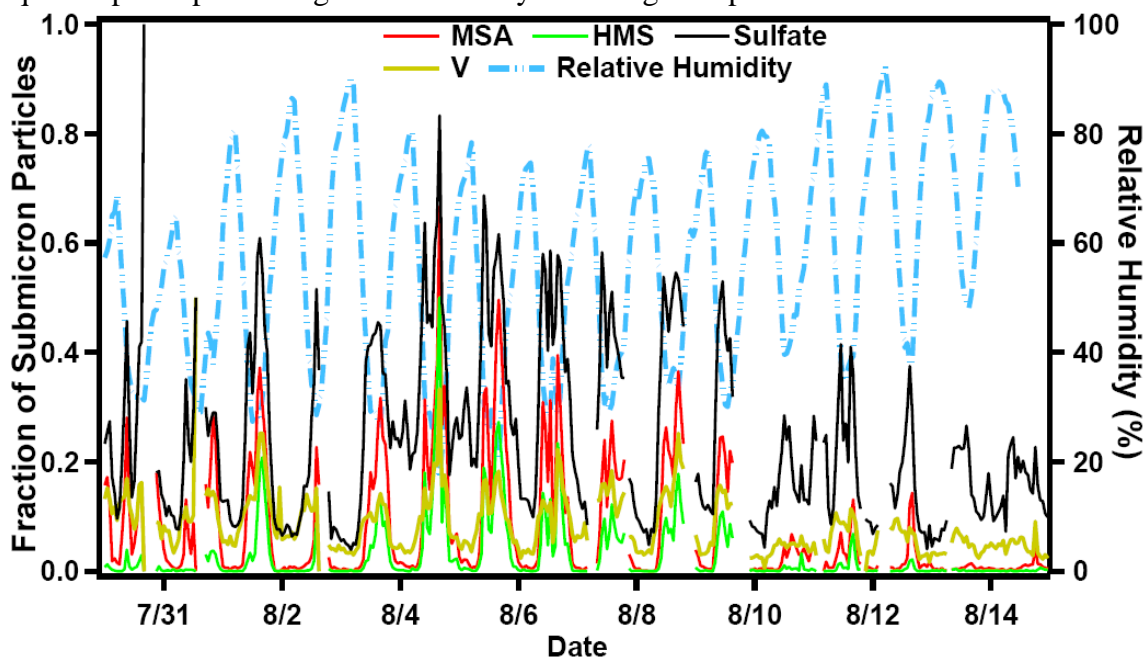
743 **Figure 7: Size distributions of all hit particles (black line) during SOAR-1 and only MSA-containing**
 744 **particles (blue line).**

745 Comparison of MSA-containing particles with all observed particle types for
 746 SOAR-1 revealed that some particle types contained little to no MSA while large
 747 fractions of other particle types contained MSA. No MSA was detected on submicron
 748 dust, and only ~3% of the total observed supermicron dust contained MSA, which is
 749 expected since dust is locally produced unlike MSA (54). Interestingly, only small
 750 fractions of the measured carbonaceous particle types (e.g. Aged OC, EC, and ECOC)
 751 were found to contain MSA. It is possible that the accumulation of secondary species
 752 particularly OC, which was the most commonly observed carbonaceous particle type, on
 753 pre-existing particles during transport from the LA coast to Riverside could potentially
 754 mask the detection of MSA (43,54). Certain particle types, however, were found to be
 755 enriched in MSA: approximately 37% and ~20% of the total observed OC-V-sulfate
 756 submicron and supermicron particles, respectively, and ~33% of aged sea salt submicron
 757 particles contained MSA. The OC-V-sulfate particle type is associated with residual fuel
 758 combustion primarily from ships (49-50,58). OC-V-sulfate particles and aged sea salt are

759 both coastally emitted along with DMS, which suggests that DMS oxidation products
760 primarily partitioned onto coastal particle types that then underwent aging as they were
761 transported inland. Therefore, MSA is a useful marker for segregating transported versus
762 locally generated particles.

763 c. Correlation of MSA with Other Species

764 During SOAR-1, MSA-containing particles were typically associated with fog
765 processing markers (see Figure 3) at m/z -81 (HSO_3^-) and -111 ($\text{HOCH}_2\text{SO}_3^-$), which are
766 the ion markers for the organosulfur compound hydroxymethanesulfonate (HMS)
767 (37,51,59). Figure 8 illustrates the temporal trends observed for submicron MSA, V,
768 sulfate, and HMS-containing particles and RH. The correlation between V and MSA-
769 containing particles ($R^2=0.57$) can be attributed to the fact that they were both coastally
770 emitted as well as the potential catalytic role of vanadium in enhancing MSA on particles
771 described in the next section. Submicron particles containing MSA and sulfate were also
772 correlated ($R^2=0.68$) potentially implying a common source for both species. The
773 correlation between MSA and HMS was very strong ($R^2=0.84$), which suggests the
774 important role of aqueous phase chemistry in MSA formation (24) as well as the
775 hygroscopic nature of MSA (18). Previous studies have shown HMS tracking RH during
776 stagnant fog events (59); however, HMS was not correlated with RH during this study
777 suggesting that the formation of HMS was not due to local increases in RH. HMS was
778 instead correlated with MSA suggesting that MSA-containing particles had undergone
779 aqueous phase processing either coastally or during transport to Riverside.



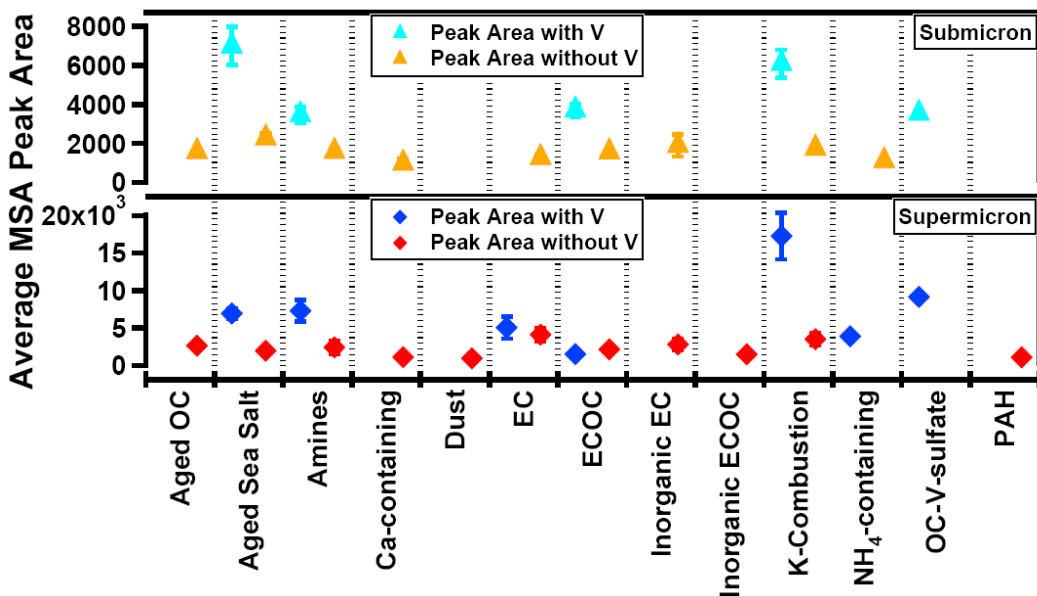
780

781 **Figure 8: Temporal profile of ATOFMS counts of submicron MSA- (red line), HMS- (green line),**
782 **sulfate- (black line) and V- (brown line) containing particles. Relative humidity (RH) is also shown**
783 **(dashed blue line).**

784 d. Role of Vanadium in MSA Formation

785 Vanadium is one of the most common metals observed in Riverside, particularly during
786 coastal transport conditions (17,43). Vanadium is used to catalyze the oxidation of sulfur
787 species such as S(IV) (60) and DMS (61) under industrial conditions. To better

788 understand the observed correlation between vanadium and MSA-containing particles
789 described above, the relationship between MSA and vanadium was further investigated.
790 MSA-containing particles internally mixed with vanadium were separated from those not
791 mixed with vanadium (see Figure 10 in the Supporting Information), and the amount of
792 MSA on each particle type was compared by averaging ion peak areas. The peak area of
793 a particular m/z can be related to the relative amount of a specific chemical species on
794 each particle type (62-63); Figure 9 shows a comparison for the major particle types
795 detected during the study. During the laser desorption/ionization process, variations in
796 ion intensity can occur depending on the chemical matrix of the particle (62). It is
797 important to note that the particles shown in Figure 9 have been separated into different
798 matrices, based on general particle type, and the MSA ion intensities are only compared
799 for the same chemical matrix. Furthermore, vanadium represents a small mass fraction of
800 the total particle mass (50) so its presence or absence has a negligible effect on the
801 overall chemical matrix. As shown in Figure 9, the peak area of MSA found on particles
802 types that contained vanadium was, in general, ~3 times larger when compared to similar
803 matrix particles not containing vanadium adding strong support that vanadium is acting
804 as a catalyst for the formation of MSA. Another factor that must be considered is that the
805 increased amount of MSA on particles internally mixed with vanadium could be solely
806 due to the fact that both species were emitted along the coast leading to increased time for
807 MSA formation to occur on these particles during transport to Riverside. However, if
808 this were the case, then it would be expected that other coastally emitted particle types
809 such as aged sea salt would also have higher amounts of MSA present regardless of
810 whether it was internally mixed with vanadium or not. As shown in Figure 9, only the
811 particles types, including aged sea salt, internally mixed with vanadium had higher
812 amounts of MSA. This shows that transport time is not the only factor leading to
813 enriched MSA in particles. Residual fuel also contains high levels of iron (64), which is
814 known to catalyze sulfur oxidation in the aqueous phase (65). Because the ionization
815 potential for vanadium is much lower (6.75 eV for V vs. 7.90 eV for Fe) (66) and hence
816 the ATOFMS sensitivity for vanadium is higher than for iron, the possibility that iron is
817 actually present and playing a role in catalyzing MSA formation rather than vanadium
818 cannot be ruled out. However, these results show that different particle types emitted by
819 specific anthropogenic sources, in this case residual fuel burning from ships, enhance
820 MSA and, potentially, sulfate production in atmospheric particles.

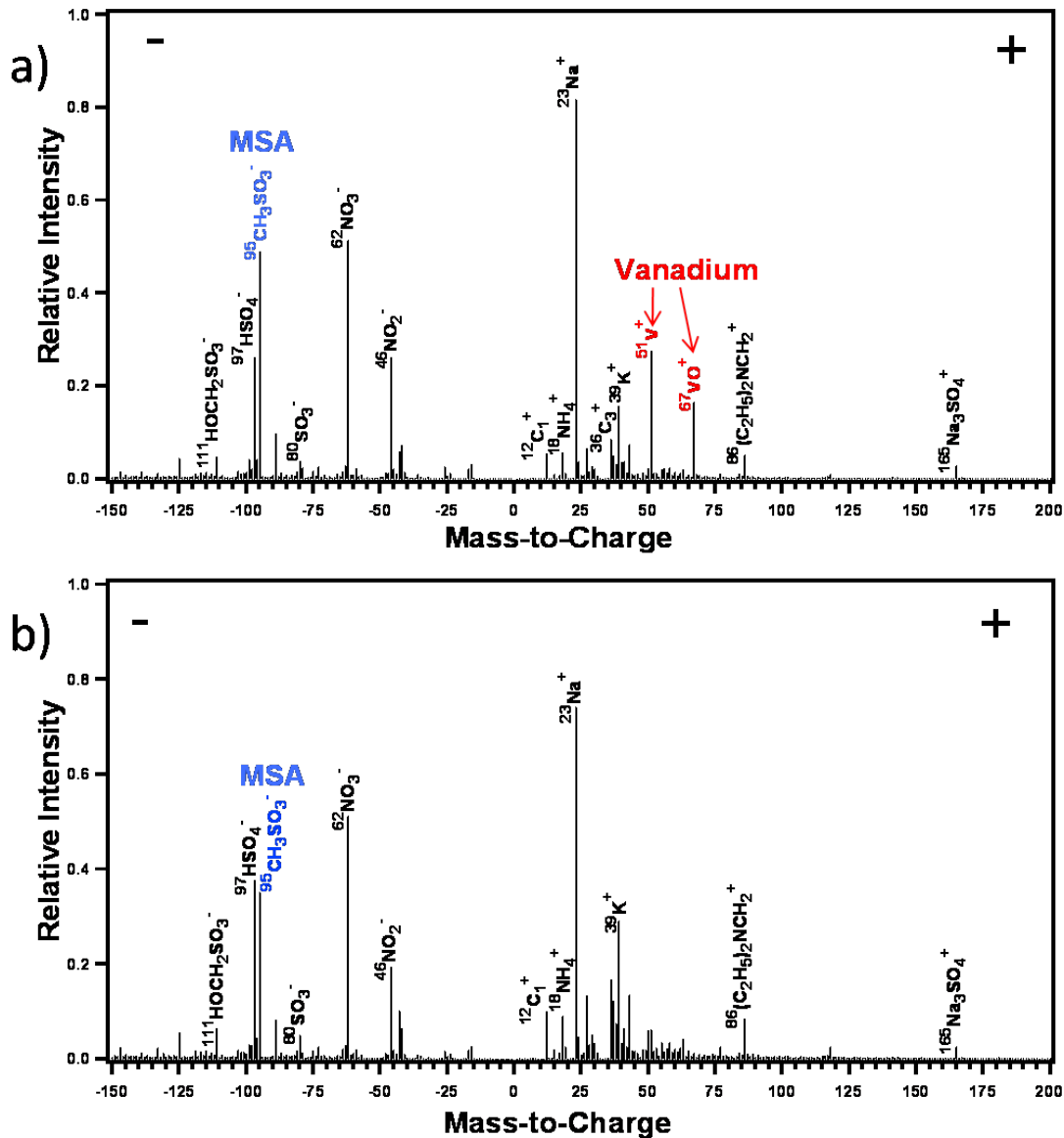


821

822 **Figure 9: Average peak area of MSA (m/z -95) for MSA-containing submicron particle types mixed**
 823 **with V (light blue triangles) and submicron particles containing no V (orange triangles) are shown in**
 824 **the top panel. The average peak area of MSA on supermicron particles containing V (dark blue**
 825 **diamonds) and containing no V (red diamonds) are shown in the bottom panel. The vertical bars**
 826 **correspond to 95% confidence intervals associated with the peak areas.**

827 **1. Comparison of MSA-containing Particles Mixed with V and without V**

828 MSA-containing particles were grouped by particle type and subdivided into
 829 particles with and without V by segregating particles containing m/z +51 (V^+) and +67
 830 (VO^+). ATOFMS utilizes laser desorption/ionization corresponding to an energy input of
 831 4.7eV/photon (at 266nm) (66) producing $\sim 9.4eV$ for a two photon ionization. This
 832 energy input makes this technique very sensitive to trace metals since the ionization
 833 potential of metals is low (63,66-67). Because of this sensitivity, a true distinction
 834 between particles mixed with V and those without V can be made. Figure 10 shows
 835 representative spectra from one particular particle type (aged sea salt) mixed with
 836 vanadium (Figure 10a) and without vanadium (Figure 10b). From Figure 10a and 10b,
 837 one can see a qualitative increase in the ion peak intensity of MSA (m/z -95). This was
 838 further investigated in Figure 9 for each particle type revealing a consistent increase in
 839 the ion peak intensity of MSA for particles mixed with V. One factor that must be
 840 considered is that during the laser desorption/ionization process, variations in ion
 841 intensity can occur depending on the chemical matrix of the particle (63). However,
 842 comparing the ion peak intensity of MSA for the same particle type with and without V
 843 reduces complications associated with matrix effects.



844

845 Figure 10: Representative average aged sea salt positive and negative ion mass spectra of particles (a)
 846 mixed with and (b) without V.

847 e. Atmospheric Implications

848 These measurements reveal how high biological oceanic activity can impact
 849 aerosol chemistry in an inland, urban environment. Periods when high levels of oceanic
 850 biological activity were observed correlated with high levels of MSA at an inland
 851 location, particularly on particles containing vanadium. Past measurements have
 852 primarily examined the influence of MSA on aerosols in clean marine environments. Our
 853 measurements, however, show that MSA can also condense onto anthropogenic particle
 854 types as well as sea salt. Future studies at multiple sampling locations spaced along a
 855 trajectory from the LA coast to inland locations should be conducted to further
 856 investigate how the mixing-state of MSA-containing particles evolves in urban locations.
 857 Previous ATOFMS studies have demonstrated the evolution of particle mixing-state

858 within the LA Basin; however, time periods influenced by high levels of oceanic
859 biological activity were not investigated (54).

860 This study shows how anthropogenic aerosols can influence the atmospheric
861 processing of biogenically emitted sulfur species. Enhanced production of MSA has
862 been observed for reactions between $\text{MSIA}_{(\text{aq})}$ and Fe(III) (68); however, little is known
863 about the ability of anthropogenic emissions to influence the processing of ambient
864 biogenic sulfur emissions. This study demonstrates the catalytic abilities of vanadium to
865 enhance MSA formation; vanadium has also been shown to enhance the conversion of
866 anthropogenically produced SO_2 to sulfate in a recent single-particle study (49).
867 Typically, biogenic and anthropogenic sources are considered separately when describing
868 aerosol and air pollution chemistry; however, this study highlights the importance of
869 including anthropogenic aerosols from sources such as ships when estimating the
870 production of MSA and sulfate in coastal and urban environments. Finally, both MSA
871 and sulfate strongly influence particle hygroscopicity meaning that the enhanced
872 production of either of these species by anthropogenic particle types could have
873 significant implications for cloud droplet formation in both marine and inland
874 environments.

875 **iv. Acknowledgements**

876 The authors would like to acknowledge Paul Ziemann (UC Riverside), Ken
877 Docherty (CU, Boulder), the UC Riverside Air Pollution Research Center, and the entire
878 Prather group, particularly Laura Shields, for assistance during the SOAR-1 field
879 campaign. The authors also thank Meagan McKay and the Goldstein group (UC
880 Berkeley) for providing wind direction, wind speed, and relative humidity data. This
881 work was supported by the California Air Resources Board. K. Pratt has been funded in
882 part by an NSF Graduate Research Fellowship (2006-2009) and an EPA STAR Graduate
883 Fellowship (2005-2006). The EPA has not officially endorsed this publication, and the
884 views expressed herein may not reflect the views of the EPA. The authors gratefully
885 acknowledge the NOAA Air Resources Laboratory (ARL) for the provision of the
886 HYSPLIT transport and dispersion model and/or READY website
887 (<http://www.arl.noaa.gov/ready.html>) used in this publication. The authors also gratefully
888 acknowledge the Southern California Coastal Ocean Observing System (SCCOOS)
889 (www.sccoos.org/) for the provision of chlorophyll data used in this publication.

890

891

892 **2. Real-time, single-particle volatility, size, and chemical composition measurements**
893 **of aged urban aerosols**

894 **i. Introduction**

895 Atmospheric aerosol particles impact global climate, regional air pollution, and
896 human health (15). Originating from a variety of sources, such as biomass burning, fossil
897 fuel combustion, and dust suspension, primary aerosol particles undergo physical and
898 chemical transformations (atmospheric aging) during transport (15). Heterogeneous
899 reactions of particles with trace gases and gas-particle partitioning of semivolatile
900 species, such as ammonium nitrate and oxidized organics, contribute to changes in
901 particle size, structure, and chemical composition (15). Thus, atmospheric aging
902 provides challenges in the identification of the major particle sources connected with
903 human health risks, making source-specific regulations difficult (69).

904 To examine the sources and chemical aging pathways of different particle types, a
905 thermodenuder (TD) can be used to heat ambient particles, inducing the vaporization of
906 semivolatile species and leaving behind the non-volatile particle cores (70-71). Size-
907 resolved volatility data, provided by measuring the size distributions of particles before
908 and after heating, is often used to infer the mixing state of the particle core, which is most
909 commonly assumed to be primarily black carbon (71). Volatilization and humidification
910 tandem differential mobility analyzer (VH-TDMA) provided an increased understanding
911 of ambient particle mixing state through hygroscopic behavior measurement (72).
912 However, it is challenging using conventional techniques to interpret the size-resolved
913 volatility data for particles containing multiple chemical components and externally
914 mixed aerosol ensembles that are typically observed in the atmosphere (70). Further, few
915 studies have measured the chemistry of heated atmospheric particles to directly determine
916 their mixing state. Frey et al. (73) found that black carbon (BC) mass concentrations
917 tracked mass concentrations of less-volatile particles during periods of local traffic
918 influence; increased disagreement between BC mass and less-volatile mass was found
919 during periods of long-range transport. An aerosol mass spectrometer, measuring the
920 chemical composition of non-refractory particulate species, was used to examine bulk
921 ambient particle residuals in real-time in Tokyo, Japan (74) and Mexico City (75).
922 However, it is important to measure the complete chemistry including refractory species,
923 such as black carbon, mineral dust, and sea salt, as these species could contribute
924 significantly to the low volatility particle core.

925 Herein, an automated TD was coupled to an aerosol time-of-flight mass
926 spectrometer (ATOFMS) to provide the first real-time, individual-particle size and
927 volatility-resolved chemistry measurements. Using laser desorption-ionization, both the
928 refractory and non-refractory particulate species are measured, providing the first on-line
929 measurements of the chemistry of heated individual particle residuals. Aerosol particles
930 undergo significant atmospheric processing within the Los Angeles (LA) basin, and thus,
931 the vast majority of unheated particles show evidence of organic carbon, ammonium,
932 amines, and nitrate accumulated during transport (76-77). A comparison of the chemistry
933 of the unheated aged particles with the heated particle cores is presented, to help provide
934 an improved understanding of particle volatility and ambient aerosol sources.

935 **ii. Experimental**

936 ATOFMS measurements of single ambient aerosol particles were conducted
937 during the Study of Organic Aerosols field campaign in Riverside, California from
938 November 2-13, 2005 (SOAR-2) ([http://cires.colorado.edu/jimenez-](http://cires.colorado.edu/jimenez-group/Field/Riverside05/)
939 [group/Field/Riverside05/](http://cires.colorado.edu/jimenez-group/Field/Riverside05/)). Ambient temperature and atmospheric water content were
940 measured using a shielded Vaisala HMP 45AC temperature and RH probe. The ground-
941 based prototype of the aircraft (A)-ATOFMS, described in Chapter 2, measured the
942 vacuum aerodynamic diameter (d_{va}) and dual-polarity mass spectra of individual particles
943 from ~100-1000 nm in real-time. For simplicity, A-ATOFMS will be referred to
944 throughout this chapter as ATOFMS. During SOAR-2, particles were desorbed and
945 ionized using 266 nm radiation from a Q-switched Nd:YAG laser operating at ~0.4-0.8
946 mJ. Polystyrene latex spheres of known physical diameter from 95-1400 nm were used
947 to complete the single-particle size calibration.

948 To examine the volatilities of the ambient particles, an automated valve-
949 controlled TD system (75) was utilized in series with the ATOFMS. A nafion dryer was
950 used to dry the particles before the TD. With continuous aerosol flow through the TD
951 (heated) and bypass line (unheated), the particles sampled by the ATOFMS switched
952 between heated and unheated ambient aerosol every 10 minutes. The heated portion of
953 the TD stepped through 8 temperatures: 171°C, 230°C, 201°C, 171°C, 142°C, 113°C,
954 83°C, 54°C. Since each portion of the schedule was maintained for 10 minutes, one full
955 cycle took 160 minutes before repeating. An activated carbon diffusion denuder
956 prevented volatilized species from condensing back onto the particles. With a flow rate
957 of 0.6 lpm, the residence time of the aerosol in the heating portion of the TD was
958 approximately 9 seconds. For further details and characterization of the TD, refer to
959 Huffman et al. (75).

960 Every 10 minutes, the ATOFMS switched between sampling either unheated and
961 heated (54-230°C) ambient particles. In this work, particle residues remaining at 230°C
962 are referred to as cores, although a specific morphology is not defined herein. A total of
963 1,390,199 size-resolved dual-polarity mass spectra were collected with the ATOFMS
964 from Nov. 2-13, 2005. Data collection times were adjusted for delays in transport lines
965 between the TD and ATOFMS. Data collected up to 20 seconds after the TD valve
966 switch were eliminated to reduce error caused by possible aerosol mixing. Overall, dual-
967 polarity mass spectra from 717,705 unheated and 462,982 heated particles were utilized
968 in this analysis. Single-particle mass spectra were imported into YAADA
969 (www.yaada.org), a software toolkit for Matlab (The MathWorks, Inc.). An adaptive
970 resonance theory-based clustering method (ART-2a) (78) was used to classify single-
971 particle mass spectra with a vigilance factor of 0.80, learning rate of 0.05, and 20
972 iterations. ART-2a classifies particles into separate clusters based on the presence and
973 intensity of ion peaks in individual single-particle mass spectra. Peak identifications
974 correspond to the most probable ions for a given m/z ratio based on previous lab and field
975 studies; the peak area of a specific m/z is related the amount of a specific species on each
976 particle (62). General particle classes are defined by characteristic chemical species or
977 possible source; these labels do not reflect all of the species present within a particular
978 particle class.

979 For comparison of SOAR particles to particulate source emissions, particle
980 signatures from heavy duty diesel vehicles (HDDV) and gasoline-powered light duty

981 vehicles (LDV) were acquired during dynamometer source studies (79). Fresh ship
982 emissions were acquired during sampling at the Port of Los Angeles (80). The fresh
983 wildfire plume particle mass spectral signature was acquired during a flight over a
984 prescribed burn in Wyoming. The mass spectral signature of unreacted sea salt was
985 acquired during sampling along the California coast, and the unreacted dust signature was
986 acquired in the lab from suspended soil (81).

987 Size-resolved number concentrations of ATOFMS particle classes were calculated using
988 a method described previously by Reinard et al. (82). A scanning mobility particle sizer
989 (SMPS, model 3081, TSI, Inc.) in series with the TD provided size-resolved number
990 concentrations of unheated and heated particles during SOAR-2. Particle mobility
991 diameters (d_m) measured by the SMPS must be converted to d_{va} using the following
992 equation, discussed in detail by DeCarlo et al. (83):

$$993 \quad d_{va} = \frac{\rho_{eff}}{\rho_o} d_m \quad (1)$$

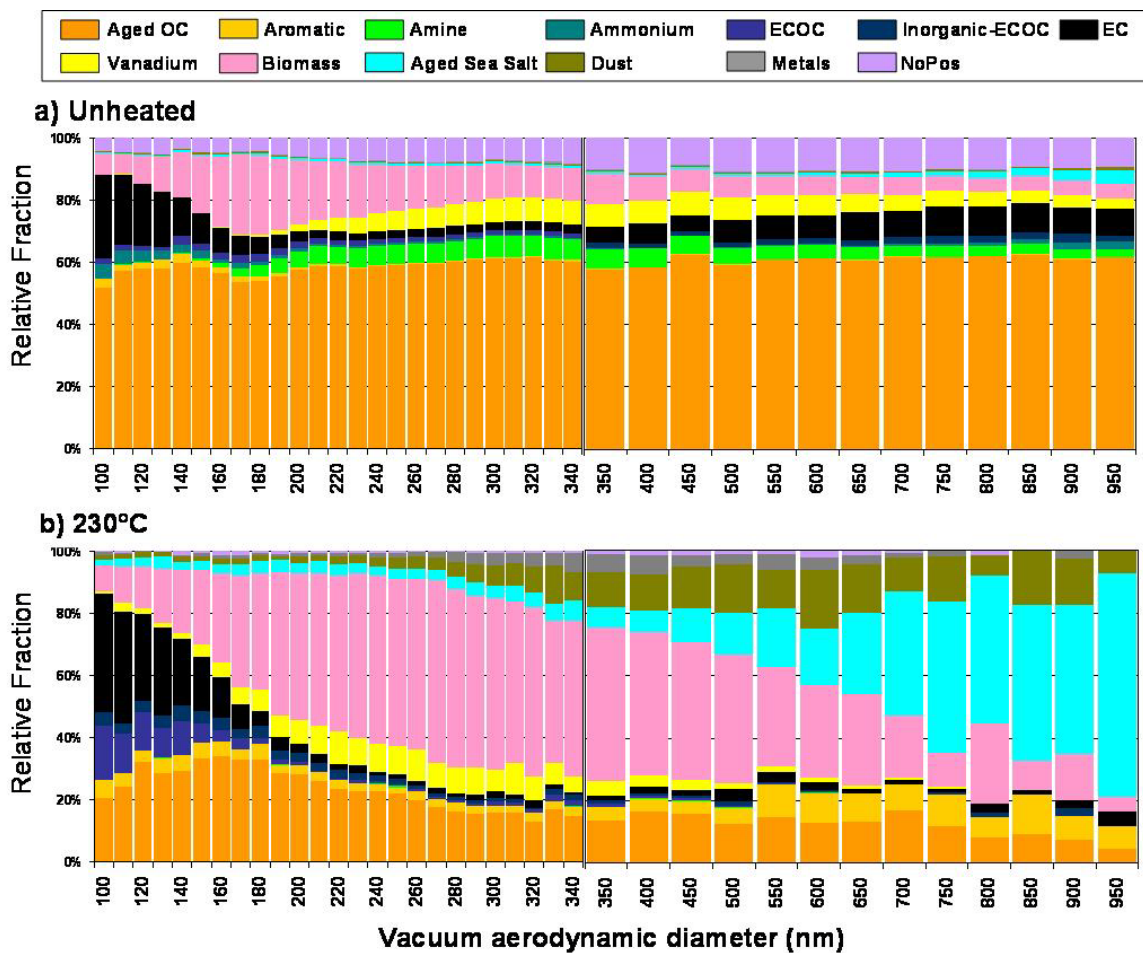
994 where ρ_{eff} is the effective density and ρ_o is the standard density (1.0 g/cm³). Average
995 size-resolved number concentrations were calculated for 103-995 nm (d_{va}) particles,
996 using an ρ_{eff} of 1.4 g/cm³, which was representative of most submicron SOAR-2 particles,
997 which were spherical due to the condensation of water, organics, and ammonium nitrate
998 (84). Using average fractions of ATOFMS particle classes for different size bins, size-
999 resolved number concentrations were calculated for unheated and heated particle classes.

1000 **iii. Results and Discussion**

1001 ***a. Ambient Aerosol Chemistry***

1002 From Nov. 2-13, westerly winds were observed from ~9:00-16:00 each day with
1003 diurnal trends in RH and ozone; most trajectories showed transport times of up to 12
1004 hours from LA, Irvine, or San Diego to Riverside (76). An average PM_{2.5} (particulate
1005 matter < 2.5 μm) mass concentration of 42 μg/m³ was observed with build-up and
1006 stagnation periods leading to an observed maximum of 106 μg/m³ (76). Individual
1007 ambient submicron (100-1000 nm) unheated and heated particles were classified into
1008 thirteen general particle classes: aged organic carbon (OC), aromatic, amine, ammonium-
1009 rich, elemental carbon-organic carbon (ECOC), inorganic-ECOC, elemental carbon (EC),
1010 vanadium, biomass, aged sea salt, dust, metals, and nitrate-sulfate particles with no
1011 positive ions (NoPos). The vast majority (~85%) of unheated particles showed evidence
1012 of organic carbon, ammonium, and nitrate accumulated during transport to Riverside (76-
1013 77); sulfate was also present in most (~70%) particles. The relative contributions of these
1014 particle classes with respect to size are shown in Figure 11. Mass spectral signatures and
1015 size-resolved number concentrations of the aged OC, EC, vanadium, and biomass
1016 burning particles classes at ambient and 230°C are shown in Figure 12.

1017 The particles in the aged OC class, which comprised ~60% by number of all
1018 unheated particles from d_{va} ~100-1000 nm, contained oxidized organic carbon species,



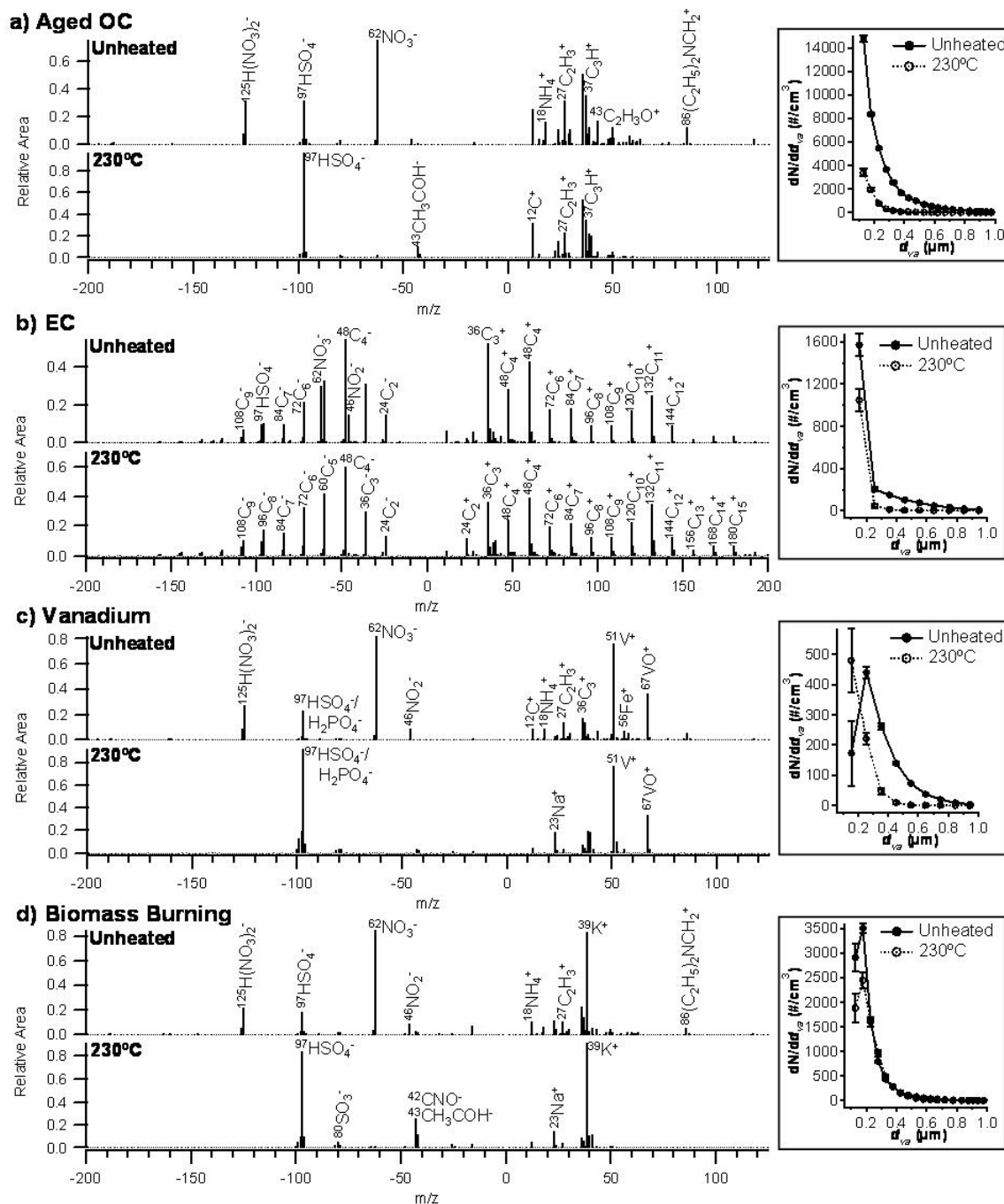
1019

1020 Figure 11: Size-resolved chemical composition of a) unheated and b) 230°C heated particles.

1021 Size resolution is 10 nm and 50 nm for the ranges of 100-350 nm and 350-1000 nm, respectively.

1022 Relative fractions of 230°C particle cores are illustrated for c) 100-150 nm, d) 200-250 nm, and

1023 e) 750-800 nm.



1024

1025

1026

1027

Figure 12: Average ATOFMS representative mass spectra and size-resolved number concentrations of unheated and 230°C heated particles for a) aged OC, b) EC, c) vanadium, and d) biomass burning particle classes.

1028

1029

1030

1031

1032

1033

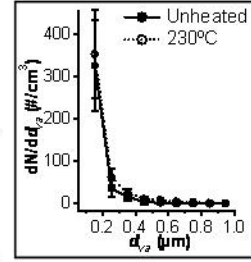
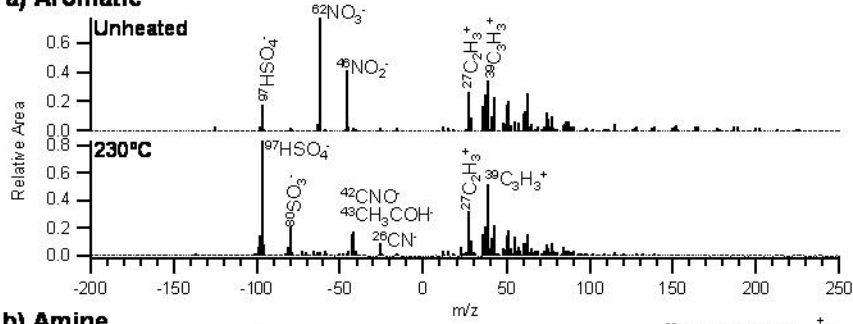
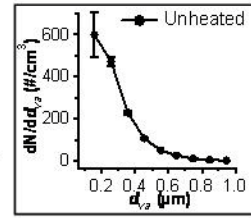
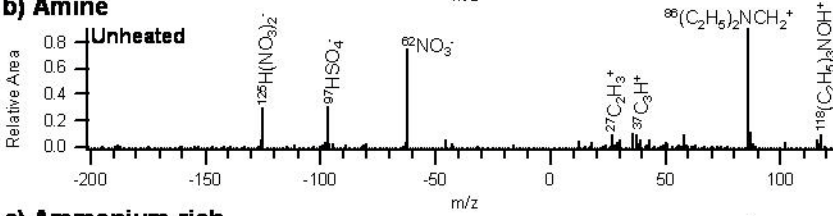
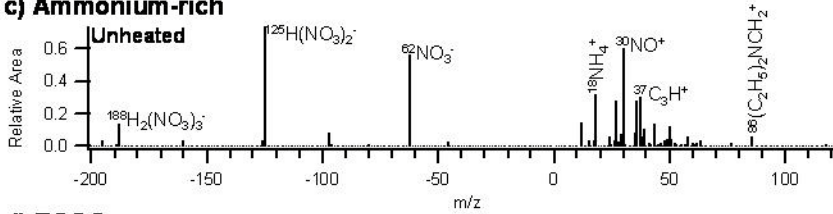
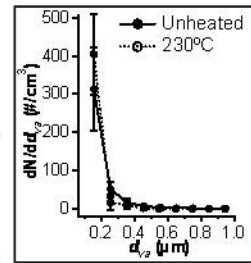
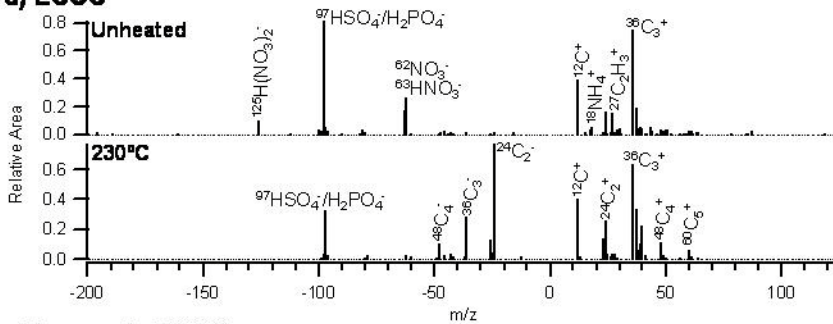
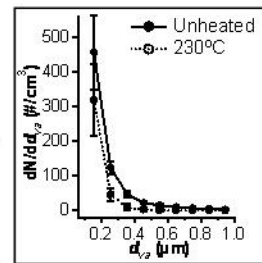
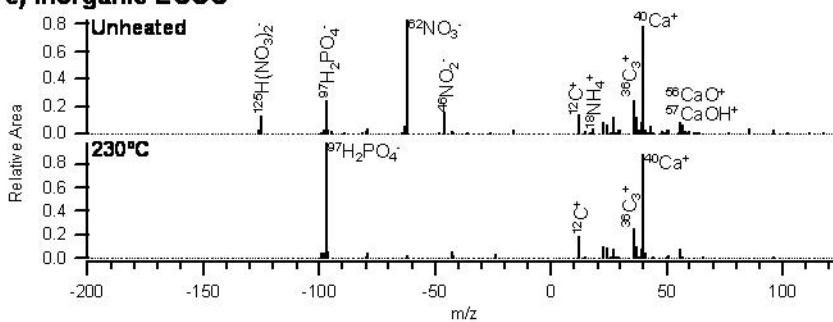
amines, ammonium, nitrate, and sulfate. The mass spectra were dominated by carbonaceous marker ions at m/z 12(C^+), 27($\text{C}_2\text{H}_3^+/\text{CHN}^+$), 36(C_3^+), 37(C_3H^+), 43($\text{CH}_3\text{CO}^+/\text{CHNO}^+$), and 86($(\text{C}_2\text{H}_5)_2\text{N}=\text{CH}_2^+$), an alkylamine fragment (38,45). Other notable ions include ammonium (m/z 18, NH_4^+), nitrate (m/z -62, NO_3^- , and -125, $\text{H}(\text{NO}_3)_2^-$), and sulfate (m/z -97, HSO_4^-) due to the aged nature of the Riverside particles (54). Previously, secondary organic carbon has been shown to comprise 50% of the total

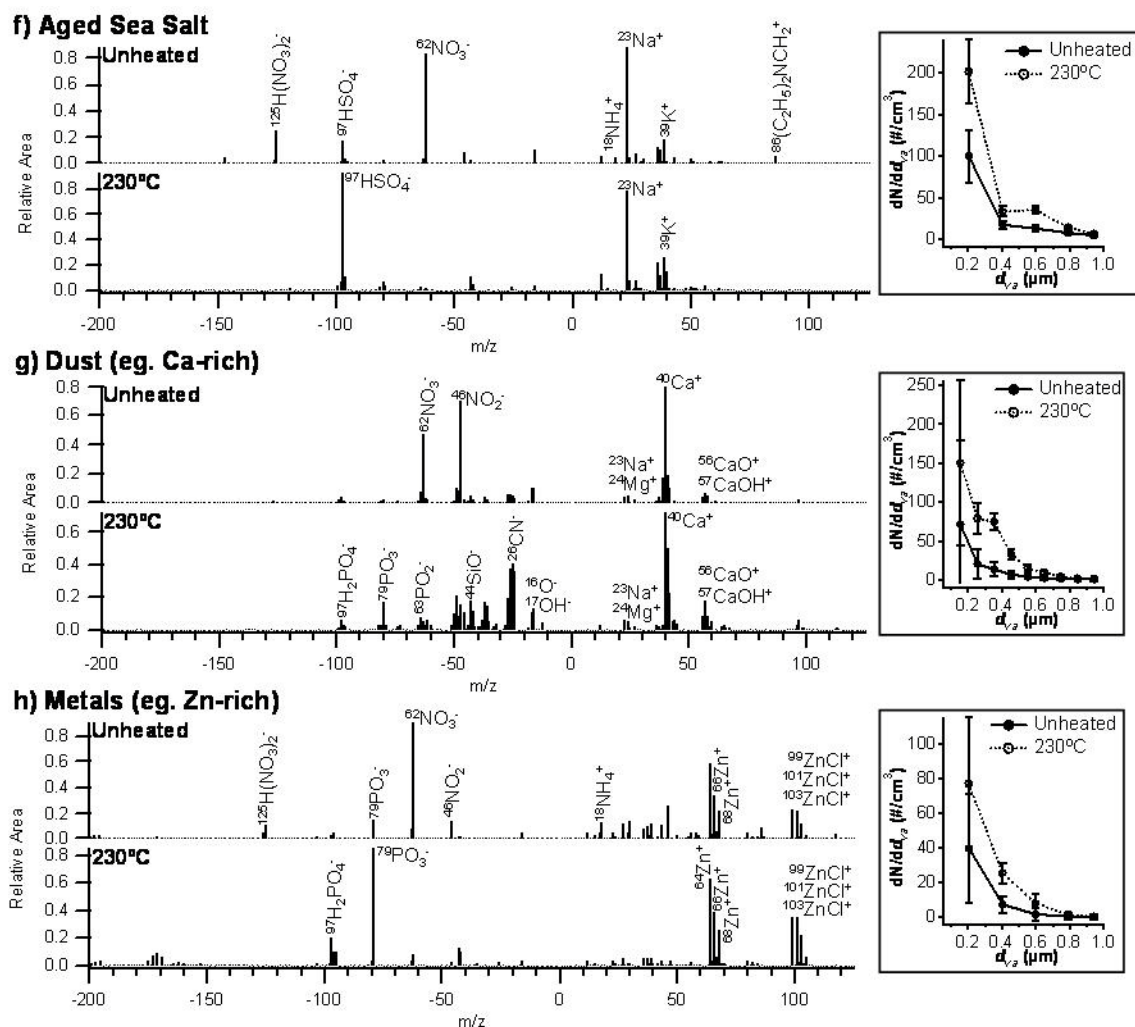
1034 PM_{2.5} (particulate matter < 2.5µm) organic carbon mass in Riverside County in
1035 November (85).

1036 Mass spectral signatures for the EC particles, attributed to vehicle emissions, were
1037 characterized by intense carbon cluster positive and negative ions from C^{+/-} to C_n^{+/-} with
1038 less intense nitrate and sulfate markers (86-87). EC particles comprised 17 ± 1% by
1039 number in the unheated 103-153 nm *d_{va}* size bin, with reduced contribution (3-10%) at
1040 greater diameters. With heating, nitrate was vaporized from the particles, concurrent
1041 with a decrease in particle size. Vanadium-containing particles, attributed to ship,
1042 automobile, and industrial emissions (76), were characterized by intense positive ions at
1043 *m/z* 51(V⁺) and 67(VO⁺) with less intense carbonaceous ion peaks (76). The negative
1044 ions are characterized by nitrate, sulfate, and phosphate. Ammonium, OC, and nitrate
1045 volatilized upon heating. The biomass burning particle class, which comprised ~10-24%
1046 by number of all unheated particles from *d_{va}* 100-400 nm, was characterized by an intense
1047 potassium ion with less intense carbonaceous positive ions; the negative ions are
1048 dominated by nitrate and sulfate (48,88). With heating, ammonium, amines, nitrate, and
1049 semi-volatile OC volatilized from the particles.

1050 Other particle types included: aromatic, amine, ammonium, ECOC, inorganic-
1051 ECOC, aged sea salt, dust, and metals. The mass spectral signatures and size-resolved
1052 number concentrations of these particle classes are shown in Figure 13. The aromatic
1053 particles were characterized by carbonaceous marker ions, aromatic fragment ions (*m/z*
1054 51(C₄H₃⁺), 63(C₅H₃⁺), 77(C₆H₅⁺), 115(C₉H₇⁺), 165(C₁₃H₉⁺), 189(C₁₅H₉⁺)), a
1055 monoaromatic molecular ion (*m/z* 139(4-nitrophenol)), and polycyclic aromatic
1056 hydrocarbon (PAH) molecular ions (*m/z* 128(naphthalene), 152(acenaphthylene),
1057 202(pyrene/fluoranthene), 276(benzo [*ghi*] perylene)) (38,86). Nitrate (*m/z* -46, NO₂⁻,
1058 and -62, NO₃⁻) and sulfate are present in the negative ion mass spectra. With heating,
1059 nitrate is removed from these particles. The presence of *m/z* -26(CN⁻), -42(CNO⁻),
1060 -43(CH₃COH⁻), and -80(SO₃⁻) become readily apparent in the 230°C spectra. The
1061 presence of *m/z* -26 and -46 is indicative of organonitrate and nitro-PAH compounds in
1062 diesel exhaust (89). The amine-rich particle class was dominated by *m/z*
1063 86((C₂H₅)₂N=CH₂⁺) with less intense amine marker ions at *m/z* 58(C₂H₅NHCH₂⁺),
1064 102((C₂H₅)₃NH⁺), and 118((C₂H₅)₃NOH⁺) (45).

1065 The ammonium-rich positive mass spectra are dominated by *m/z* 18(NH₄⁺) and
1066 30(NO⁺) with less intense OC and amine marker ions; the negative ions are characterized
1067 by intense nitrate markers: *m/z* -62(NO₃⁻), -125(H(NO₃)₂⁻), and -188((H₂(NO₃)₃)⁻) (90). It
1068 is important to note that these nitrate clusters correspond to periods with very high
1069 ambient nitrate mass concentrations. Ammonium nitrate is formed when NO_x, emitted
1070 from vehicles, is oxidized to nitric acid (HNO₃) and reacts with gas-phase ammonia
1071 (NH₃), primarily from livestock emissions (91). At

a) Aromatic**b) Amine****c) Ammonium-rich****d) ECOC****e) Inorganic-ECOC**



1073

1074 Figure 13: Average ATOFMS representative mass spectra and size-resolved number
 1075 concentrations of unheated and 230°C heated particles for the following particle types: a)
 1076 aromatic, b) amine, c) ammonium-rich, d) ECOC, e) inorganic-ECOC, f) aged sea salt, g)
 1077 metals (Zn-rich shown). A size distribution is not shown for the ammonium-rich particle class
 1078 due to low ATOFMS particle counts.

1079

1080 maximum, the ammonium-rich particle type contributed $2 \pm 1\%$ by number to the
 1081 unheated d_{va} 892-995 nm size bin. The relatively large size of these unheated ammonium
 1082 nitrate particles is likely due to the Kelvin effect, wherein ammonium nitrate deposits on
 1083 larger particles where surface curvature effects on vapor pressure are minimal (92).

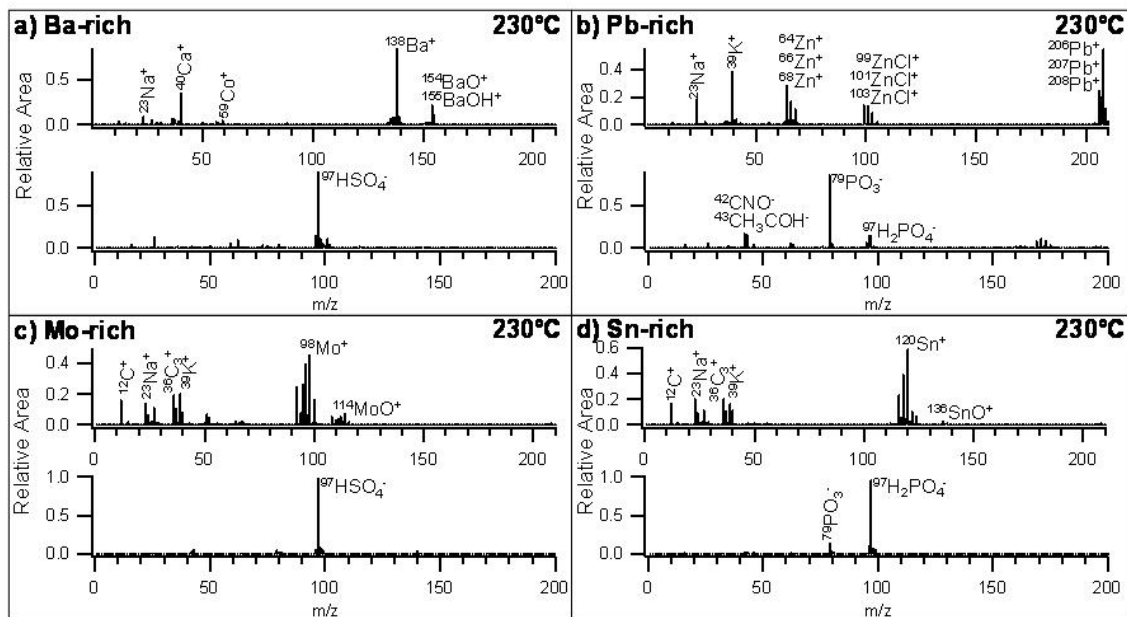
1084 ECOC particle mass spectra are dominated by carbon cluster ions at m/z 12(C^+),
 1085 24(C_2^+), and 36(C_3^+) with less intense OC and amine ion peaks. The negative ion mass
 1086 spectra are characterized by nitrate (m/z -62, NO_3^- , -63, HNO_3^- , and -125, $\text{H}(\text{NO}_3)_2^-$) and
 1087 sulfate. Calcium (m/z 40, Ca^+) and the carbon cluster ions at m/z 48(C_4^+), 60(C_5^+),
 1088 -24(C_2^-), -36(C_3^-), and -48(C_4^-) became more apparent with heating due to the loss of a
 1089 semi-volatile ammonium, OC, and nitrate. Further, the appearance of m/z -79(PO_3^-) with
 1090 heating indicates that m/z -97 can be attributed to both HSO_4^- and H_2PO_4^- ; the loss of
 1091 nitrate with heating causes more electrons to be available in the LDI plume that can
 1092 attach to neutral phosphate and form ions.

1093 The aged sea salt particles were characterized by intense sodium, potassium,
1094 nitrate, and sulfate ion markers with smaller ammonium and carbonaceous ion markers
1095 (76). With heating, ammonium, amines, and nitrate are volatilized from these aged sea
1096 salt particles. The mass spectra of a representative calcium-rich dust particle type are
1097 shown in Figure 13g and are characterized by inorganic peaks at m/z 23(Na^+), 24(Mg^+),
1098 40(Ca^+), 56(CaO^+), 57(CaOH^+), -46(NO_2^-), and -62(NO_3^-) (93). With heating, CN^- (m/z -
1099 26), silicates (m/z -44, SiO^- , and -60, SiO_2^-), and phosphate (m/z -63, PO_2^- , -79, PO_3^- , and
1100 -97, H_2PO_4^-) become prominent with the loss of nitrate. The mass spectra of a
1101 representative zinc-rich particle type are shown in Figure 13h and characterized by zinc
1102 (m/z 64, 66, 68), zinc chloride (m/z 99, 101, 103), nitrate, and phosphate with smaller
1103 carbonaceous ion peaks. With heating, ammonium, OC, and nitrate are volatilized.
1104 Figure 14 shows representative average mass spectra of 230°C heated particles for four
1105 other metal-rich particle types: a) Ba-rich, b) Pb-rich, c) Mo-rich, and d) Sn-rich.

1106 With aging, secondary species can mask particles' primary source "fingerprints".
1107 Thus, heating with the TD can be used to volatilize non-refractory secondary species,
1108 making the primary source signature more identifiable, as described below. Since gas-
1109 particle partitioning occurs more commonly than nucleation in urban environments, an
1110 understanding of the primary particle population is important in understanding urban air
1111 pollution as gas/particle partitioning depends not only on surface area and volume, but
1112 also on the chemistry and resulting interactions on the surface of the available primary
1113 particles (15).

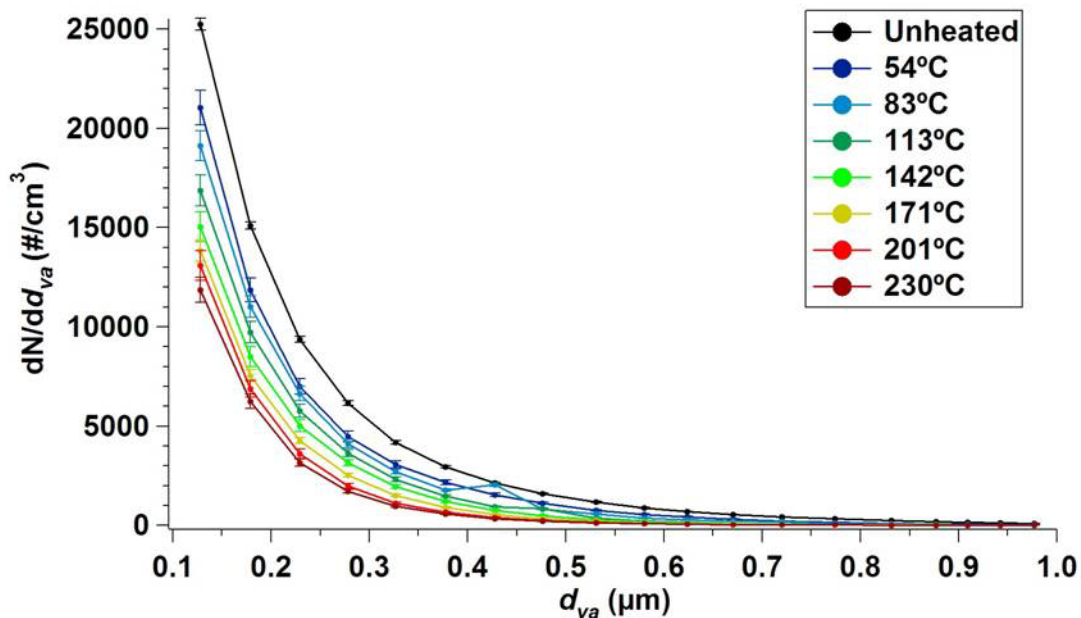
1114 ***b. Chemically-Resolved Volatility***

1115 Overall, a systematic decrease in particle size was observed with heating from
1116 ambient temperature (average 16°C, range 8-26°C) up to 230°C, as shown in Figure 15.
1117 However, the strength of the TD-ATOFMS system is that it directly measures the size-
1118 resolved chemical composition of the individual particle residues following heating,
1119 providing an improved understanding of the original sources of the particle cores. For
1120 the aged OC particles, the most abundant submicron particle type in Riverside, the
1121 particles shifted to smaller diameters with heating from 54-230°C (Figures 11 and 16).



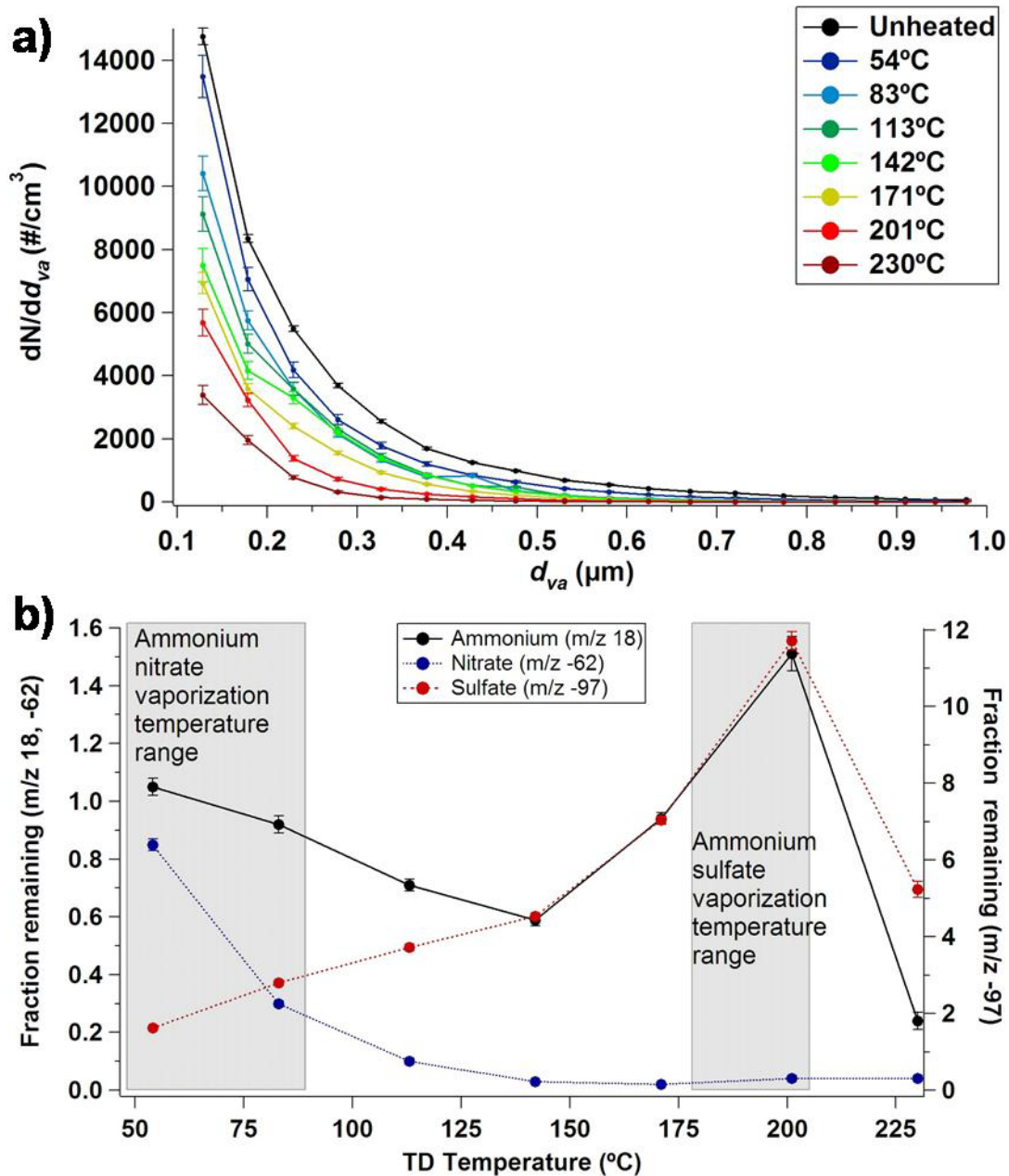
1122
1123
1124
1125
1126

Figure 14: Representative average positive and negative mass spectra of 230°C heated particles for four metal-rich particle types: a) Ba-rich, b) Pb-rich, c) Mo-rich, and d) Sn-rich.



1127
1128
1129
1130

Figure 15: Average size-resolved number concentrations with ~50 nm size bins ($d_{va} = 103-995$ nm) as measured by the SMPS from Nov. 2-13 for ambient temperature to 230°C. Variation over the course of the study is shown by standard error bars.



1131

1132 Figure 16: a) Size-resolved number concentrations of unheated and heated (54-230°C) aged OC
 1133 particles. b) Fractions of ammonium, nitrate, and sulfate remaining at different TD temperatures
 1134 (54-230°C) for aged OC particles with respect to the vaporization temperature ranges of
 1135 ammonium nitrate (94) and ammonium sulfate (72).

1136

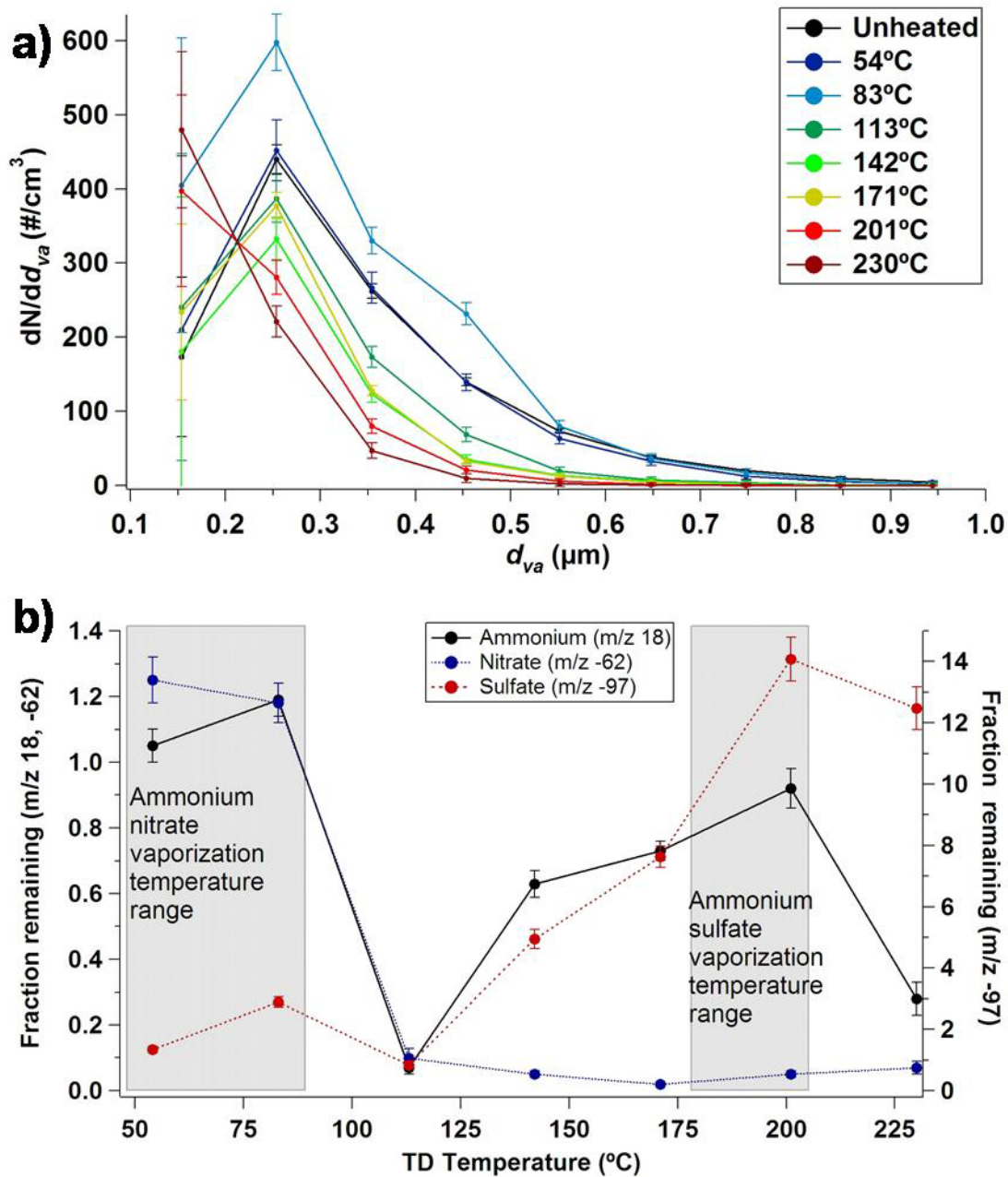
1137 Parallel ATOFMS particle optical measurements showed that these aged OC particles
 1138 were spherical (84), allowing average particle volume to be calculated, from which the
 1139 approximate volume fraction of the average aged OC particle remaining at each TD
 1140 temperature (54-230°C) was calculated. The volatilization of ammonium (m/z 18, NH_4^+),
 1141 nitrate (m/z -62, NO_3^-), and sulfate (m/z -97, HSO_4^-) were then examined with respect to
 1142 TD temperature (54-230°C) for all of the aged OC particles (Figure 16). For comparison,

1143 the vaporization temperature ranges of ammonium nitrate and ammonium sulfate are 48-
1144 89°C (94) and 178-205°C (72), respectively. Through comparison of average volume
1145 and ion marker peak area fractions remaining at different TD temperatures, approximate
1146 contributions of secondary species to the average unheated particle may be calculated.
1147 These are likely conservative estimates as they are biased by the measurement of
1148 particles in the 100-1000 nm (d_{va}) size range, and thus, they cannot account for particles
1149 entering this range from larger sizes ($>1.0 \mu\text{m}$) and leaving this size range as they shift to
1150 the ultrafine mode ($<100 \text{ nm}$). For aged OC particles, ammonium nitrate contributes $22 \pm$
1151 6% to the average particle volume, assuming that ammonium nitrate is the primary
1152 volatile component below 113°C. Further, $\sim 90\%$ of the nitrate was found to be in the
1153 form of ammonium nitrate; the remaining $\sim 10\%$ of the nitrate was found to be primarily
1154 non-volatile aminium nitrate salts (Chapter 5). The decrease in sulfate peak area from
1155 201-230°C was correlated with the decrease in ammonium due to the loss of ammonium
1156 sulfate; considering the volume loss from 201-230°C, ammonium sulfate is estimated to
1157 contribute $19 \pm 9\%$ by volume to the average unheated aged OC particle. Volume loss
1158 from 113-171°C is attributed primarily to the loss of organic carbon species ($6 \pm 7\%$);
1159 however, while organic carbon was observed to volatilize across the temperature range,
1160 some of the organic carbon in the form of oligomers (Chapter 3) remained at 230°C, as
1161 shown by the organic carbon markers in Figure 12. In addition to organic carbon and
1162 aminium nitrate salts, sulfate remaining at 230°C was in the form of sulfuric acid,
1163 aminium sulfate (Chapter 5), and likely organosulfates within these aged OC particles.

1164 The increase in sulfate intensity with heating to 201°C (Figures 17-19) is
1165 hypothesized to be caused by the loss of nitrate, whereby more electrons were available
1166 in the laser desorption-ionization plume to attach to the sulfate and form ions. Recent
1167 SOAR-1 results from Huffman et al. (95) found increased sulfate mass at 142°C
1168 compared to ambient temperature. There is also some evidence of possible
1169 recondensation of ammonium sulfate at 230°C prior to the activated carbon diffusion
1170 denuder (75).

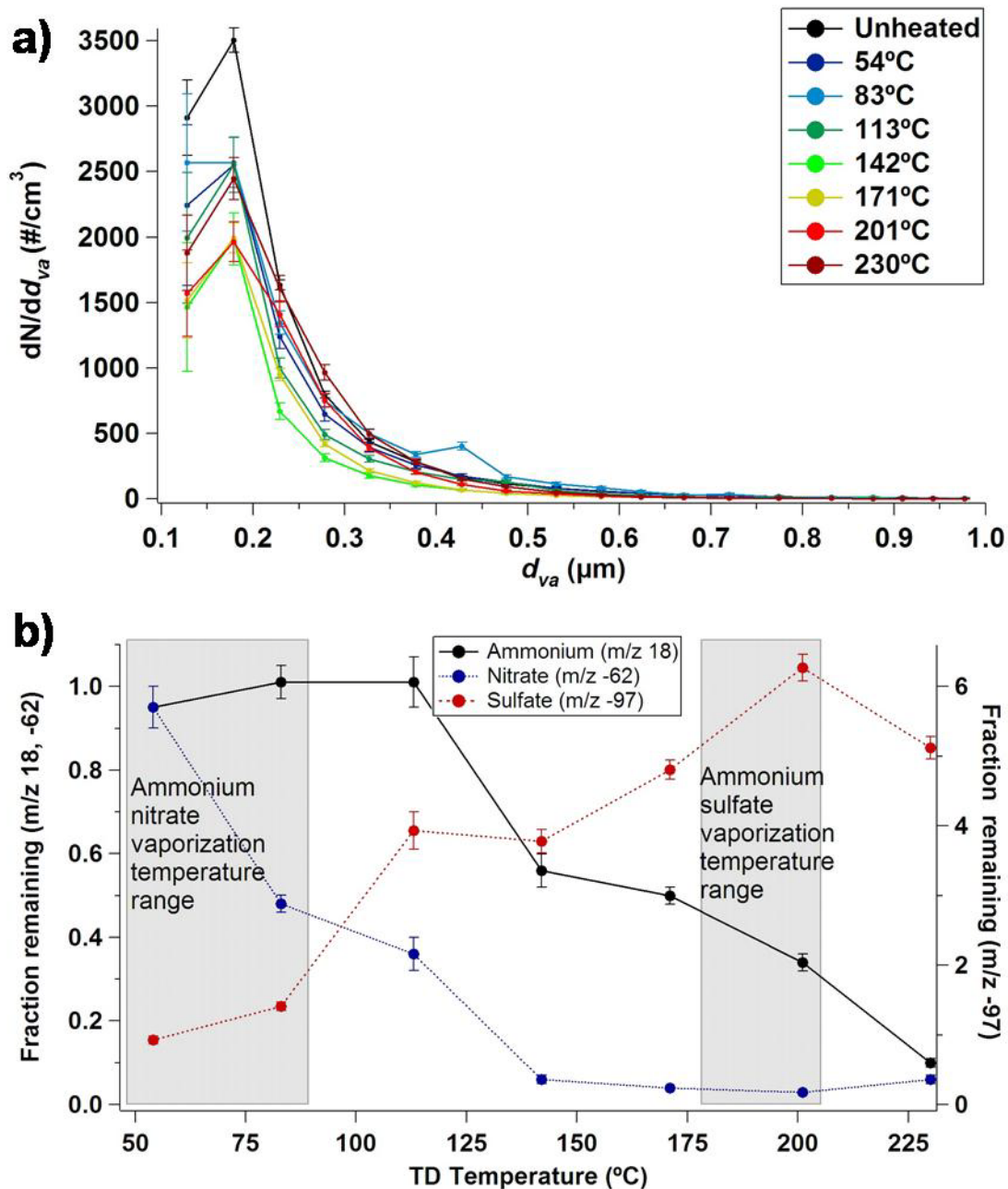
1171 To further investigate the impacts of single-particle mixing state on volatility,
1172 secondary species on vanadium-containing, biomass burning, aged sea salt, and dust
1173 particles were examined (Figures 12, 17, 18, and 19). Similar to the aged OC class,
1174 nitrate was found to be primarily in the form of ammonium nitrate for the vanadium-
1175 containing and biomass burning particle types. However, sulfate remaining at 230°C is
1176 hypothesized to be in the forms of VOSO_4 and K_2SO_4 , which volatilize at 600°C and
1177 above 1000°C, respectively (96-97). For the aged sea salt and dust particle classes, the
1178 heated size distributions of these particle types included supermicron particles that shrank
1179 into the submicron size range with heating, resulting in higher number concentrations at
1180 230°C compared to ambient temperature (see Figure 19). For the aged sea salt class, a
1181 significant fraction of the nitrate and sulfate did not

1182



1183
 1184
 1185
 1186
 1187
 1188

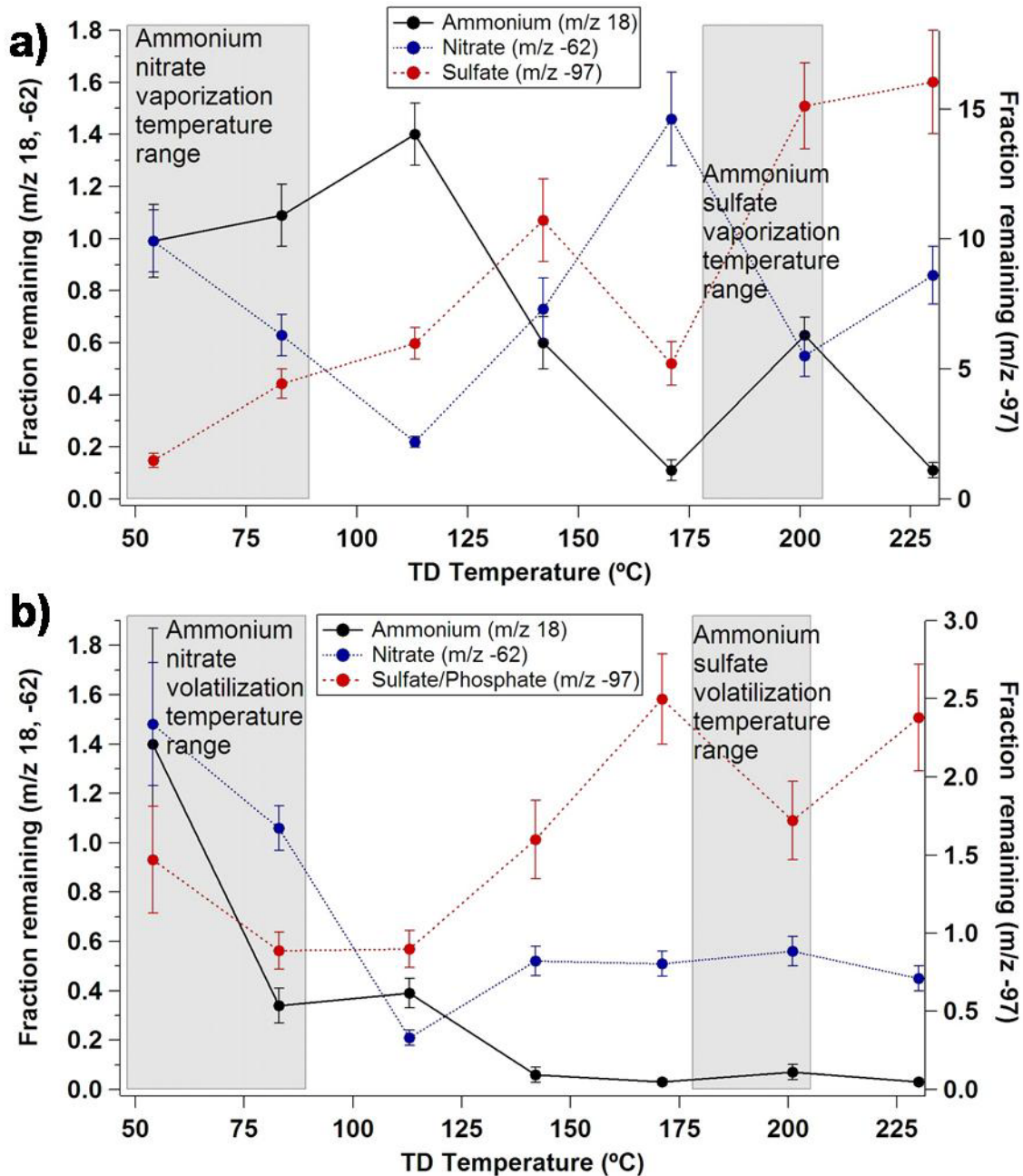
Figure 17: a) Size-resolved number concentrations of unheated and heated (54-230°C) vanadium-containing particles. b) Fractions of ammonium, nitrate, and sulfate at different TD temperatures (54-230°C) for vanadium-containing particles with respect to the vaporization temperature ranges of ammonium nitrate (94) and ammonium sulfate (72).



1189

1190 Figure 18: a) Size-resolved number concentrations of unheated and heated (54-230°C) biomass
 1191 burning particles. b) Fractions of ammonium, nitrate, and sulfate at different TD temperatures
 1192 (54-230°C) for biomass burning particles with respect to the vaporization temperature ranges of
 1193 ammonium nitrate (94) and ammonium sulfate (72).

1194



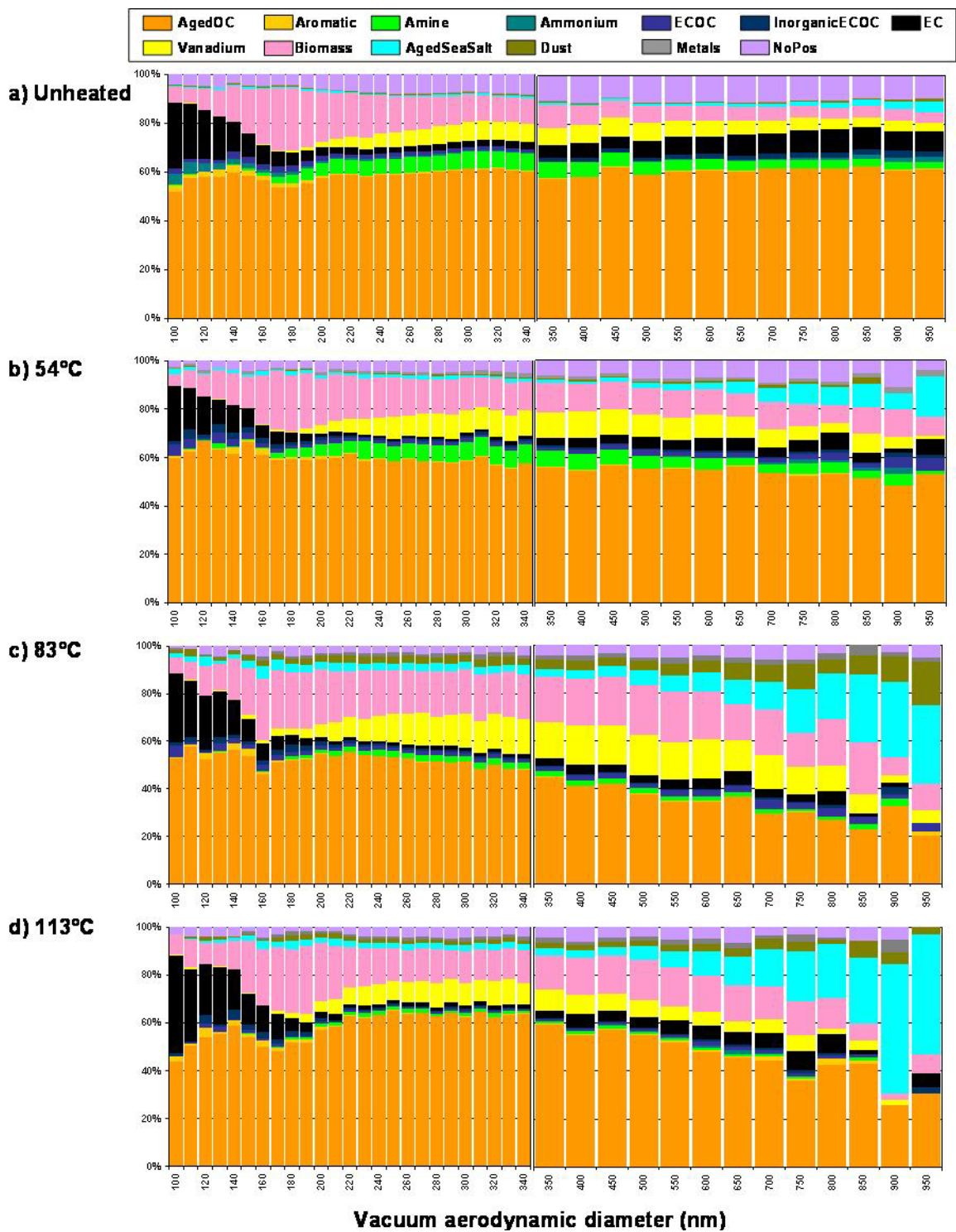
1195
 1196 Figure 19: Fractions of ammonium, nitrate, and sulfate at different TD temperatures (54-230°C)
 1197 for a) aged sea salt and b) dust particles with respect to the vaporization temperature ranges of
 1198 ammonium nitrate (94) and ammonium sulfate (72).
 1199

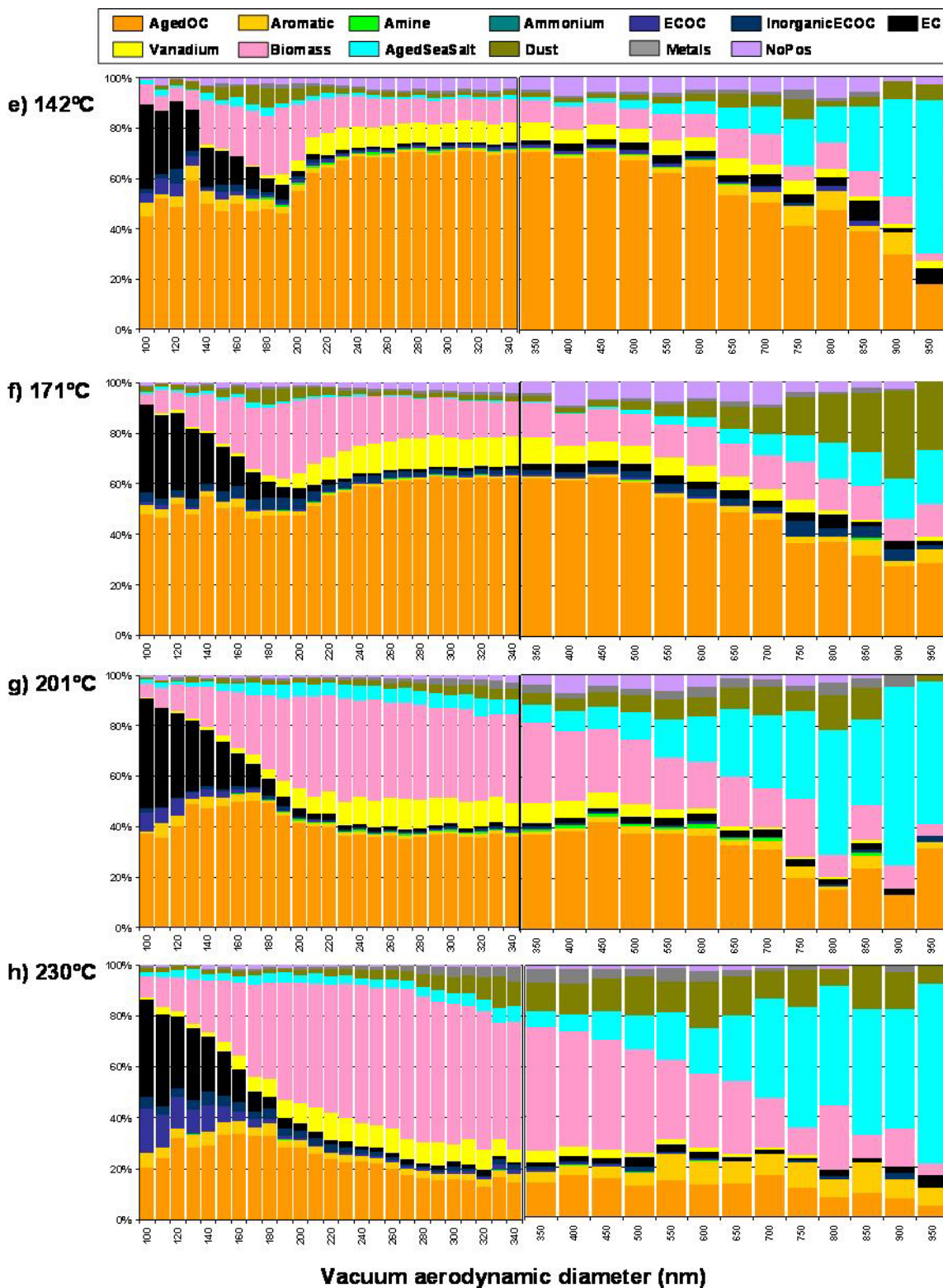
1200 volatilize at 230°C, suggesting nitrate and sulfate were in the forms of NaNO₃ and
 1201 Na₂SO₄, which volatilize at >300°C, similar to NaCl (71). During transport across the
 1202 LA basin, sea salt particles undergo heterogeneous chemical reactions, wherein nitric
 1203 acid and sulfuric acid react with NaCl (77). The average dust particle contained a
 1204 significant fraction of ammonium nitrate; however, nearly half of the nitrate was present
 1205 in non-volatile forms, such as Ca(NO₃)₂. Thus, the volatilities of sulfate and nitrate were
 1206 found to be dependent on particle mixing state. Therefore, the volatility of a particular
 1207 species cannot be assumed to be the same for all particles, even in an aged urban

1208 environment, such as Riverside. Future publications will investigate the predicted versus
1209 measured gas-particle partitioning of various chemical species with respect to season and
1210 particle class.

1211 *c. Aerosol Core Chemistry at 230°C*

1212 The TD-ATOFMS system allowed the complete chemistry of individual ambient
1213 particle cores at 230°C to be measured for the first time. As discussed above, secondary
1214 coatings of ammonium nitrate, organic carbon, and ammonium sulfate volatilized with
1215 heating. Figure 11 shows the relative fractions of particle types observed in Riverside
1216 with respect to size for the 230°C heated particles; the evolution of the size-chemistry
1217 distribution from ambient temperature to 230°C is shown in Figure 20. Two secondary
1218 semivolatile particle types, amine and ammonium-rich, volatilized prior to 230°C. The
1219 abundance of the amine particles, present from ambient temperatures up to 142°C from
1220 ~170-1000 nm, decreased by ~63% with heating above 54°C with only ~8% by number





1222

1223 Figure 20: Size-resolved chemical composition for the 13 general particle types for: a) unheated,
 1224 b) 54°C, c) 83°C, d) 113°C, e) 142°C, f) 171°C, g) 201°C, and h) 230°C. Size resolution is 10
 1225 nm and 50 nm for the ranges of 100-350 nm and 350-1000 nm, respectively.

1226 present above 113°C, suggesting these amine species are quite volatile. The ammonium-
1227 rich particle type, consisting of primarily ammonium nitrate, was not present at 54°C,
1228 consistent with laboratory studies showing a volatilization temperature range of 48-89°C
1229 for ammonium nitrate (72). As these two semivolatile particle types are internal mixtures
1230 of carbonaceous and inorganic species, it is likely that these heated particles shifted to
1231 <100 nm in diameter or became reclassified as aged OC particles following volatilization
1232 of the amines or ammonium nitrate, respectively.

1233 The aged OC and vanadium-containing particle types decreased significantly in
1234 size with increasing temperature, with the majority of remaining particles estimated to be
1235 less than 100 nm in diameter (Figure 11). Aged OC particles accounted for ~60% of the
1236 unheated submicron (100-1000 nm) particles by number; the relative contribution of
1237 these aged OC particles decreased with heating, particularly for the larger (>350 nm)
1238 particles, accounting for only ~20% by number of the 230°C particles across all sizes.
1239 For particles >100 nm, the average aged OC particle diameter decreased from 242 ± 2 nm
1240 to 177 ± 12 nm with heating to 230°C, showing the significant fraction of volatilized
1241 species. Considering the average particle volume, less than $53 \pm 7\%$ by volume of the
1242 average submicron aged OC particle was found to remain at 230°C; this represents an
1243 upper limit since most particles shifted to <100 nm with heating. For the vanadium-
1244 containing particle type, the average particle diameter decreased from 334 ± 35 nm to
1245 201 ± 37 nm with heating to 230°C; this corresponds to a volatile fraction of at least $64 \pm$
1246 15% . Previously, volatility measurements have shown a volume loss of ~80% with
1247 heating to 350°C for submicron urban particles (98).

1248 The size distributions of several particle classes (aromatic, ECOC, inorganic-
1249 ECOC, EC, and biomass burning) did not show significant shifts with heating, as
1250 expected for fresh particles containing smaller fractions of secondary species. Previous
1251 thermogravimetric studies of traffic-related particles showed that, prior to heating at 280°C,
1252 nearly 100% of particles with initial diameters of 150 nm were non-volatile (99). The
1253 biomass burning particle results agree with previous findings that biomass burning
1254 particles are less volatile with a greater fraction of refractory OC than pollution plume
1255 particles (100). In particular, biomass burning particles have relatively large cores due to
1256 the presence of refractory salts, such as KCl and K₂SO₄, which volatilize at temperatures
1257 above 700°C, as well as soot (97,100). The mode positioned at ~180 nm for 230°C is
1258 consistent with that of fresh biomass burning emissions and was the largest of all
1259 combustion-type particles observed (101).

1260 As expected, the aged sea salt and dust particles had the largest particle diameters
1261 at 230°C. As discussed in the above section, the fractional contributions of aged sea salt
1262 and dust particle types increased with heating primarily due to the volatilization of
1263 semivolatile coatings and water from supermicron particles (76). The increased
1264 contributions of sea salt and dust particles to the larger submicron particle cores can be
1265 seen in Figure 11.

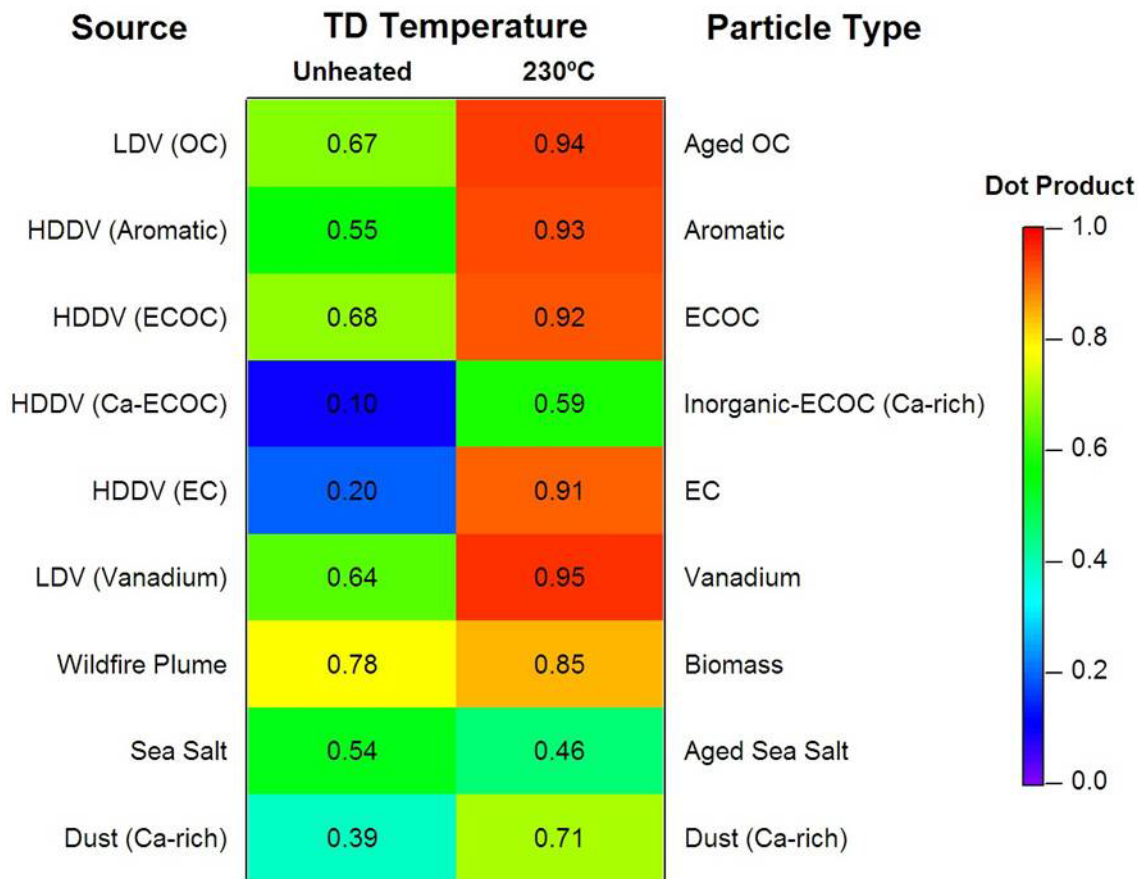
1266 With heating, the percentage of particles with metal signatures increased by a
1267 factor of 6 at 54°C, due to the volatilization of semivolatile species, causing these
1268 particles to be reclassified as metal-rich. The most abundant metals observed at 230°C
1269 included vanadium, zinc, barium, lead, molybdenum, and tin (Figures 11, 13, and 14).
1270 Posing negative human health effects, trace metals present in particulate matter are of
1271 considerable importance (69). However, small metal particles produced in combustion

1272 fumes quickly become coated in the atmosphere, making detection difficult. A detailed
1273 discussion of the mass spectral signatures, sources, and temporal patterns of metal-rich
1274 particles detected during SOAR is presented elsewhere (102); however, it is important to
1275 note that metals are not typically detected in aged environments by single particle mass
1276 spectrometry as they are masked by high levels of secondary coatings. Based on these
1277 thermodenuder results, it appears they must be masked by high levels of secondary
1278 coatings, suggesting that the overall fraction of metal-containing particles is greater than
1279 previously estimated (102). However, there is some evidence of toxicity related to the
1280 chemical composition of the particle surface (69), and, thus, studies are needed to
1281 determine the relative toxicity of coated (aged) versus uncoated metal-containing
1282 particles. Future laboratory studies will quantify the amount of secondary coatings
1283 necessary to mask these trace metal signals and examine corresponding health impacts.
1284 In summary, at 230°C, the main particle types present from 100-150 nm were elemental
1285 carbon (29% by number), OC (27%), and biomass burning (15%). Correspondingly,
1286 biomass burning (51%) and OC (25%) were the primary particle types at 200-250 nm,
1287 and sea salt (47%) and dust (15%) were found at 750-800 nm. Future studies will size-
1288 select particles prior to TD heating to better quantify the fractions of secondary species
1289 versus particle core. The TD-ATOFMS method has provided insight into the
1290 contributions of different forms of secondary species, such as ammonium nitrate vs.
1291 sodium nitrate, with respect to individual particle cores.

1292 *d. Comparison of Particle Cores with Source Emissions*

1293 If the semivolatile material volatilized from the particle phase at 230°C is
1294 composed of mostly secondary species, then the particle core should resemble non-
1295 volatile primary particle-phase source emissions. To test this hypothesis, the mass
1296 spectral signatures of the aged unheated and 230°C heated particles were each compared
1297 to freshly emitted particles from previous source studies, described in the supporting
1298 information, using a method similar to Toner et al. (79). Briefly, the mass spectral
1299 signatures of the SOAR-2 particle types were compared to the mass spectral signatures
1300 resulting from various source studies; dot products were calculated for the ion peaks in
1301 the compared spectra (Figure 21). Lower dot products (i.e. blue) indicate less similarity
1302 between the SOAR-2 and source particles; whereas high dot products (i.e. red) indicate
1303 more similarity. To examine the similarity of the unheated and 230°C heated aged OC
1304 particles, the mass spectra were compared, giving a dot product of 0.62, illustrating the
1305 dramatic change in particle chemical composition with heating. The aged OC particles
1306 were likely primary combustion emission particles transformed by the accumulation of
1307 the secondary reaction products (103). It is likely that ammonium nitrate, ammonium
1308 sulfate, amines, and organic carbon were acquired due to condensation and aqueous-
1309 phase processing during the night when lower temperatures and higher relative humidity
1310 (average 72%, range of 16-96%) were encountered (104). Following removal of
1311 semivolatile species with heating to 230°C, concurrent with a decrease in particle size,
1312 the heated OC particle mass spectral signature was nearly identical to that of fresh OC
1313 particles emitted from light duty vehicles (LDV)

1314



1315

1316 Figure 21: Dot product comparisons of mass spectral signatures of freshly emitted source
 1317 particles (light duty vehicles (LDV), heavy duty diesel vehicles (HDDV), wildfire, sea salt, and
 1318 dust) with unheated and 230°C heated SOAR-2 particles.

1319

1320 (86). The dot product between the LDV emissions (86) and Riverside particles increases
 1321 with heating from 0.67 for the unheated particles to 0.94 for the 230°C heated aged OC
 1322 particles.

1323 Other heated particle types also resembled fresh vehicle emissions (Figure 21).
 1324 For the aromatic particle type (Figure 13), similar polycyclic aromatic hydrocarbon
 1325 (PAH)-containing particles have been previously identified in heavy duty diesel vehicles
 1326 (HDDV) and LDV emissions (86-87). The dot product comparison between HDDV
 1327 aromatic particle emissions and these Riverside particles improves with heating from
 1328 0.55 to 0.93, showing a nearly identical signature to HDDV emissions at 230°C.
 1329 Similarly, the mass spectral signature of the ECOC particle type resembles fresh HDDV
 1330 emissions previously detected by ATOFMS (87) with the dot product increasing from
 1331 0.68 to 0.92 with heating. The Ca-rich ECOC particles were likely residual oil particles
 1332 from HDDV exhaust (105); Na/K-dominant ECOC particles were likely unburned fuel
 1333 particles from LDV exhaust (106). The 230°C Ca-rich ECOC particles showed an
 1334 improved match (0.59) to the HDDV Ca-ECOC (105) compared to the unheated particles
 1335 (0.10); however, the relatively low dot product observed for the heated Ca-ECOC
 1336 particles suggests that another unidentified source could also be contributing to these
 1337 particles. The EC mass spectral signature resembles fresh HDDV emissions (87) with the

1338 dot product increasing from 0.20 to 0.91 with heating. The heated vanadium-containing
1339 particles were an excellent match to vanadium-containing LDV particles (86) (0.95) and
1340 vanadium-containing ship emissions (80) (0.94), increasing from 0.64 and 0.62 for the
1341 unheated particles, respectively.

1342 For unheated particles characterized by distinctive source signatures, the results
1343 were mixed. Comparison of the aged biomass particles with fresh biomass particles
1344 collected within a wildfire plume provides a good match with both the unheated (0.78)
1345 and 230°C heated particles (0.85) since potassium dominates the comparison. Unlike
1346 other particle types, the dot product between fresh sea salt and the aged sea salt does not
1347 increase with heating (0.54 vs. 0.46), due to the irreversibility of chloride replacement by
1348 nitrate and sulfate during atmospheric aging. The mass spectral signature of the heated
1349 aged dust particles is similar to that of fresh suspended dust particles (81) with a dot
1350 product of 0.71 compared to 0.39 for the unheated dust; however, similar to the sea salt,
1351 the lower observed dot product for the heated dust particles is due to irreversible
1352 heterogeneous chemical reactions.

1353 Thus, the TD-ATOFMS method has been shown to apportion particles in highly
1354 aged environments to their original sources, while providing insight into the relative
1355 contributions of primary and secondary species. Future TD-ATOFMS studies in different
1356 environments are expected to further our understanding of primary particle sources and
1357 gas/particle partitioning.

1358 **iv. Acknowledgements**

1359 The authors acknowledge Paul Ziemann (UC-Riverside), Ken Docherty (CU-
1360 Boulder), and the UC-Riverside Air Pollution Research Center for support during SOAR-
1361 2 and Alex Huffman and Jose Jimenez (CU-Boulder) for use of the TD system. Mike
1362 Cubison (CU-Boulder) provided SMPS data. Megan McKay and the Goldstein group
1363 (UC Berkeley) provided ambient temperature and relative humidity data. The authors
1364 thank the Prather group, particularly Laura Shields, Xueying Qin, and Stephen Toner, for
1365 support during SOAR-2. This work was supported by the California Air Resources
1366 Board. K. Pratt was funded in part by an NSF Graduate Research Fellowship (2006-
1367 2009) and an EPA STAR Graduate Fellowship (2005-2006).

1368

1369 **3. Source apportionment of PM_{2.5} in Athens (Greece) and Mexico City using**
1370 **an ATOFMS derived mass spectral source library**

1371

1372 **i. Introduction**

1373 Proper source apportionment of ambient particles is important with regards to
1374 understanding their origin, as well as determining the roles they may play in the
1375 environment and affecting human health. The ability to apportion ambient particles
1376 quickly and accurately will be very helpful for environmental and health agencies and for
1377 monitoring and enforcing emission standards. This kind of application is also useful for
1378 global climate and pollution modelers who desire to know the contribution of specific
1379 sources in a given region rather than using estimated numbers from emission inventories
1380 (107-111). Traditional methods of ambient aerosol classification and apportionment
1381 typically use filter or impactor based applications where aerosols are collected on a
1382 substrate and then analyzed with offline techniques (112-114). Other methods have
1383 apportioned particles to sources based strictly on the size distribution and concentration
1384 of ambient aerosols (115-117). More recent techniques using mass spectrometry on
1385 single particles, such as aerosol time-of-flight mass spectrometry (ATOFMS) (35,118),
1386 have proven very useful for determining the size resolved chemical composition of
1387 aerosols (48,119-121). One of the issues with the single particle mass spectrometry
1388 techniques is that the classification, labeling, and apportionment of particles based on
1389 their mass spectrum is dependent upon user interpretation. This can result in
1390 inconsistencies with labeling of similar classes and apportionment.

1391 The methods for ATOFMS single particle data analysis and classification have
1392 been developing and progressing over the years. Some methods have included: sorting
1393 through individual spectra by hand, which can be extremely time consuming for large
1394 datasets; simple m/z peak searching using basic table database structures; and databases
1395 where mathematical algorithms can be used to cluster the data based on user defined
1396 parameters. The major progress has come from incorporating data clustering methods
1397 with mathematical algorithms such as ART-2a, K-means, and Hierarchical Clustering (7-
1398 9,122-123). These techniques have been shown to accurately cluster particle spectra
1399 within given similarity thresholds (8-9,119,124-126). These methods fail to label (or
1400 classify) the particle types they have been used to cluster. That process is still determined
1401 by the user which can succumb to biases or overly generalized classification. The use of
1402 a mass spectral source library for apportioning ATOFMS single particle data has been
1403 described and shown to work with minimal error in a fresh emission environment (127-
1404 128). The next progressive step is to use the method on more aged environments and/or
1405 other global areas to see if a mass spectral library developed for one location is
1406 representative of the same sources around the world. The goal of this study is to test the
1407 mass spectral source library matching method on ATOFMS data collected in more
1408 polluted environments (Athens, Greece and Mexico City) to determine if the library
1409 signatures are applicable in other locations and with other ATOFMS instruments.

1410 **ii. Experimental**

1411 The use of a single mass spectral library for source apportionment of ATOFMS
1412 data, for any sampling location, is a very desirable commodity. To date, ATOFMS
1413 ambient particle mass spectral data are typically clustered using the ART-2a algorithm
1414 and then visually characterized (119,129). The inherent weakness of such a method is
1415 that user bias can sway the classification results, and the homogeneity of an ART-2a
1416 cluster can vary depending on the parameters used for clustering. Using a mass spectral
1417 library, built from ART-2a generated clusters from various source characterization
1418 studies, is a novel approach to eliminating user bias when classifying single particle data.
1419 This approach can also help reduce misclassification of particles because the clusters
1420 within the source library do not change as particles are added to them during the
1421 apportionment step. The library matching method uses a variation of the ART-2a
1422 algorithm known as match-ART-2a (www.yaada.org) (130). This method is different
1423 than the standard ART-2a clustering method by having particle clusters (or seeds) already
1424 defined. These seeds are the particle source signatures from the source library which are
1425 described below. As particle spectra are compared mathematically, taking the dot
1426 product, to the seed spectra in the library, they either will match to specific source seeds
1427 above a defined vigilance (or similarity) factor (VF), or they may not match to any of the
1428 source seeds. If the particle matches to a particular source seed above a designated dot
1429 product VF threshold, then the particle is assigned to that type. If the particle matches to
1430 two or more different source seeds above the VF, then it will be assigned to the one that
1431 provided the highest dot product. The dot product values range between 0 and 1, where a
1432 dot product of 1 means the particle spectra are identical. Particles that do not match to
1433 any of the source seeds are grouped in an unclassified category.

1434 The current source library contains seeds for seven specific sources (gasoline
1435 powered light duty vehicles (LDV), heavy duty diesel vehicles (HDDV), biomass
1436 burning, dust, sea salt, meat cooking, and industrial emissions) and has seeds for seven
1437 other general particle types (elemental carbon (EC), aged organic carbon (aged OC), aged
1438 elemental carbon (aged EC), amines, PAH's, vanadium-containing, and NH₄-containing)
1439 for particles that may not match into any of the seven specific sources. The source
1440 specific seeds were obtained from both laboratory and ambient field studies conducted
1441 with the ATOFMS. For example, the HDDV and LDV clusters were generated from data
1442 acquired from dynamometer studies as well as from a freeway-side study. Likewise, the
1443 dust source signatures were obtained from lab studies of resuspended dust and soil as
1444 well as from dust particle classes detected from various ATOFMS studies around the
1445 world. The sea salt, industrial, and non-source specific seeds were generated exclusively
1446 from particle classes detected from ATOFMS ambient studies. The non-source specific
1447 aged types were created from ATOFMS ambient studies where the particle types exhibit
1448 ion peaks attributed to aging (i.e. SOA, nitrate, sulfate, and ammonium) and are to
1449 convoluted to assign to a specific source. While there are not a vast amount of specific
1450 sources currently in the library, the current types represent major particle types found in
1451 urban, marine, and rural areas (112,131-139). The library is adaptive and can have more
1452 source signatures added to it as future source characterization and ambient studies are
1453 conducted. Such sources include a variety of industrial emissions, coal combustion, and
1454 cigarette smoking, as well as increasing the detail on the vehicle source seeds and with
1455 more aged source particle types.

1456 It is very important to test the source library on multiple ATOFMS instruments in
1457 order to insure that they can be universal for the ATOFMS community around the world.
1458 The library, as it currently stands, is not completely universal just yet. Since the library is
1459 open-source, it can always have new source spectra added to it or even have ones
1460 removed if they are found to interfere with proper apportionment. The idea is for the
1461 library to be openly available to the ATOFMS community and for it to evolve as users
1462 modify the library with their own source data.

1463 The source signature library matching technique was previously tested on
1464 ATOFMS ambient data obtained in a location dominated by “fresh” emissions near a
1465 freeway (Chapters 4 and 5) (127-128). To test whether particles can be apportioned in
1466 different environments, as well as with ATOFMS instruments used by different research
1467 groups, data from two different global locations were chosen. The first study is Athens,
1468 Greece (37°59'12.24"N 23°43'30.73"E), which was conducted in August of 2003 using a
1469 TSI 3800 ATOFMS owned and operated by the Harrison research group out of the
1470 University of Birmingham (140). The second study is Mexico City, Mexico
1471 (19°29'23.60"N 99°08'55.60"W), which was conducted in March of 2006 with an in-
1472 house built ATOFMS instrument that was also used for some of the original source
1473 characterization studies used to build the source library (141). The experimental methods
1474 as well as the general classification of the particles are described for both studies in the
1475 literature (140-141). The ATOFMS data from both of these studies were analyzed
1476 (separately) using the source library with match-ART-2a at a VF of 0.85 which represents
1477 a very high VF. This is the same VF used in Chapter 4 which showed a low error of 4%
1478 for aerosol apportionment at VF = 0.85 (127). The same VF is used again for this study
1479 to test if such a high VF can be used to apportion particles in more polluted (and aged)
1480 regions. The effect of varying the VF are shown and discussed in the Appendix 3. The
1481 source apportionment results from the mass spectral library matching method are
1482 discussed and compared to the traditional ART-2a classified particles reported in the
1483 literature for both studies (140-141).

1484 **iii. Results and Discussion**

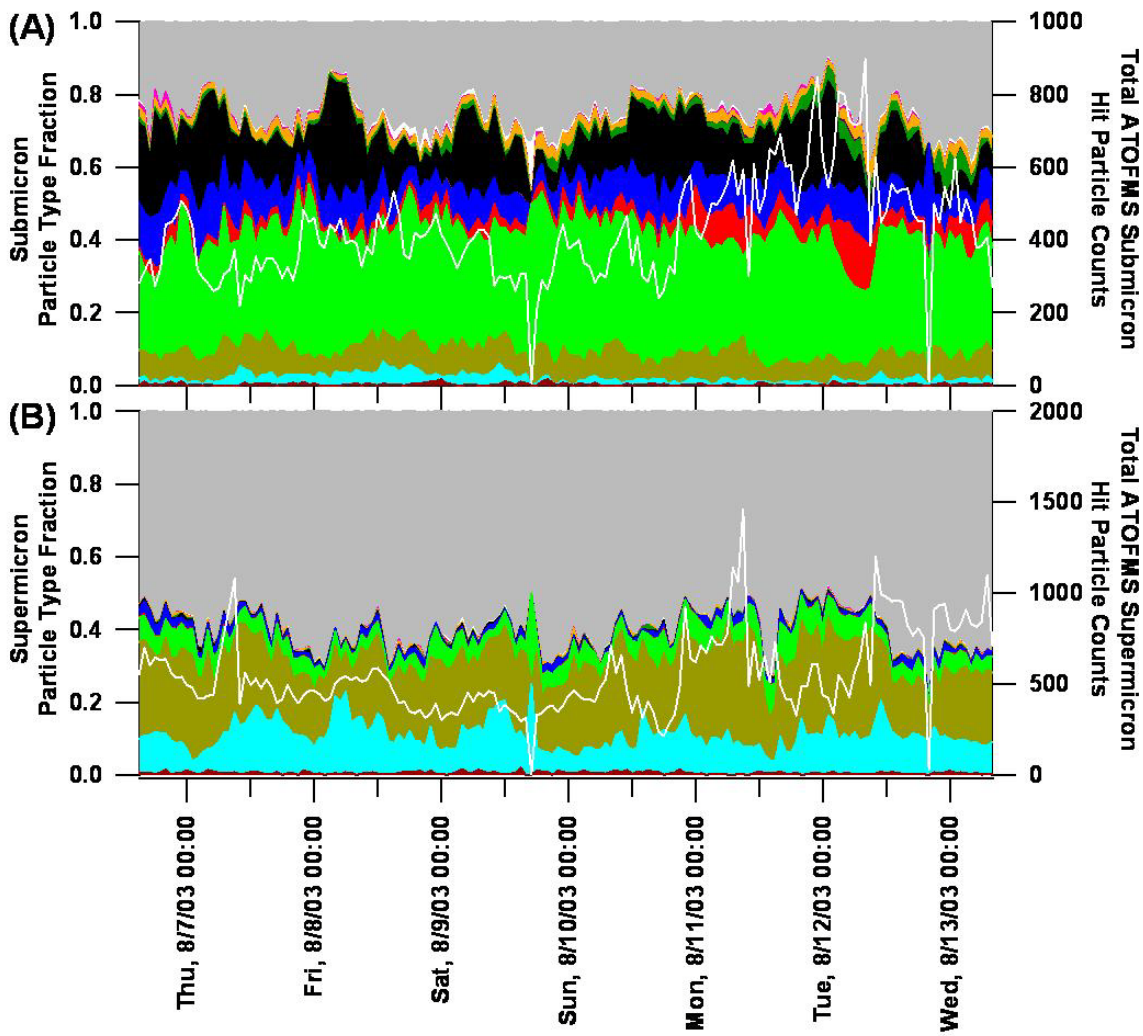
1485 ***a. Source apportionment of ambient particles in Athens, Greece***

1486 The ambient particles detected with the ATOFMS used by Dall'Osto et al. in
1487 Athens, Greece were analyzed using the match-ART-2a technique with the mass spectral
1488 source signature library. As was previously mentioned, a VF of 0.85 was used for the
1489 library matching process. For this particular analysis, the submicron (200 – 1000 nm)
1490 and supermicron (1000 – 3000 nm) particles were analyzed separately in order to
1491 illustrate the chemical differences that typically distinguish the two modes. The
1492 submicron mode particles are typically due to combustion sources and/or agglomeration
1493 and condensation processes, while the supermicron mode aerosols are typically
1494 represented by mechanically driven processes. Figure 22 shows the temporal series of
1495 the submicron (Figure 2A) and supermicron (Figure 22B) apportioned particles along
1496 with their respective total ATOFMS particle counts (white trace). It is apparent by
1497 looking at Figure 22 that there is a large number of particles that are not apportioned to
1498 any sources (i.e. unclassified) by this matching process at VF = 0.85. The reason for this
1499 is because the data collected for this study has many spectra with low signal to noise and

1500 a large fraction (~15% in the submicron and over 35% in the supermicron) of spectra
1501 with miscalibrated peaks (140). These noisy and miscalibrated spectra typically do not
1502 match to the source library spectra, especially at a high VF of 0.85, as their ion peaks
1503 simply do not match. For this reason, matching was also carried out at a lower VF and
1504 with a different technique using only the positive ions for the unclassified particles to see
1505 how these parameters affect the matching process.

1506 As shown in Figure 22A, biomass burning contributes to the majority (~33%) of
1507 ambient submicron particles. This result agrees with findings in Dall'Osto et al., 2006;
1508 however, the particles attributed to biomass by library source matching were more
1509 generically labeled as secondary carbon by Dall'Osto et al. Despite being labeled as
1510 secondary carbon by Dall'Osto et al., inspection of these particles revealed that they
1511 contain a large peak due to potassium and exhibit very strong similarities to the biomass

■ Industrial ■ Sea Salt ■ Dust ■ Biomass ■ LDV ■ HDDV ■ Meat Cooking ■ EC Pos Only
■ Vanadium Rich ■ Aged EC ■ Aged OC ■ Amine □ PAH ■ NH₄ Rich ■ Unclassified
 (White trace = Total ATOFMS hit particle counts)



1512

1513 Figure 22: Temporal series of the mass spectral source library matching results for
 1514 Athens, Greece ambient A) submicron particles; and B) supermicron particles.

1515

1516 signatures (matching with dot products > 0.9). The summer of 2003 produced record
 1517 temperatures and an intense wildfire season throughout Europe. These wildfires have a
 1518 major impact on the air quality over the Mediterranean area (142), and explain why
 1519 biomass aerosols appears as a consistent background during this study. Since these
 1520 biomass particles have been transported to the Athens site, it is likely that much of the
 1521 carbon they contain is due to the uptake of secondary organic carbon. Elemental carbon
 1522 particles (EC Pos Only) make up the next largest fraction (14%) of particles for the
 1523 submicron mode. This particle type has been shown before to correlate with vanadium
 1524 particles in a coastal environment, and may be indicative of ship emissions (128,143).

1525 The other major contributors to the submicron particles are dust, HDDV, and LDV at 7%,
1526 9%, and 4% respectively. There are also more minor contributions from sea salt, aged
1527 OC, vanadium, amines, and industrial emissions. It is interesting to note that there is no
1528 strong diurnal variation for any of the source fractions, nor with the total ATOFMS
1529 submicron counts. This may be another indication of a fairly constant regional
1530 background as described for the biomass particles.

1531 As can be seen in Figure 22B for the supermicron mode, the majority of the
1532 classified particles are from dust (21%) and sea salt (11%). Both local and transported
1533 dust have been shown to be a major fraction to the particulate matter in Athens in prior
1534 studies (144-146), as well as by Dall'Osto et al. for this study (140). This is a good
1535 indication that the matching results for the classified particles are accurate. The particles
1536 apportioned to sea salt do show some temporal variations, which may a function of local
1537 winds. Since much of Greece is surrounded by the Mediterranean Sea, and the closest
1538 coastline to the sampling site is 6.5 km, it seems very reasonable that there be a
1539 contribution from sea salt to the supermicron mode. As shown in Figure 22B, almost
1540 60% of the supermicron particles were not classified by the library matching technique
1541 though. As stated earlier, this is because over 35% of the supermicron spectra have
1542 miscalibrated ion peaks for this study. Also contributing to the supermicron mode are
1543 particles from biomass burning, industrial emissions, diesel emissions, and some aged
1544 OC and amines. The matching percentages for each source are summarized in Figure 28.

1545 Figure 23 shows the size resolved source apportionment of the ATOFMS detected
1546 ambient particles for Athens, Greece. As can be seen in this figure, biomass particles
1547 represent the major fraction of the submicron particles, but only down to 250 nm. To
1548 note, the biomass particles are not 100% pure biomass particles since they have
1549 transported to the Athens site and contain secondary species (organics, nitrate, and
1550 sulfate) on them. The influence from both HDDV and LDV emissions can be seen
1551 throughout the full size range of the submicron particles, but below 250 nm the influence
1552 from diesel emissions is detected as the major particle type. As described by Dall'Osto et
1553 al., the sampling site was located alongside a road with moderate traffic, with more
1554 trafficked roads in relatively close proximity to the site. These findings agree with other
1555 roadside studies, even with high LDV to HDDV traffic ratios, that the smaller particles

Particle Source	Matching VF = 0.85		Matching VF = 0.85**		Matching VF = 0.75	
	Sub %	Super %	Sub %	Super %	Sub %	Super %
Industrial	0.29	0.54	0.72	1.37	0.48	1.23
Sea Salt	1.78	10.45	2.77	19.30	2.66	19.36
Dust	7.18	21.09	11.95	38.64	11.62	41.81
Biomass	32.56	5.11	34.41	6.30	36.57	7.06
LDV	4.30	0.12	5.02	0.18	8.33	0.28
HDDV	8.90	1.42	8.90	1.42	10.37	4.27
Meat Cooking	0.01	0.00	0.01	0.00	0.01	0.00
EC (Positive only)	14.03	0.35	14.03	0.35	13.44	0.37
Vanadium Rich	1.82	0.15	2.04	0.26	2.60	0.29
Aged EC	0.07	0.00	0.07	0.00	0.09	0.00
Aged OC	2.34	0.36	2.34	0.36	4.73	1.02
Amine Containing	0.39	0.07	0.60	0.14	1.36	0.14
PAH Containing	0.62	0.07	0.62	0.07	0.06	0.04
NH4 Containing	0.00	0.00	0.00	0.00	0.00	0.00
Unclassified	25.72	60.26	16.51	31.60	7.69	24.13

Sub = Submicron particles (200-1000nm)

Super = Supermicron particles (1000-3000nm)

** Matching at VF = 0.85 including rematching unclassified particles using positive ion only matching

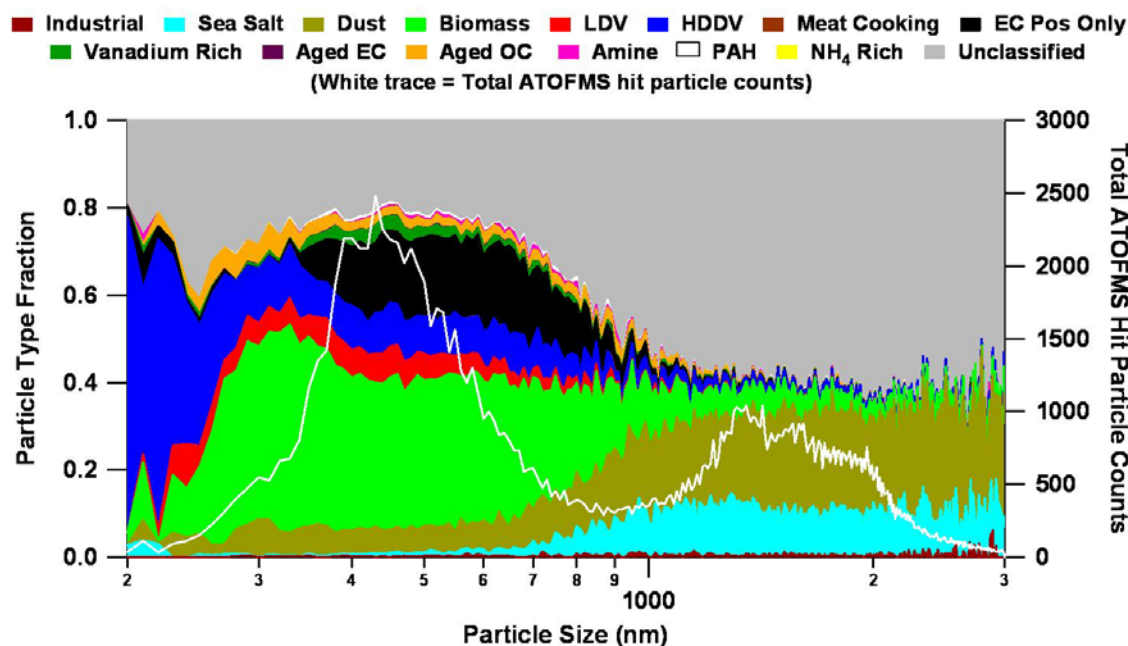
1556

1557

1558

1559

Figure 23: Percent of Athens, Greece particles matched to the mass spectral source library at different match-ART-2a Vigilance Factors (VF)



1560

1561

1562

Figure 24: Size resolved source apportionment of the ATOFMS detected ambient particles for Athens, Greece.

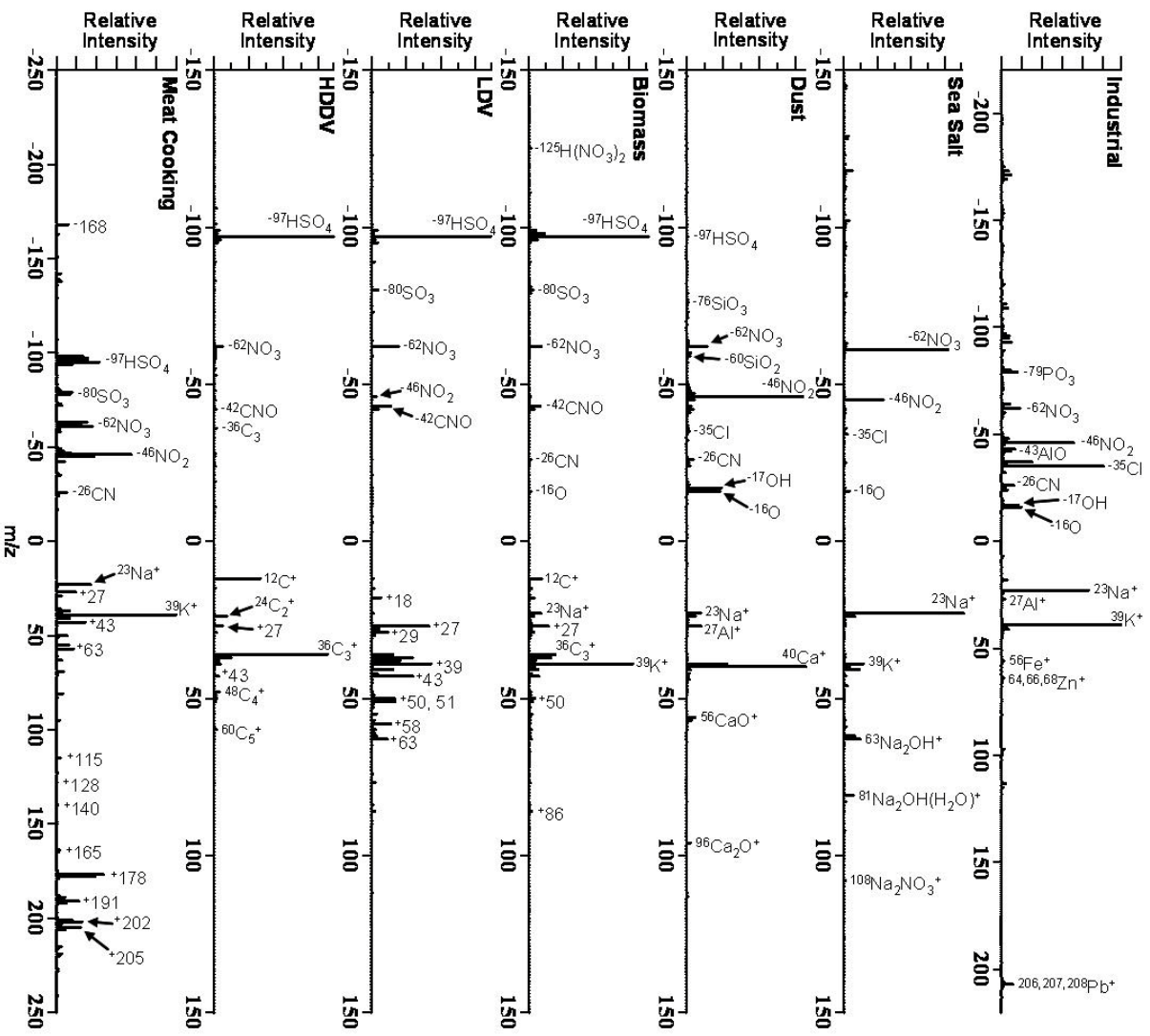
1563 will be dominated by vehicle traffic of which diesel emission can be the largest
1564 contributor (117,127,147-149). The EC positive ion only type as well as vanadium
1565 particles are shown to peak between 300 and 1000 nm, just as in a previous coastal
1566 ATOFMS study (128). As was discussed in Chapters 4 and 5, these two classes
1567 combined in this size range may be due to ship emissions, however their temporal R^2
1568 correlation for Athens is 0.5, which may indicate separate sources for this site. The
1569 analysis of a current ATOFMS study is underway to determine if these signatures are
1570 ship emissions (143). As discussed for Figure 22B, it can be seen that both dust and sea
1571 salt make up the majority of the classified particles in Figure 23.

1572 ***b. Source Signature Matching for Athens, Greece***

1573 While the ATOFMS mass spectral library contains many spectra for each source,
1574 it is interesting to examine the top spectra to which the particles are matched for each
1575 study. Figure 24 shows the top library spectra that the ambient Athens particles matched
1576 to for each specific source, while Figure 24 shows the top non-source specific source
1577 spectra that were matched. The particle types are listed in order (as in Figures 22 and 23)
1578 across Figures 24 and 25.

1579 Despite not being one of the major particle types in the Athens ambient aerosol, it
1580 is interesting to note that the particles which match to the industrial spectrum (Figure 24)
1581 are matching to a library cluster that was produced from the Mexico City dataset. This
1582 industrial particle type is characterized by the large ion signals due to sodium and
1583 potassium, as well as the presence of aluminum, iron, zinc, and lead, as described in the
1584 literature (141). Such particles, described by Moffet et al., are consistent with those
1585 associated with high temperature combustion sources such as waste incinerators
1586 (141,150). Particles containing these metals have also been detected in prior Athens
1587 aerosol characterization studies (151-155).

1588 The top sea salt, dust, biomass, LDV, and HDDV library clusters that were
1589 matched are typical of those seen in other ATOFMS studies (81,105,140,156-159). The
1590 majority of the sea salt and biomass particles detected for this Athens study show signs of
1591 aging due to the uptake and oxidation of NO_x species. The biomass particles, as well as
1592 the HDDV and LDV particles, also show the presence of HSO_4^- (m/z -97) and SOA (m/z
1593 +43). The top dust type for Athens is dominated by the presence of calcium which is
1594 consistent with the findings by Dall'Osto et al., and others for Athens $\text{PM}_{2.5}$ (140,144-
1595 145). This dust type has been shown to be transported from the Saharan desert in
1596 previous studies and is commonly detected in the Mediterranean area (145-146,160-161).
1597 The presence of the large nitrate ion peak (m/z -62) is also an indication that this dust
1598 type has been transported and aged.



1599
 1600 Figure 25: The top matching mass spectral signatures for each source for Athens,
 1601 Greece ATOFMS data.

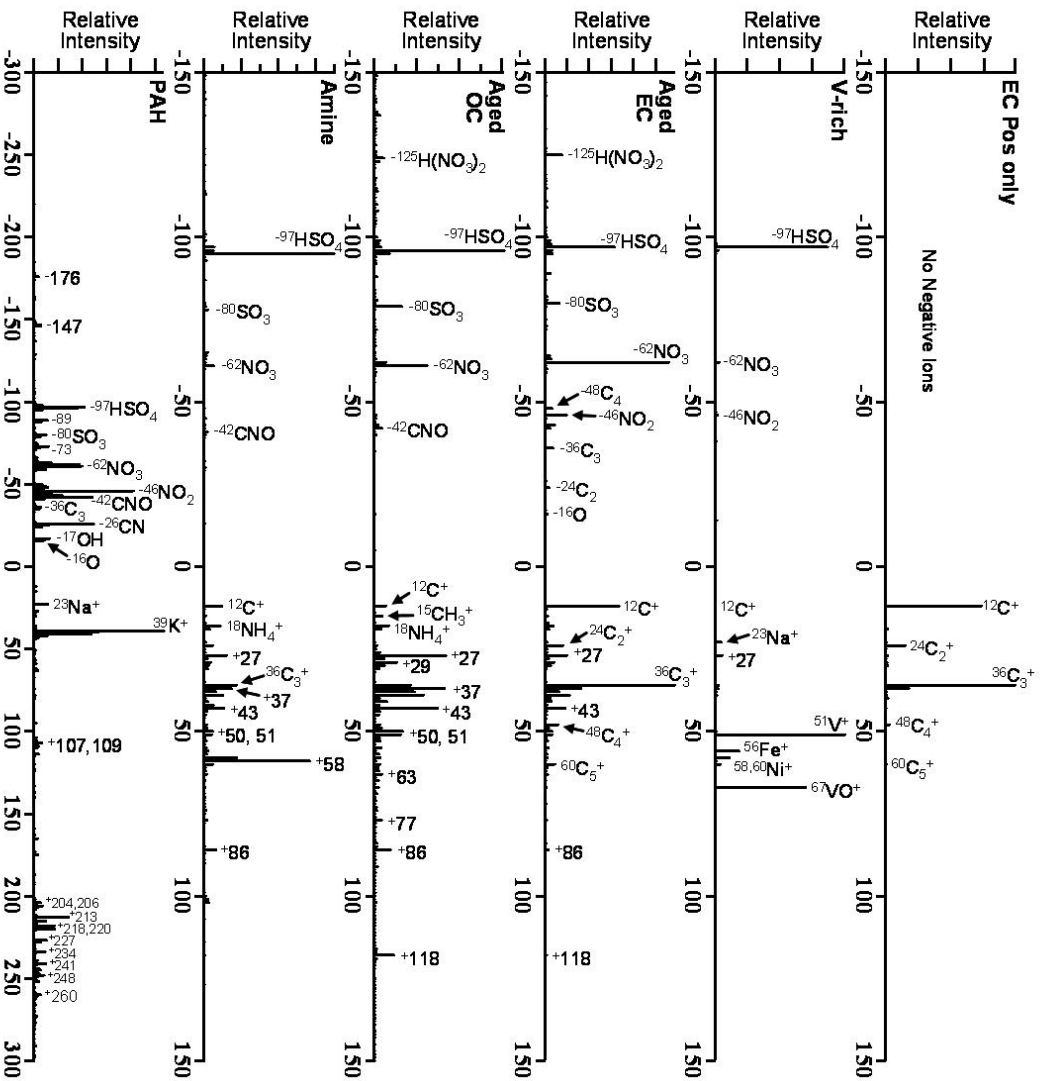
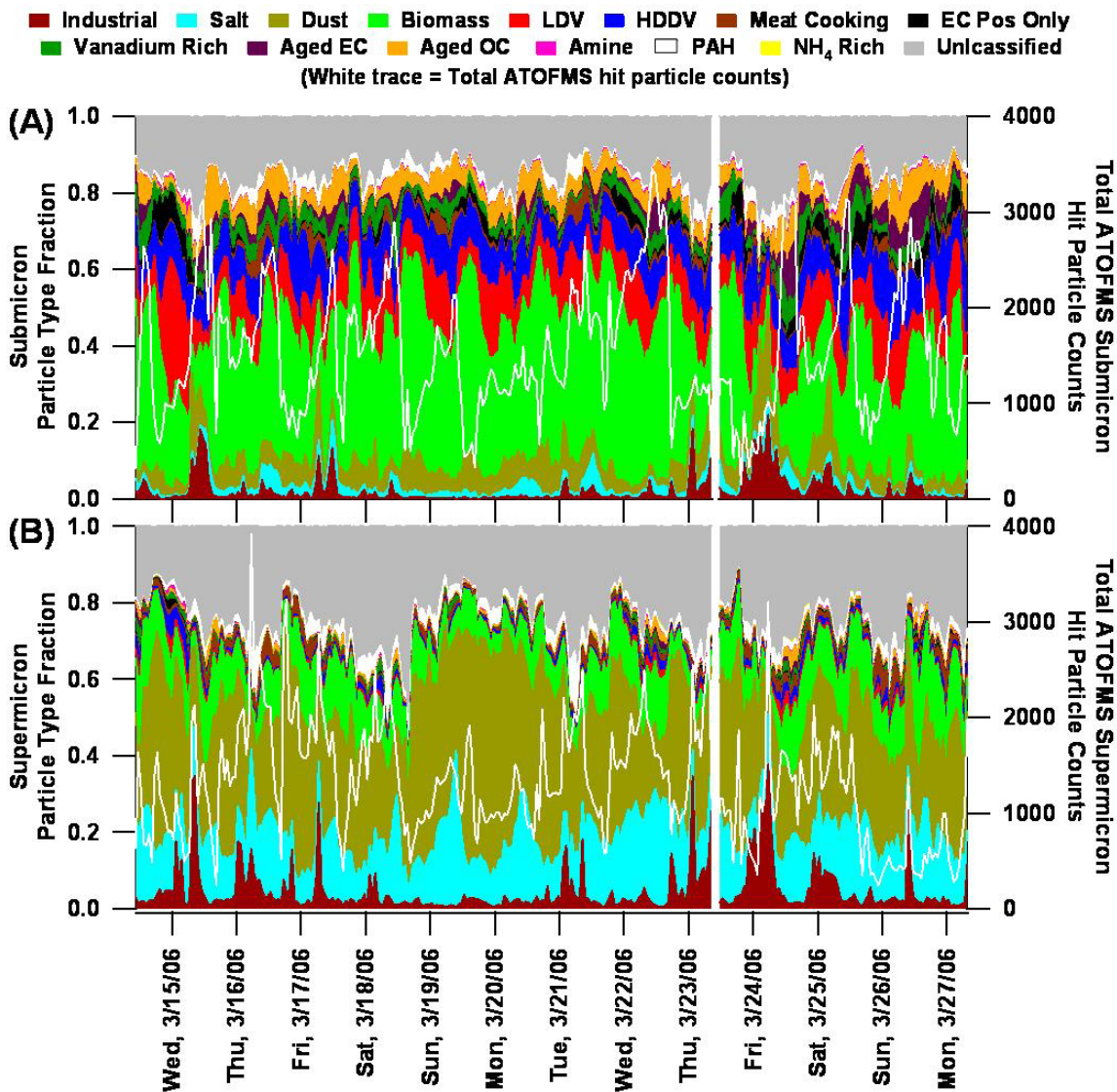


Figure 26: The top matching non-source specific mass spectral signatures for each type for Athens, Greece ATOFMS data.

Figure 25 shows the top non-source specific library clusters that were matched to for the Athens dataset. The EC pos only type (characterized by EC peaks at m/z 12, 24, 36, 48, and 60, and the lack of negative ions) and the vanadium (V-rich) particle types are very similar to the ones described in Chapter 5 (128). As noted earlier, these particles may be due to ship exhaust emissions as indicated in Chapter 5, but their low R^2 correlation for the Athens data may suggest different sources for this site. Further analysis is underway to confirm this, as these are relatively general particle types that could be produced from a number of different sources. The aged EC and aged OC types both show the presence of nitrate, ammonium, SOA (m/z $^{+43}$), and sulfate species, indicating secondary species are prevalent in Athens. The presence of m/z -125 [$\text{H}(\text{NO}_3)_2$], which is also on the biomass particles, is an indication of a large amount of nitrate species on these particles.

1619 As was done for the Athens data, the ambient particles detected with the ATOFMS used
 1620 by Moffet et al. in Mexico City were analyzed using the match-ART-2a technique with
 1621 the mass spectral source signature library. For this particular analysis, the submicron
 1622 (180 – 1000 nm) and supermicron (1000 – 3000 nm) particles were analyzed separately,
 1623 as done by Moffet et al. for direct comparison of the results. Figure 26A and 26B shows
 1624 the temporal series of the submicron and supermicron apportioned particles in the same
 1625 manner as in Moffet et al. For submicron particles apportioned with the source library
 1626 matching method in Figure 26A, it was found that the majority (34%) of the submicron
 1627 particles were attributed to biomass burning. It has been noted in the



1628
 1629 Figure 27: Temporal series of the mass spectral source library matching results for Mexico City
 1630 ambient A) submicron particles; and B) supermicron particles.
 1631

1632 literature that there were many visible brush and agricultural fires around Mexico City
1633 during this study (141,162). Vehicle emissions and dust make up the next largest
1634 fractions with 11% LDV, 10% HDDV, and 6% dust. Aged OC (5%), aged EC (3%),
1635 vanadium particles (4%), meat cooking (2%), and PAH containing particles (2%) also
1636 make notable contributions to the submicron matched particles. Upon further evaluation
1637 of the apportionment results, it was found that 44% of the particles apportioned to LDV
1638 are similar (with dot products above 0.85) to the aged OC seeds as well. As studies on
1639 Mexico City particulate matter have indicated that secondary organic species dominate
1640 the particle mass (163-168), this could be an indication that some of the aged OC
1641 particles have been incorrectly apportioned as LDV. However, it has been shown that
1642 LDVs produce a large number of OC particles above 100 nm (157). Therefore, a large
1643 amount of these particles can actually be from primary LDV emissions but have
1644 undergone aging and have become coated with secondary organic species. The biomass
1645 and vehicle particles show diurnal trends which agree with the findings in Moffet et al.,
1646 2007. The particles matched to the meat cooking library signatures generally peak during
1647 the morning and early afternoon hours, which is when local street vendors were observed
1648 to be cooking. Additionally, the particles that matched to the industrial seeds
1649 (representing 2% of the submicron matched particles) have episodal occurrences, which
1650 also agrees with the findings by Moffet et al. (141). Another 2% of the submicron
1651 particles, labeled as "Salt", were matched to sea salt clusters in the source library. Since
1652 Mexico City is a considerable distance (about 250 km) from the ocean, the presence of
1653 such particles could be from the dry lake bed of Lake Texcoco (located ~15 km east)
1654 which has regions of salt flats (141,169-172). Due to the fact that these particles are in
1655 the submicron mode, they could also be from combustion processes originating from
1656 industry or from paper refuse incineration. The submicron salt particles closely resemble
1657 the supermicron salt particles; however, about 55% of the submicron salt particles show
1658 the presence of elemental and organic carbon.

1659 As can be seen in Figure 26B for the supermicron mode, the majority of matched
1660 particles are from dust (34%), salt (15%), and biomass (11%) particles. The salt particles
1661 show a diurnal pattern, and spike during time periods when the winds are coming from
1662 the east and north-east (141). As mentioned for the submicron salt, with the Texcoco dry
1663 lake bed being located east/northeast of the sampling site, it makes it the likely candidate
1664 for the source of these salt particles. The particles matched to the industrial library seeds
1665 occur in early morning episodes, at the same times as in the submicron mode, and make
1666 up 5% of the particles in the supermicron mode. The matching percentages for each
1667 source are summarized in Figure 28.

1668 It is also apparent from Figure 26 that the amount of unclassified particles for the
1669 Mexico City ATOFMS data (submicron = 16% & supermicron = 25%) is much less than
1670 that for the Athens dataset. This is primarily because there are fewer miscalibrated
1671 spectra for the Mexico City dataset. As with the Athens dataset though, there is a larger
1672 fraction of miscalibrated spectra in for the supermicron particles (~10%) than in the
1673 submicron particles (~3%) in the Mexico City dataset. It is hypothesized that the
1674

Particle Source	Matching VF = 0.85		Matching VF = 0.85**		Matching VF = 0.75	
	Sub %	Super %	Sub %	Super %	Sub %	Super %
Industrial	2.19	4.56	2.42	4.82	3.23	5.53
Salt	1.99	15.19	2.52	18.16	2.38	17.04
Dust	6.26	34.01	7.63	39.32	7.76	40.20
Biomass	34.07	10.99	35.59	12.02	36.48	12.68
LDV	11.19	0.96	11.71	1.03	14.79	1.65
HDDV	9.84	1.43	9.81	1.42	10.55	2.41
Meat Cooking	1.77	2.17	1.77	2.16	1.74	2.15
EC (Positive only)	2.19	0.21	2.19	0.21	2.26	0.22
Vanadium Rich	4.03	0.69	4.40	0.95	5.00	0.95
Aged EC	2.78	0.30	2.77	0.30	2.84	0.35
Aged OC	5.32	1.00	5.32	1.00	6.25	2.29
Amine Containing	0.37	0.17	0.74	0.42	0.85	0.28
PAH Containing	2.17	3.06	1.57	2.73	1.35	2.43
NH4 Containing	0.00	0.03	0.00	0.03	0.00	0.10
Unclassified	15.83	25.23	11.56	15.44	4.51	11.72

Sub = Submicron particles (180-1000nm)

Super = Supermicron particles (1000-3000nm)

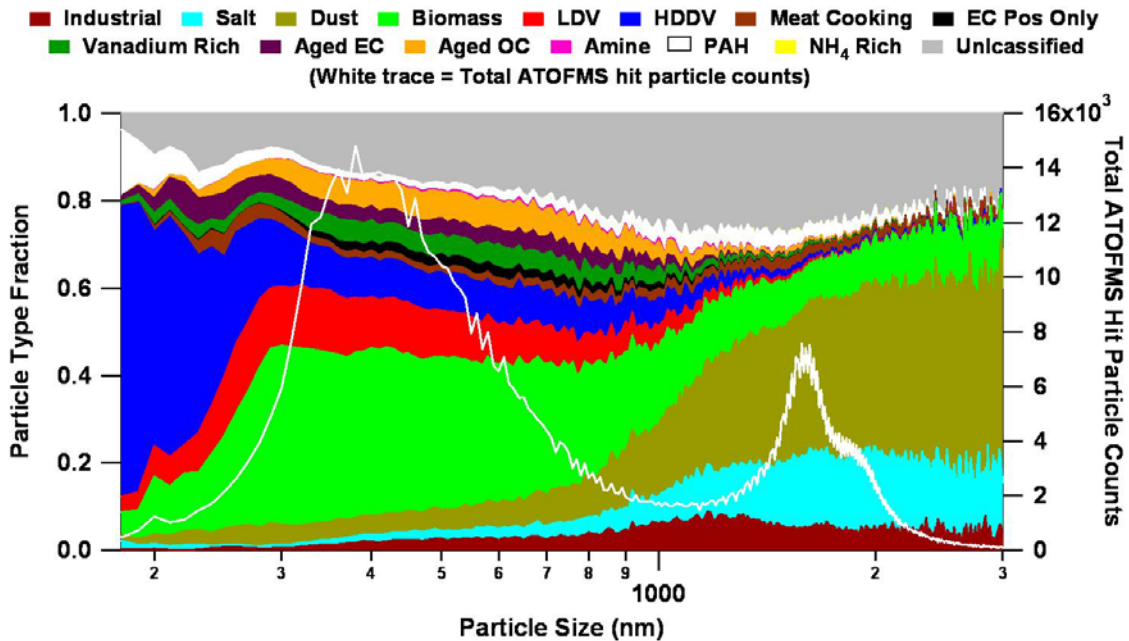
** Matching at VF = 0.85 including rematching unclassified particles using positive ion only matching

1675

1676

1677

Figure 28: Percent of Mexico City particles matched to the mass spectral source library at different match-ART-2a Vigilance Factors (VF).



1678

1679

1680

Figure 29: Size resolved source apportionment of the ATOFMS detected ambient particles for Mexico City.

1681 extremely large ion signals (which often exceed acquisition board scale) produced from
1682 inorganic particle species, such as dust and salt, detected in the supermicron mode may
1683 be the reason for these miscalibrated spectra. Further experiments are needed to confirm
1684 this hypothesis though. The unmatched particles that are not miscalibrated are either
1685 from sources not in the current mass spectral library, or are particle types that are far
1686 more aged than their equivalent types in the library.

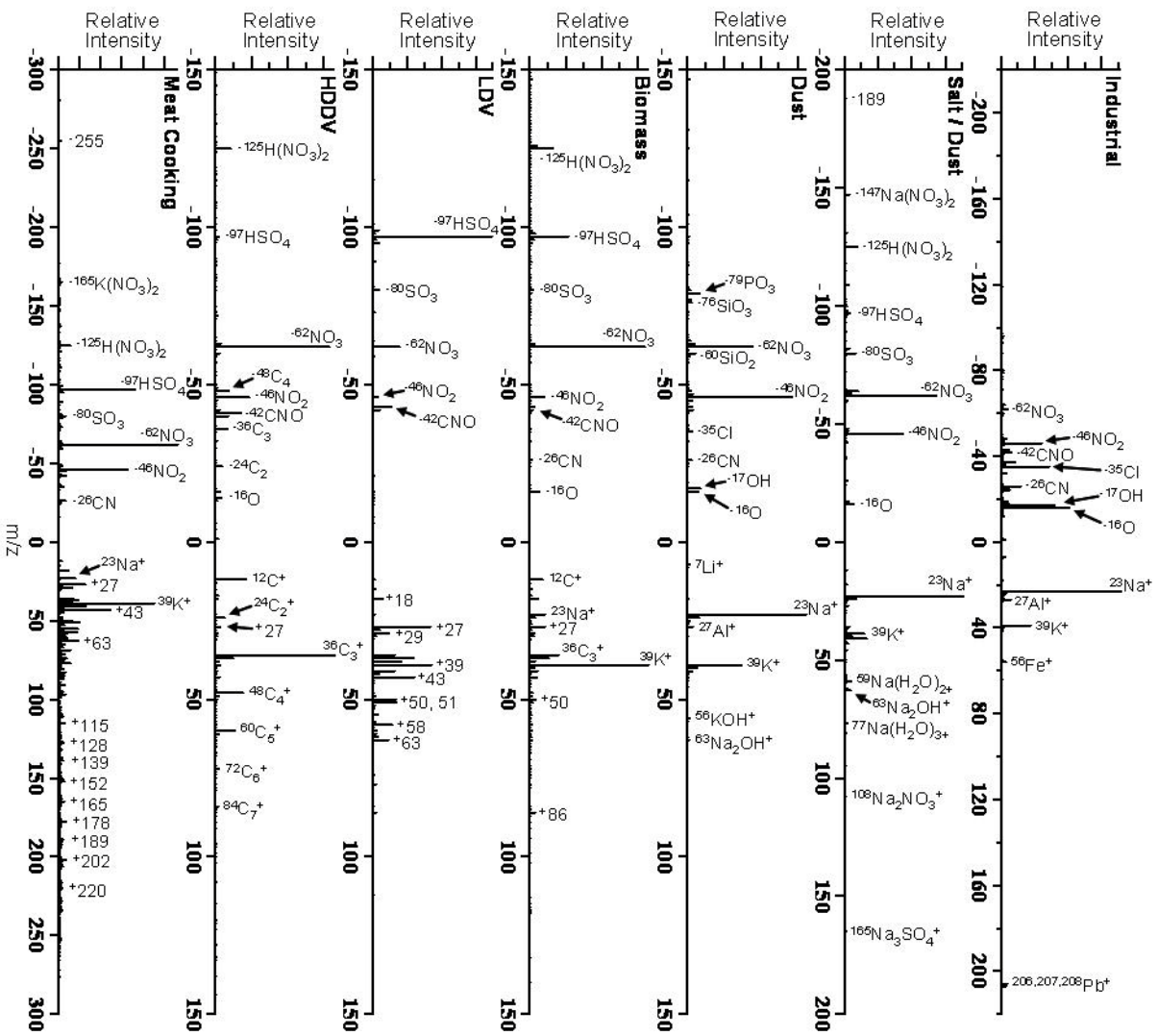
1687 Figure 27 shows the size resolved source apportionment of the ATOFMS detected
1688 ambient particles for Mexico City. Similar to what was seen for Athens, Greece; biomass
1689 particles represent the major fraction of the submicron particles down to 250 nm. As
1690 with Athens, the influence from both HDDV and LDV emissions can be seen throughout
1691 the submicron particles, and below 250 nm the influence from diesel emissions is
1692 detected as the major particle type. A major difference between the aerosol for the two
1693 locations is the near absence of the EC positive ion only type in Mexico City. There is a
1694 small amount detected (about 2%) in Mexico City, but, as will be shown below, the
1695 spectra for this type is different from the EC particles detected in Athens. Likewise, the
1696 top vanadium type detected in Mexico City is different than the one seen in Athens, and
1697 does not resemble the vanadium particles thought to be from ship emissions (128,143).
1698 When comparing Figure 27 to Figure 23, it can be seen that the presence of aged OC,
1699 aged EC, meat cooking, and PAH-containing particles are more prevalent at the Mexico
1700 City site than at the Athens, Greece site.

1701 d. Source Signature Matching for Mexico City

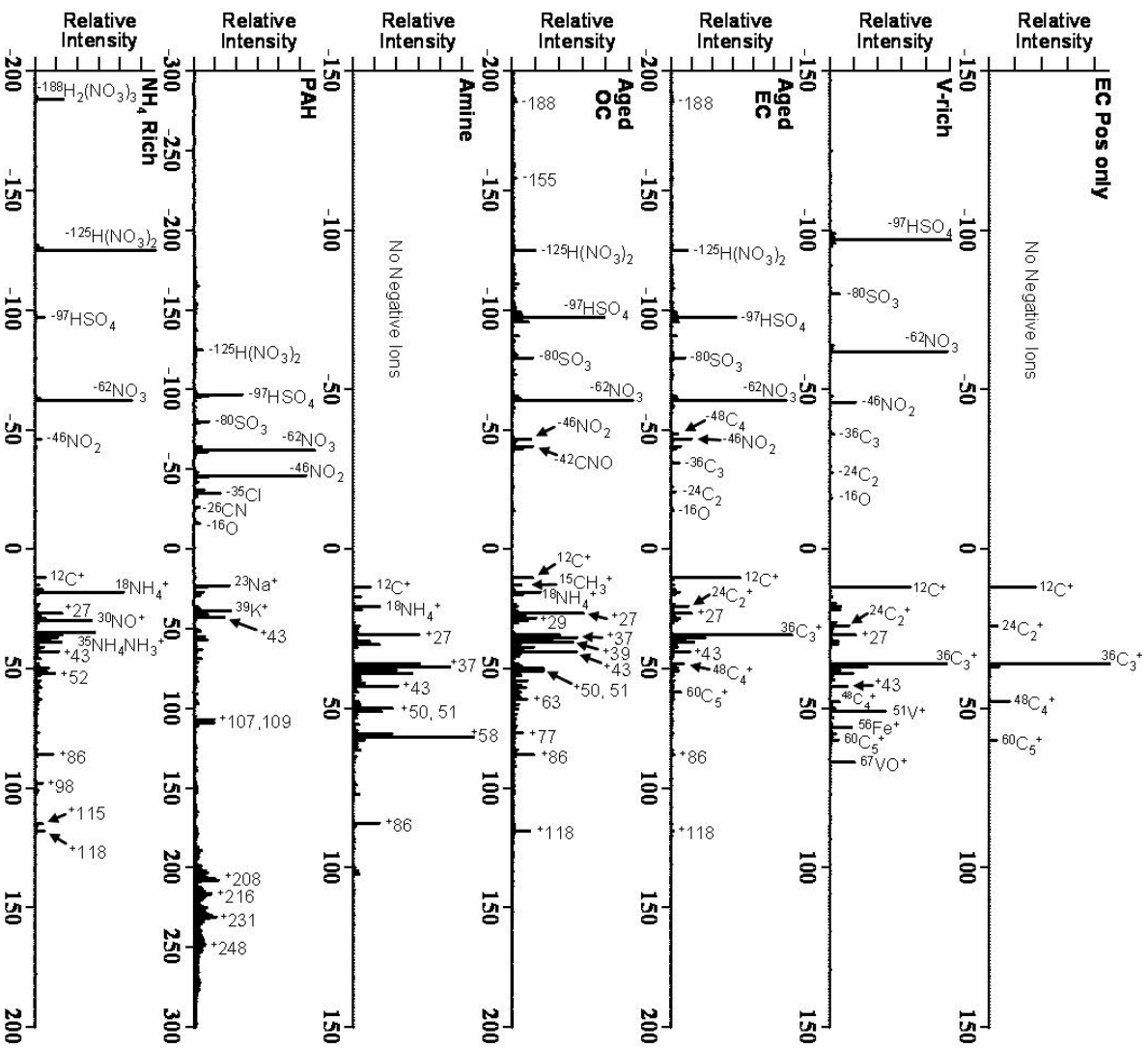
1702 The top source library spectra that the ambient Mexico City particles matched to
1703 for each specific source are shown in Figure 28, while Figure 30 shows the top non-
1704 source specific source spectra that were matched. Since the source signatures for
1705 industrial particles were generated from the Mexico City dataset, it is of no surprise that
1706 the top industrial type matched is the same as the top industrial type described by Moffet
1707 et al., 2007. As mentioned before, this industrial particle type is characterized by the
1708 large ion signals due to sodium and potassium, as well as the presence of aluminum, iron,
1709 and lead, and is consistent with particles associated with high temperature combustion
1710 sources such as waste incinerators (141,150).

1711 The top salt type, which matched to sea salt signatures, is also described by Moffet et al.
1712 as a Na-K class. As previously mentioned, these particles likely come from the Texcoco
1713 dry lake bed which has salt flat regions. This wind suspended salt (or dust) is very
1714 similar to aged sea salt in that it has ion peaks for sodium-water clusters, as well as
1715 sodium nitrate and sodium sulfate (as shown in Figure 28). The top dust type matched in
1716 Mexico City, while containing sodium and potassium, is different from the salt type. The
1717 dust contains ion markers for Al^+ , Li^+ , silicates and phosphate, and does not have sodium
1718 nitrate or sodium sulfate as in the salt type.

1719 The top biomass type matched in Mexico City is very similar to that matched for
1720 the Athens dataset except that the Mexico City biomass type is more aged, as it has larger
1721 ion peaks for NO_3^- (m/z -62) and $H(NO_3)_2^-$ (m/z -125). As described by Moffet et al., the
1722 majority of the secondary species found on the particles in Mexico City is from NO_x ,
1723 SOA and ammonium. The LDV top matched type is the same library signature that was



1724
1725
1726
Figure 30: The top matching mass spectral source signatures for each source for Mexico City ATOFMS data.



1727
 1728 Figure 31: The top matching non-source specific mass spectral signatures for each type for
 1729 Mexico City ATOFMS data.

1730 the top type for the Athens dataset, however the top HDDV matched type is very
 1731 different from the Athens type and shows aging ion peaks due to the uptake of NO_x
 1732 species. This is expected as Mexico City is more polluted than Athens, and has more
 1733 sources (vehicles and industry) that release gas phase NO_x (which is the precursor for
 1734 particle phase nitrate). This HDDV signature is one that was generated from slightly
 1735 aged particles detected at a freeway-side study (127). While the Mexico City sampling
 1736 site was located in an industrial area, it has been reported that there was considerable
 1737 traffic both from gasoline and diesel vehicles in the area around the sampling site (141).
 1738 The top meat cooking matched type detected in Mexico City exhibits the presence of
 1739 oleic acid (m/z -255), which is often used as a tracer for meat cooking emissions (173-

1740 174). As mentioned in Moffet et al., 2007, a busy roadway near the sampling site had
1741 street vendors who were often cooking meat during the morning through the afternoon.

1742 Figure 30 shows the top non-source specific library clusters that were matched to
1743 for the Mexico City dataset. As was mentioned in the discussion for the Athens data, the
1744 EC pos only and vanadium-containing particles matched in Mexico are different than
1745 those matched in Athens. These types are hypothesized to come from ship emissions in
1746 Athens, Greece, however, they are more likely from other sources in Mexico City since
1747 Mexico City is a considerable distance from the ocean. While EC is commonly emitted
1748 from a variety of combustion sources, vanadium is often used as a heavy oil marker
1749 which can also come from a variety of sources, including vehicle emissions (157,175),
1750 industrial emissions (176-177), and from oil fired power plants (178-179). The EC
1751 positive ion only type is different than the one detected in Athens in that the ion intensity
1752 for m/z ⁺³⁶ is much greater than that of m/z ⁺¹², and the ion peaks for m/z ⁺⁴⁸ & ⁺⁶⁰ are
1753 also more intense in Mexico City. These characteristics of the EC positive ion type are
1754 similar to those seen for diesel emissions and LDVs that emit large amounts of smoke
1755 from their tailpipe (105,127,157). While this could also be an artifact due to “hot spots”
1756 and shot-to-shot variability in the LDI laser used for the ATOFMS (124), that is likely
1757 not the case due. If the types between the two studies were due to the LDI process, there
1758 would be a more random generation of EC pos only types in both studies, and not the
1759 majorities seen for each. This is more of an indication of different particle sources (or
1760 atmospheric processes) with both locations having the majority of the EC pos only
1761 particles being different. Additionally, the vanadium type for Mexico City, shown in
1762 Figure 30, is very noticeably different than the type shown for Athens in that the
1763 vanadium in Mexico City has large peaks due to EC in the positive ions.

1764 The top matched vanadium, aged EC, aged OC, and PAH-containing signatures
1765 matched in Mexico City show larger peaks for NO_x species in the negative ions than for
1766 Athens. This is likely due to the vastly larger amount of gas-phase and particulate
1767 pollution that is in Mexico City than in Athens. The presence of the NH₄ rich particle
1768 type in Mexico City (shown in Figure 30) is also a strong indication of the amount of
1769 secondary species in the atmosphere there. While this type only accounted for 0.03%
1770 (29,381 of the 979,357 detected supermicron particles) of the matched particles in
1771 Mexico City, this type was not detected at all for the Athens dataset. This could be an
1772 indication that there is either less ammonium containing particles present in the
1773 atmosphere in Athens compared to Mexico City, or more of the ammonium is in the form
1774 of pure ammonium sulfate, or nitrate, in Athens which (in its pure form) is not ionized
1775 and detected by the mass spectrometer of the ATOFMS. This is typically a simple
1776 particle type to check for as it will appear in the ATOFMS data as a lot of scattered
1777 particles that do not produce a mass spectrum. This has been referred to as a “missing
1778 type” in previous ATOFMS studies (180). Unfortunately, the data for scattered particles
1779 without mass spectra (or, missed particles) is not available for the Athens dataset to check
1780 for this type.

1781 *e. Future implementations*

1782 A major goal of the source library matching approach is to be able to perform on-
1783 the-fly (or real-time) apportionment when running the ATOFMS instrument.
1784 Experimental modifications to the ATOFMS software have been made to include the

1785 particle source library along with a variation of the match-ART-2a algorithm in order to
1786 instantly compare the spectra of each particle to the source library as they are detected
1787 with the instrument. The results are then displayed in real time along with the other on-
1788 screen displays for the instrument. This kind of application of the source library can be
1789 particularly useful for mobile experiments or chase studies where the sampling specific
1790 sources are desired. Since the analysis would be taking place in real-time, the sampling
1791 location could be adjusted accordingly by the user to detect the desired source (or
1792 sources).

1793 The results shown in this paper indicate that the source library matching method
1794 is accurate when apportioning ATOFMS detected ambient particles. Additionally, the
1795 method is much faster in its analysis than the traditional hand classification of ART-2a
1796 results. It can take weeks to months to classify an ATOFMS dataset of a million particles
1797 using the traditional ART-2a clustering followed by hand grouping and classification,
1798 where the match-ART-2a technique with the source signature library can classify the
1799 majority of the particles in same dataset in about 6 hours (using a 3-GHz Pentium
1800 processor computer with 4-Gb of RAM). While the current source library only contains
1801 seeds for seven specific sources (LDV, HDDV, biomass burning, dust, sea salt, industrial
1802 emissions, and meat cooking), these are seven of the largest contributors to ambient
1803 PM_{2.5} in urban areas (112,131-139,176). As more ATOFMS source characterization
1804 studies are conducted, new source signatures can be added to the source library to
1805 increase its diversity and ability to distinguish individual sources of ambient aerosols. As
1806 particles become increasingly aged or agglomerated, identifying their original primary
1807 source becomes more difficult. In this case, the particles will be classified as secondary
1808 (or aged) particles since their signatures are now dominated by secondary species. As
1809 many recent studies have shown that SOA can make up 75 – 90 % of the submicron OC
1810 particles (166,181-185), it is important to be able to distinguish between primary and
1811 secondary particles. This is why the more general (non-source specific) seeds (EC pos
1812 only, aged OC, aged EC, amines, PAH's, vanadium containing, and NH₄ containing) are
1813 included in the library. Future ATOFMS studies where the particles from specific
1814 sources are put under controlled aging environments, such as in smog chamber or flow
1815 tube experiments, will help resolve the origin of these types of particles and help reduce
1816 the amount of unclassified particles when using the source library matching method. In
1817 addition, such experiments could yield the signatures for the aged version of the source
1818 particles and could allow for the determination of how much secondary species are on the
1819 primary particles.

1820 **iv. Acknowledgements**

1821 The authors thank Laura Shields, Sharon Qin, Thomas Rebotier, and Kerri
1822 Denkenberger for their help and input with testing the source signature library. Funding
1823 for the development of the source library was provided by the California Air Resources
1824 Board (CARB).

1825
1826

1828 **D. References**

1829

1830 (1) Gard, E.; Mayer, J. E.; Morrical, B. D.; Dienes, T.; Fergenson, D. P.;
1831 Prather, K. A., Real-time analysis of individual atmospheric aerosol particles - design and
1832 performance of a portable ATOFMS. *Analytical Chemistry* **1997**, *69*, (20) 4083-4091.

1833 (2) Su, Y. X.; Sipin, M. F.; Furutani, H.; Prather, K. A., Development and
1834 characterization of an aerosol time-of-flight mass spectrometer with increased detection
1835 efficiency. *Analytical Chemistry* **2004**, *76*, (3) 712-719.

1836 (3) Liu, P.; Ziemann, P. J.; Kittelson, D. B.; McMurry, P. H., Generating
1837 Particle Beams of Controlled Dimensions and Divergence .1. Theory of Particle Motion
1838 in Aerodynamic Lenses and Nozzle Expansions. *Aerosol Science and Technology* **1995**,
1839 *22*, (3) 293-313.

1840 (4) Liu, P.; Ziemann, P. J.; Kittelson, D. B.; McMurry, P. H., Generating
1841 Particle Beams of Controlled Dimensions and Divergence .2. Experimental Evaluation of
1842 Particle Motion in Aerodynamic Lenses and Nozzle Expansions. *Aerosol Science and*
1843 *Technology* **1995**, *22*, (3) 314-324.

1844 (5) Pratt, K. A.; Mayer, J. E.; Holecek, J. C.; Moffet, R. C.; Sanchez, R. O.;
1845 Rebotier, T. P.; Furutani, H.; Gonin, M.; Fuhrer, K.; Su, Y. X.; Guazzotti, S.; Prather, K.
1846 A., Development and Characterization of an Aircraft Aerosol Time-of-Flight Mass
1847 Spectrometer. *Anal. Chem.* **2009**, *81*, (5) 1792-1800.

1848 (6) Hinz, K. P.; Greweling, M.; Drews, F.; Spengler, B., Data processing in
1849 on-line laser mass spectrometry of inorganic, organic, or biological airborne particles.
1850 *Journal of the American Society for Mass Spectrometry* **1999**, *10*, (7) 648-660.

1851 (7) Phares, D. J.; Rhoads, K. P.; Wexler, A. S.; Kane, D. B.; Johnston, M. V.,
1852 Application of the ART-2a algorithm to laser ablation aerosol mass spectrometry of
1853 particle standards. *Analytical Chemistry* **2001**, *73*, (10) 2338-2344.

1854 (8) Murphy, D. M.; Middlebrook, A. M.; Warshawsky, M., Cluster analysis of
1855 data from the Particle Analysis by Laser Mass Spectrometry (PALMS) instrument.
1856 *Aerosol Science and Technology* **2003**, *37*, (4) 382-391.

1857 (9) Rebotier, T. P.; Prather, K. A., Aerosol time-of-flight mass spectrometry
1858 data analysis: A benchmark of clustering algorithms. *Analytica Chimica Acta* **2007**, *585*,
1859 (1) 38-54.

1860 (10) Hinz, K. P.; Spengler, B., Instrumentation, data evaluation and
1861 quantification in on-line aerosol mass spectrometry. *Journal of Mass Spectrometry* **2007**,
1862 *42*, (7) 843-860.

1863 (11) Xie, Y.; Hopke, P. K.; Wienke, D., Airborne particle classification with a
1864 combination of chemical composition and shape index utilizing an adaptive resonance
1865 artificial neural network. *Environmental Science & Technology* **1994**, *28*, (11) 1921-
1866 1928.

1867 (12) Hopke, P. K.; Song, X. H., Classification of single particles by neural
1868 networks based on the computer-controlled scanning electron microscopy data. *Analytica*
1869 *Chimica Acta* **1997**, *348*, (1-3) 375-388.

- 1870 (13) Song, C. H.; Carmichael, G. R., The aging process of naturally emitted
1871 aerosol (sea-salt and mineral aerosol) during long range transport. *Atmospheric*
1872 *Environment* **1999**, *33*, (14) 2203-2218.
- 1873 (14) Toner, S. M.; Shields, L. G.; Sodeman, D. A.; Prather, K. A., Using mass
1874 spectral source signatures to apportion exhaust particles from gasoline and diesel
1875 powered vehicles in a freeway study using UF-ATOFMS, in press. *Atmospheric*
1876 *Environment* **2007**.
- 1877 (15) Poschl, U., Atmospheric aerosols: Composition, transformation, climate
1878 and health effects. *Angewandte Chemie-International Edition* **2005**, *44*, (46) 7520-7540.
- 1879 (16) Kiehl, J. T.; Briegleb, B. P., The relative roles of sulfate aerosols and
1880 greenhouse gases in climate forcing. *Science* **1993**, *260*, (5106) 311-314.
- 1881 (17) Singh, M.; Jaques, P. A.; Sioutas, C., Size distribution and diurnal
1882 characteristics of particle-bound metals in source and receptor sites of the Los Angeles
1883 Basin. *Atmos. Environ.* **2002**, *36*, (10) 1675-1689.
- 1884 (18) Barnes, I.; Hjorth, J.; Mihalopoulos, N., Dimethyl sulfide and dimethyl
1885 sulfoxide and their oxidation in the atmosphere. *Chem. Rev.* **2006**, *106*, (3) 940-975.
- 1886 (19) Bates, T. S.; Lamb, B. K.; Guenther, A.; Dignon, J.; Stoiber, R. E., Sulfur
1887 emissions to the atmosphere from natural sources. *J. Atmos. Chem.* **1992**, *14*, (1-4) 315-
1888 337.
- 1889 (20) Charlson, R. J.; Lovelock, J. E.; Andreae, M. O.; Warren, S. G., Oceanic
1890 phytoplankton, atmospheric sulfur, cloud albedo and climate. *Nature* **1987**, *326*, (6114)
1891 655-661.
- 1892 (21) Hopkins, R. J.; Desyaterik, Y.; Tivanski, A. V.; Zaveri, R. A.; Berkowitz,
1893 C. M.; Tyliczszak, T.; Gilles, M. K.; Laskin, A., Chemical speciation of sulfur in marine
1894 cloud droplets and particles: Analysis of individual particles from the marine boundary
1895 layer over the California Current. *J. Geophys. Res.-Atmos.* **2008**, *113*, (D4) D04209,
1896 doi:04210.01029/02007JD008954.
- 1897 (22) von Glasow, R.; Crutzen, P. J., Model study of multiphase DMS oxidation
1898 with a focus on halogens. *Atmos. Chem. Phys.* **2004**, *4*, 589-608.
- 1899 (23) Kreidenweis, S. M.; Seinfeld, J. H., Nucleation of sulfuric acid-water and
1900 methanesulfonic acid-water solution particles: Implications for the atmospheric
1901 chemistry of organosulfur species. *Atmos. Environ.* **1988**, *22*, (2) 283-296.
- 1902 (24) Bardouki, H.; da Rosa, M. B.; Mihalopoulos, N.; Palm, W. U.; Zetzsch,
1903 C., Kinetics and mechanism of the oxidation of dimethylsulfoxide (DMSO) and
1904 methanesulfinate (MSI-) by OH radicals in aqueous medium. *Atmos. Environ.* **2002**, *36*,
1905 (29) 4627-4634.
- 1906 (25) Ganor, E.; Foner, H. A.; Bingemer, H. G.; Udisti, R.; Setter, I., Biogenic
1907 sulphate generation in the Mediterranean Sea and its contribution to the sulphate anomaly
1908 in the aerosol over Israel and the Eastern Mediterranean. *Atmos. Environ.* **2000**, *34*, (20)
1909 3453-3462.
- 1910 (26) Kouvarakis, G.; Mihalopoulos, N., Seasonal variation of dimethylsulfide
1911 in the gas phase and of methanesulfonate and non-sea-salt sulfate in the aerosols phase in
1912 the Eastern Mediterranean atmosphere. *Atmos. Environ.* **2002**, *36*, (6) 929-938.
- 1913 (27) Watts, S. F.; Brimblecombe, P.; Watson, A. J., Methanesulfonic acid,
1914 dimethyl sulfoxide and dimethyl sulfone in aerosols. *Atmos. Environ. A-[Gen. Topics]*
1915 **1990**, *24*, (2) 353-359.

1916 (28) Phinney, L.; Leaitch, W. R.; Lohmann, U.; Boudries, H.; Worsnop, D. R.;
1917 Jayne, J. T.; Toom-Sauntry, D.; Wadleigh, M.; Sharma, S.; Shantz, N., Characterization
1918 of the aerosol over the sub-arctic north east Pacific Ocean. *Deep-Sea Res. Pt. II* **2006**, *53*,
1919 (20-22) 2410-2433.

1920 (29) Zorn, S. R.; Drewnick, F.; Schott, M.; Hoffmann, T.; Borrmann, S.,
1921 Characterization of the South Atlantic marine boundary layer aerosol using an aerodyne
1922 aerosol mass spectrometer. *Atmos. Chem. Phys.* **2008**, *8*, (16) 4711-4728.

1923 (30) Kolaitis, L. N.; Bruynseels, F. J.; Grieken, R. E. V.; Andreae, M. O.,
1924 Determination of methanesulfonic acid and non-sea-salt sulfate in single marine aerosol
1925 particles. *Environ. Sci. Technol.* **1989**, *23*, 236-240.

1926 (31) Huffman, J. A.; Docherty, K. S.; Aiken, A. C.; Cubison, M. J.; Ulbrich, I.
1927 M.; DeCarlo, P. F.; Sueper, D.; Jayne, J. T.; Worsnop, D. R.; Ziemann, P. J.; Jimenez, J.
1928 L., Chemically-resolved aerosol volatility measurements from two
1929 megacity field studies. *Atmos. Chem. Phys.* **2009**, *9*, 7161-7182.

1930 (32) Qin, X.; Shields, L. G.; Toner, S. M.; Pratt, K. A.; Prather, K. A., Seasonal
1931 comparisons of the single particle mixing state in Riverside, CA during the SOAR 2005
1932 campaign. *Aerosol Sci. Technol.* **2009**, *In Preparation*.

1933 (33) Mayali, X.; Franks, P. J. S.; Azam, F., Cultivation and ecosystem role of a
1934 marine Roseobacter clade-affiliated cluster bacterium. *Appl. Environ. Microbiol.* **2008**,
1935 *74*, (9) 2595-2603.

1936 (34) Hatton, A. D.; Wilson, S. T., Particulate dimethylsulphoxide and
1937 dimethylsulphonioacetate in phytoplankton cultures and Scottish coastal waters.
1938 *Aquat. Sci.* **2007**, *69*, (3) 330-340.

1939 (35) Gard, E.; Mayer, J. E.; Morrical, B. D.; Dienes, T.; Fergenson, D. P.;
1940 Prather, K. A., Real-time analysis of individual atmospheric aerosol particles: Design and
1941 performance of a portable ATOFMS. *Analytical Chemistry* **1997**, *69*, (20) 4083-4091.

1942 (36) Allen, J. O., YAADA software toolkit to analyze single-particle mass
1943 spectral data: Reference manual version 1.1 *Arizona State University* **2002**,
1944 <http://www.yaada.org>.

1945 (37) Neubauer, K. R.; Sum, S. T.; Johnston, M. V.; Wexler, A. S., Sulfur
1946 speciation in individual aerosol particles. *J. Geophys. Res.-Atmos.* **1996**, *101*, (D13)
1947 18701-18707.

1948 (38) Silva, P. J.; Prather, K. A., Interpretation of mass spectra from organic
1949 compounds in aerosol time-of-flight mass spectrometry. *Anal. Chem.* **2000**, *72*, (15)
1950 3553-3562.

1951 (39) Guazzotti, S. A.; Coffee, K. R.; Prather, K. A., Continuous measurements
1952 of size-resolved particle chemistry during INDOEX-Intensive Field Phase 99. *J.*
1953 *Geophys. Res.-Atmos.* **2001**, *106*, (D22) 28607-28627.

1954 (40) Gard, E. E.; Kleeman, M. J.; Gross, D. S.; Hughes, L. S.; Allen, J. O.;
1955 Morrical, B. D.; Fergenson, D. P.; Dienes, T.; Galli, M. E.; Johnson, R. J.; Cass, G. R.;
1956 Prather, K. A., Direct observation of heterogeneous chemistry in the atmosphere. *Science*
1957 **1998**, *279*, (5354) 1184-1187.

1958 (41) Song, X. H.; Hopke, P. K.; Fergenson, D. P.; Prather, K. A., Classification
1959 of single particles analyzed by ATOFMS using an artificial neural network, ART-2a.
1960 *Anal. Chem.* **1999**, *71*, (4) 860-865.

1961 (42) Pastor, S. H.; Allen, J. O.; Hughes, L. S.; Bhave, P.; Cass, G. R.; Prather,
1962 K. A., Ambient single particle analysis in Riverside, California by aerosol time-of-flight
1963 mass spectrometry during the SCOS97-NARSTO. *Atmos. Environ.* **2003**, *37*, S239-
1964 S258.

1965 (43) Pratt, K. A.; Prather, K. A., Real-time, single-particle volatility, size, and
1966 chemical composition measurements of aged urban aerosols. *Environ. Sci. Technol.* **2009**,
1967 *43*, (21) 8276-8282.

1968 (44) Spencer, M. T.; Prather, K. A., Using ATOFMS to determine OC/EC mass
1969 fractions in particles. *Aerosol Sci. Technol.* **2006**, *40*, (8) 585-594.

1970 (45) Angelino, S.; Suess, D. T.; Prather, K. A., Formation of aerosol particles
1971 from reactions of secondary and tertiary alkylamines: Characterization by aerosol time-
1972 of-flight mass spectrometry. *Environ. Sci. Technol.* **2001**, *35*, (15) 3130-3138.

1973 (46) Silva, P. J.; Carlin, R. A.; Prather, K. A., Single particle analysis of
1974 suspended soil dust from Southern California. *Atmos. Environ.* **2000**, *34*, 1811-1820.

1975 (47) Spencer, M. T.; Shields, L. G.; Sodeman, D. A.; Toner, S. M.; Prather, K.
1976 A., Comparison of oil and fuel particle chemical signatures with particle emissions from
1977 heavy and light duty vehicles. *Atmos. Environ.* **2006**, *40*, (27) 5224-5235.

1978 (48) Silva, P. J.; Liu, D. Y.; Noble, C. A.; Prather, K. A., Size and chemical
1979 characterization of individual particles resulting from biomass burning of local Southern
1980 California species. *Environ. Sci. Technol.* **1999**, *33*, (18) 3068-3076.

1981 (49) Ault, A. P.; Gaston, C. J.; Wang, Y.; Dominguez, G.; Thiemens, M. H.;
1982 Prather, K. A., Characterization of the single particle mixing state of individual ship
1983 plume events measured at the port of Los Angeles. *Environ. Sci. Technol.* **2009**,
1984 *Submitted*.

1985 (50) Ault, A. P.; Moore, M. J.; Furutani, H.; Prather, K. A., Impact of
1986 emissions from the Los Angeles port region on San Diego air quality during regional
1987 transport events. *Environ. Sci. Technol.* **2009**, *43*, (10) 3500-3506.

1988 (51) Qin, X. Y.; Prather, K. A., Impact of biomass emissions on particle
1989 chemistry during the California Regional Particulate Air Quality Study. *Int. J. Mass*
1990 *Spectrom.* **2006**, *258*, (1-3) 142-150.

1991 (52) Draxler, R. R.; Rolph, G. D., HYSPLIT (HYbrid Single-Particle
1992 Lagrangian Integrated Trajectory) model access via NOAA ARL READY Website
1993 (<http://www.arl.noaa.gov/ready/hysplit4.html>). *NOAA Air Resources Laboratory* **2003**,
1994 Silver Spring, MD.

1995 (53) Kim, H.-J.; Miller, A. J.; McGowan, J.; Carter, M. L., Coastal
1996 phytoplankton blooms in the Southern California Bight. *Prog. Oceanogr.* **2009**, *82*, 137-
1997 147.

1998 (54) Hughes, L. S.; Allen, J. O.; Bhave, P.; Kleeman, M. J.; Cass, G. R.; Liu,
1999 D. Y.; Fergenson, D. F.; Morrical, B. D.; Prather, K. A., Evolution of atmospheric
2000 particles along trajectories crossing the Los Angeles basin. *Environ. Sci. Technol.* **2000**,
2001 *34*, (15) 3058-3068.

2002 (55) Allen, J. O.; Fergenson, D. P.; Gard, E. E.; Hughes, L. S.; Morrical, B. D.;
2003 Kleeman, M. J.; Gross, D. S.; Galli, M. E.; Prather, K. A.; Cass, G. R., Particle detection
2004 efficiencies of aerosol time of flight mass spectrometers under ambient sampling
2005 conditions. *Environ. Sci. Technol.* **2000**, *34*, (1) 211-217.

2006 (56) Qin, X. Y.; Bhave, P. V.; Prather, K. A., Comparison of two methods for
2007 obtaining quantitative mass concentrations from aerosol time-of-flight mass spectrometry
2008 measurements. *Anal. Chem.* **2006**, *78*, (17) 6169-6178.

2009 (57) Seinfeld, J. H.; Pandis, S. N. *Atmospheric Chemistry and Physics*; John
2010 Wiley & Sons, Inc.: Hoboken, New Jersey, **2006**.

2011 (58) Isakson, J.; Persson, T. A.; Lindgren, E. S., Identification and assessment
2012 of ship emissions and their effects in the harbour of G(o)over-circleteborg, Sweden.
2013 *Atmos. Environ.* **2001**, *35*, (21) 3659-3666.

2014 (59) Whiteaker, J. R.; Prather, K. A., Hydroxymethanesulfonate as a tracer for
2015 fog processing of individual aerosol particles. *Atmos. Environ.* **2003**, *37*, (8) 1033-1043.

2016 (60) Dunn, J. P.; Stenger, H. G.; Wachs, I. E., Oxidation of sulfur dioxide over
2017 supported vanadia catalysts: Molecular structure-reactivity relationships and reaction
2018 kinetics. *Catal Today* **1999**, *51*, (2) 301-318.

2019 (61) Sahle-Demessie, E.; Devulapelli, V. G., Vapor phase oxidation of
2020 dimethyl sulfide with ozone over V₂O₅/TiO₂ catalyst. *Appl. Catal. B-Environ.* **2008**, *84*,
2021 (3-4) 408-419.

2022 (62) Bhave, P. V.; Allen, J. O.; Morrical, B. D.; Ferguson, D. P.; Cass, G. R.;
2023 Prather, K. A., A field-based approach for determining ATOFMS instrument sensitivities
2024 to ammonium and nitrate. *Environ. Sci. Technol.* **2002**, *36*, (22) 4868-4879.

2025 (63) Gross, D. S.; Galli, M. E.; Silva, P. J.; Prather, K. A., Relative sensitivity
2026 factors for alkali metal and ammonium cations in single particle aerosol time-of-flight
2027 mass spectra. *Anal. Chem.* **2000**, *72*, (2) 416-422.

2028 (64) *Petroleum products--Fuels (Class F) Specifications of Marine Fuels*; 3rd
2029 ed. Geneva, 2005.

2030 (65) Alexander, B.; Park, R. J.; Jacob, D. J.; Gong, S., Transition metal-
2031 catalyzed oxidation of atmospheric sulfur: Global implications for the sulfur budget. *J.*
2032 *Geophys. Res.* **2009**, *114*, (D02309) doi:10.1029/2008JD010486.

2033 (66) Lide, D. R., Ed. *CRC Handbook of Chemistry and Physics*; 89th ed.; CRC
2034 Press/Taylor and Francis: Boca Raton, FL, **2009**.

2035 (67) Carson, P. G.; Neubauer, K. R.; Johnston, M. V.; Wexler, A. S., On-line
2036 chemical analysis of aerosols by rapid single-particle mass spectrometry. *J. Aerosol Sci.*
2037 **1995**, *4*, (26) 535-545.

2038 (68) Key, J. M.; Paulk, N.; Johansen, A. M., Photochemistry of iron in
2039 simulated crustal aerosols with dimethyl sulfide oxidation products. *Environ. Sci.*
2040 *Technol.* **2008**, *42*, (1) 133-139.

2041 (69) Schlesinger, R. B.; Kunzli, N.; Hidy, G. M.; Gotschi, T.; Jerrett, M., The
2042 health relevance of ambient particulate matter characteristics: Coherence of toxicological
2043 and epidemiological inferences. *Inhalation Toxicol.* **2006**, *18*, (2) 95-125.

2044 (70) Burtscher, H.; Baltensperger, U.; Bukowiecki, N.; Cohn, P.; Hüglin, C.;
2045 Mohr, M.; Matter, U.; Nyeki, S.; Schmatloch, V.; Streit, N.; Weingartner, E., Separation
2046 of volatile and non-volatile aerosol fractions by thermodesorption: instrumental
2047 development and applications. *J. Aerosol Sci.* **2001**, *32*, 427-442.

2048 (71) Engler, C.; Rose, D.; Wehner, B.; Wiedensohler, A.; Brüggemann, E.;
2049 Gnauk, T.; Spindler, G.; Tuch, T.; Birmili, W., Size distributions of non-volatile particle
2050 residuals (D_p<800 nm) at a rural site in Germany and relation to air mass origin. *Atmos.*
2051 *Chem. Phys.* **2007**, *7*, (22) 5785.

2052 (72) Johnson, G.; Ristovski, Z.; Morawska, L., Application of the VH-TDMA
2053 technique to coastal ambient aerosols. *Geophys. Res. Lett.* **2004**, *31*, (16).

2054 (73) Frey, A.; Rose, D.; Wehner, B.; Muller, T.; Cheng, Y.; Wiedensohler, A.;
2055 Virkkula, A., Application of the volatility-TDMA technique to determine the number size
2056 distribution and mass concentration of less volatile particles. *Aerosol Sci. Technol.* **2008**,
2057 *42*, 817-828.

2058 (74) Kondo, Y.; Komazaki, Y.; Miyazaki, Y.; Moteki, N.; Takegawa, N.;
2059 Kodama, D.; Deguchi, S.; Nogami, M.; Fukuda, M.; Miyakawa, T.; Morino, Y.; Koike,
2060 M.; Sakurai, H.; Ehara, K., Temporal variations of elemental carbon in Tokyo. *J.*
2061 *Geophys. Res.* **2006**, *111*, (D12).

2062 (75) Huffman, J. A.; Ziemann, P. J.; Jayne, J. T.; Worsnop, D. R.; Jimenez, J.
2063 L., Development and characterization of a fast-stepping/scanning thermodenuder for
2064 chemically-resolved aerosol volatility measurements. *Aerosol Sci. Technol.* **2008**, *42*, (5)
2065 395-407.

2066 (76) Qin, X.; Shields, L. G.; Toner, S. M.; Pratt, K. A.; Prather, K. A., Seasonal
2067 comparisons of the single particle mixing state in Riverside, CA during the SOAR 2005
2068 campaign. *Aerosol Sci. Technol.* **2009**, *In preparation*.

2069 (77) Hughes, L. S.; Allen, J. O.; Salmon, L. G.; Mayo, P. R.; Johnson, R. J.;
2070 Cass, G. R., Evolution of nitrogen species air pollutants along trajectories crossing the
2071 Los Angeles area. *Environ. Sci. Technol.* **2002**, *36*, (18) 3928-3935.

2072 (78) Song, X. H.; Hopke, P. K.; Fergenson, D. P.; Prather, K. A., Classification
2073 of single particles analyzed by ATOFMS using an artificial neural network, ART-2A.
2074 *Anal. Chem.* **1999**, *71*, (4) 860-865.

2075 (79) Toner, S. M.; Shields, L. G.; Sodeman, D. A.; Prather, K. A., Using mass
2076 spectral source signatures to apportion exhaust particles from gasoline and diesel
2077 powered vehicles in a freeway study using UF-ATOFMS. *Atmos. Environ.* **2008**, *42*,
2078 568-581.

2079 (80) Ault, A. P.; Gaston, C. J.; Wang, Y.; Dominguez, G.; Thiemens, M. H.;
2080 Prather, K. A., Single particle mixing state of individual ship plumes at the Port of Los
2081 Angeles. *Environ. Sci. Technol.* **2009**, *Submitted*.

2082 (81) Silva, P. J.; Carlin, R. A.; Prather, K. A., Single particle analysis of
2083 suspended soil dust from Southern California. *Atmos. Environ.* **2000**, *34*, (11) 1811-1820.

2084 (82) Reinard, M. S.; Adou, K.; Martini, J. M.; Johnston, M. V., Source
2085 characterization and identification by real-time single particle mass spectrometry. *Atmos.*
2086 *Environ.* **2007**, *41*, 9397-9409.

2087 (83) DeCarlo, P. F.; Slowik, J. G.; Worsnop, D. R.; Davidovits, P.; Jimenez, J.
2088 L., Particle morphology and density characterization by combined mobility and
2089 aerodynamic diameter measurements. Part 1: Theory. *Aerosol Sci. Technol.* **2004**, *38*,
2090 (12) 1185-1205.

2091 (84) Moffet, R. C.; Qin, X.; Rebotier, T.; Furutani, H.; Prather, K. A.,
2092 Chemically segregated optical and microphysical properties of ambient aerosols
2093 measured in a single-particle mass spectrometer. *J. Geophys. Res.* **2008**, *113*,
2094 doi:10.1029/2007JD009393.

2095 (85) Na, K. S.; Sawant, A. A.; Song, C.; Cocker, D. R., Primary and secondary
2096 carbonaceous species in the atmosphere of Western Riverside County, California. *Atmos.*
2097 *Environ.* **2004**, *38*, (9) 1345-1355.

2098 (86) Sodeman, D. A.; Toner, S. M.; Prather, K. A., Determination of single
2099 particle mass spectral signatures from light-duty vehicle emissions. *Environ. Sci.*
2100 *Technol.* **2005**, *39*, (12) 4569-4580.

2101 (87) Shields, L. G.; Suess, D. T.; Prather, K. A., Determination of single
2102 particle mass spectral signatures from heavy-duty diesel vehicle emissions for PM_{2.5}
2103 source apportionment. *Atmos. Environ.* **2007**, *41*, (18) 3841-3852.

2104 (88) Guazzotti, S. A.; Suess, D. T.; Coffee, K. R.; Quinn, P. K.; Bates, T. S.;
2105 Wisthaler, A.; Hansel, A.; Ball, W. P.; Dickerson, R. R.; Neususs, C.; Crutzen, P. J.;
2106 Prather, K. A., Characterization of carbonaceous aerosols outflow from India and Arabia:
2107 Biomass/biofuel burning and fossil fuel combustion. *J. Geophys. Res.* **2003**, *108*, (D15).

2108 (89) Bezabeh, D. Z.; Allen, T. M.; McCauley, E. M.; Kelly, P. B.; Jones, A. D.,
2109 Negative ion laser desorption ionization time-of-flight mass spectrometry of nitrated
2110 polycyclic aromatic hydrocarbons. *J. Am. Soc. Mass Spectrom.* **1997**, *8*, (6) 630-636.

2111 (90) Hughes, L. S.; Allen, J. O.; Kleeman, M. J.; Johnson, R. J.; Cass, G. R.;
2112 Gross, D. S.; Gard, E. E.; Galli, M. E.; Morrical, B. D.; Ferguson, D. P.; Dienes, T.;
2113 Noble, C. A.; Silva, P. J.; Prather, K. A., Size and composition distribution of
2114 atmospheric particles in southern California. *Environ. Sci. Technol.* **1999**, *33*, (20) 3506-
2115 3515.

2116 (91) Russell, A. G.; Cass, G. R., Verification Of A Mathematical-Model For
2117 Aerosol Nitrate And Nitric-Acid Formation And Its Use For Control Measure Evaluation.
2118 *Atmos. Environ.* **1986**, *20*, (10) 2011-2025.

2119 (92) Bassett, M. E.; Seinfeld, J. H., Atmospheric Equilibrium-Model Of Sulfate
2120 And Nitrate Aerosols .2. Particle-Size Analysis. *Atmos. Environ.* **1984**, *18*, (6) 1163-
2121 1170.

2122 (93) Pastor, S. H.; Allen, J. O.; Hughes, L. S.; Bhave, P.; Cass, G. R.; Prather,
2123 K. A., Ambient single particle analysis in Riverside, California by aerosol time-of-flight
2124 mass spectrometry during the SCOS97-NARSTO. *Atmos. Environ.* **2003**, *37*,, S239-
2125 S258.

2126 (94) Johnson, G. R.; Ristovski, Z.; Morawska, L., Method for measuring the
2127 hygroscopic behaviour of lower volatility fractions in an internally mixed aerosol. *J.*
2128 *Aerosol Sci.* **2004**, *35*, (4) 443-455.

2129 (95) Huffman, J. A.; Docherty, K. S.; Aiken, A. C.; Cubison, M. J.; Ulbrich, I.
2130 M.; DeCarlo, P. F.; Sueper, D.; Jayne, J. T.; Worsnop, D. R.; Ziemann, P. J.; Jimenez, J.
2131 L., Chemically-resolved aerosol volatility measurements from two megacity field results.
2132 *Atmos. Chem. Phys. Discuss.* **2009**, *9*, 2645-2697.

2133 (96) Vlaev, L. T.; Georgieva, V. G.; Genieva, S. D., Products and kinetics of
2134 non-isothermal decomposition of vanadium(IV) oxide compounds. *J. Thermal. Anal. Cal.*
2135 **2007**, *88*, (3) 805-812.

2136 (97) Knudsen, J. N.; Jensen, P. A.; Dam-Johansen, K., Transformation and
2137 release to the gas phase of Cl, K, and S during combustion of annual biomass. *Energy*
2138 *Fuels* **2004**, *18*, (5) 1385-1399.

2139 (98) Clarke, A. D.; Shinozuka, Y.; Kapustin, V. N.; Howell, S.; Huebert, B.;
2140 Doherty, S.; Anderson, T.; Covert, D.; Anderson, J.; Hua, X.; Moore, K. G.;
2141 McNaughton, C.; Carmichael, G.; Weber, R., Size distributions and mixtures of dust and
2142 black carbon aerosol in Asian outflow: Physiochemistry and optical properties. *J.*
2143 *Geophys. Res.* **2004**, *109*, (D15).

2144 (99) Wehner, B.; Philippin, S.; Wiedensohler, A.; Scheer, V.; Vogt, R.,
2145 Variability of non-volatile fractions of atmospheric aerosol particles with traffic
2146 influence. *Atmos. Environ.* **2004**, *38*, (36) 6081-6090.

2147 (100) Clarke, A.; McNaughton, C.; Kapustin, V.; Shinozuka, Y.; Howell, S.;
2148 Dibb, J.; Zhou, J.; Anderson, B.; Brekhovskikh, V.; Turner, H.; Pinkerton, M., Biomass
2149 burning and pollution aerosol over North America: Organic components and their
2150 influence on spectral optical properties and humidification response. *J. Geophys. Res.*
2151 **2007**, *112*, (D12).

2152 (101) Reid, J. S.; Koppmann, R.; Eck, T. F.; Eleuterio, D. P., A review of
2153 biomass burning emissions part II: intensive physical properties of biomass burning
2154 particles. *Atmos. Chem. Phys.* **2005**, *5*, 799-825.

2155 (102) Shields, L. G.; Qin, X.; Toner, S. M.; Prather, K. A., Characterization of
2156 trace metals in single urban particles during the SOAR 2005 campaign. *Sci. Total*
2157 *Environ.* **2008**, *Submitted*.

2158 (103) Kleeman, M. J.; Hughes, L. S.; Allen, J. O.; Cass, G. R., Source
2159 contributions to the size and composition distribution of atmospheric particles: Southern
2160 California in September 1996. *Environ. Sci. Technol.* **1999**, *33*, (23) 4331-4341.

2161 (104) Munger, J. W.; Collett, J.; Daube, B.; Hoffmann, M. R., Fogwater
2162 chemistry at Riverside, California. *Atmos. Environ.* **1990**, *24B*, (2) 185-205.

2163 (105) Toner, S. M.; Sodeman, D. A.; Prather, K. A., Single particle
2164 characterization of ultrafine and accumulation mode particles from heavy duty diesel
2165 vehicles using aerosol time-of-flight mass spectrometry. *Environ. Sci. Technol.* **2006**, *40*,
2166 (12) 3912-3921.

2167 (106) Spencer, M. T.; Shields, L. G.; Sodeman, D. A.; Toner, S. M.; Prather, K.
2168 A., Comparison of oil and fuel particle chemical signatures with particle emissions from
2169 heavy and light duty vehicles. *Atmos. Environ.* **2006**, *40*, (27) 5224-5235.

2170 (107) Ramanathan, V.; Crutzen, P. J., New directions: Atmospheric brown
2171 "Clouds". *Atmospheric Environment* **2003**, *37*, (28) 4033-4035.

2172 (108) Griffin, R. J.; Dabdub, D.; Kleeman, M. J.; Fraser, M. P.; Cass, G. R.;
2173 Seinfeld, J. H., Secondary organic aerosol 3. Urban/regional scale model of size- and
2174 composition-resolved aerosols. *Journal of Geophysical Research, [Atmospheres]* **2002**,
2175 *107*, (D17) AAC5/1-AAC5/14.

2176 (109) Fraser, M. P.; Kleeman, M. J.; Schauer, J. J.; Cass, G. R., Modeling the
2177 atmospheric concentrations of individual gas-phase and particle-phase organic
2178 compounds. *Environmental Science and Technology* **2000**, *34*, (7) 1302-1312.

2179 (110) Chung, C. E.; Ramanathan, V.; Kim, D.; Podgorny, I. A., Global
2180 anthropogenic aerosol direct forcing derived from satellite and ground-based
2181 observations. *Journal of Geophysical Research-Atmospheres* **2005**, *110*, (D24).

2182 (111) Ramana, M. V.; Ramanathan, V., Abrupt transition from natural to
2183 anthropogenic aerosol radiative forcing: Observations at the ABC-Maldives Climate
2184 Observatory. *Journal of Geophysical Research-Atmospheres* **2006**, *111*, (D20).

2185 (112) Kleeman, M. J.; Cass, G. R., Source contributions to the size and
2186 composition distribution of urban particulate air pollution. *Atmospheric Environment*
2187 **1998**, *32*, (16) 2803-2816.

2188 (113) Kleeman, M. J.; Schauer, J. J.; Cass, G. R., Size and composition
2189 distribution of fine particulate matter emitted from motor vehicles. *Environmental*
2190 *Science and Technology* **2000**, *34*, (7) 1132-1142.

2191 (114) Cass, G. R.; Hughes, L. A.; Bhave, P.; Kleeman, M. J.; Allen, J. O.;
2192 Salmon, L. G., The chemical composition of atmospheric ultrafine particles.
2193 *Philosophical Transactions of the Royal Society of London, Series A: Mathematical,*
2194 *Physical and Engineering Sciences* **2000**, *358*, (1775) 2581-2592.

2195 (115) Reilly, P. T. A.; Gieray, R. A.; Whitten, W. B.; Ramsey, J. M., Real-time
2196 characterization of the organic composition and size of individual diesel engine smoke
2197 particles. *Environmental Science and Technology* **1998**, *32*, (18) 2672-2679.

2198 (116) Lehmann, U.; Mohr, M.; Schweizer, T.; Rutter, J., Number size
2199 distribution of particulate emissions of heavy-duty engines in real world test cycles.
2200 *Atmospheric Environment* **2003**, *37*, (37) 5247-5259.

2201 (117) Zhang, K. M.; Wexler, A. S.; Niemeier, D. A.; Zhu, Y. F.; Hinds, W. C.;
2202 Sioutas, C., Evolution of particle number distribution near roadways. Part III: Traffic
2203 analysis and on-road size resolved particulate emission factors. *Atmospheric Environment*
2204 **2005**, *39*, (22) 4155-4166.

2205 (118) Su, Y.; Sipin, M. F.; Furutani, H.; Prather, K. A., Development and
2206 characterization of an aerosol time-of-flight mass spectrometer with increased detection
2207 efficiency. *Analytical Chemistry* **2004**, *76*, (3) 712-719.

2208 (119) Bhave, P. V.; Ferguson, D. P.; Prather, K. A.; Cass, G. R., Source
2209 apportionment of fine particulate matter by clustering single-particle data: tests of
2210 receptor model accuracy. *Environmental Science and Technology* **2001**, *35*, (10) 2060-
2211 2072.

2212 (120) Bein, K. J.; Zhao, Y.; Pekney, N. J.; Davidson, C. I.; Johnston, M. V.;
2213 Wexler, A. S., Identification of sources of atmospheric PM at the Pittsburgh Supersite-
2214 Part II: Quantitative comparisons of single particle, particle number, and particle mass
2215 measurements. *Atmospheric Environment* **2006**, *40*, (Suppl. 2) S424-S444.

2216 (121) Owega, S.; Evans, G. J.; Jervis, R. E.; Fila, M.; D'Souza, R.; Khan, B.-U.-
2217 Z., Long-range sources of Toronto particulate matter (PM_{2.5}) identified by Aerosol Laser
2218 Ablation Mass Spectrometry (LAMMS). *Atmospheric Environment* **2004**, *38*, (33) 5545-
2219 5553.

2220 (122) Ward, J. H., Hierarchical grouping to optimize an objective function.
2221 *Journal of the American Statistical Association* **1963**, *58*, (301) 236.

2222 (123) Lance, G. N.; Williams, W. T., A General Theory of Classificatory Sorting
2223 Strategies .1. Hierarchical Systems. *Computer Journal* **1967**, *9*, (4) 373.

2224 (124) Wenzel, R. J.; Prather, K. A., Improvements in ion signal reproducibility
2225 obtained using a homogeneous laser beam for on-line laser desorption/ionization of
2226 single particles. *Rapid Communications in Mass Spectrometry* **2004**, *18*, (13) 1525-1533.

2227 (125) Song, X. H.; Faber, N. M.; Hopke, P. K.; Suess, D. T.; Prather, K. A.;
2228 Schauer, J. J.; Cass, G. R., Source apportionment of gasoline and diesel by multivariate
2229 calibration based on single particle mass spectral data. *Analytica Chimica Acta* **2001**,
2230 *446*, (1-2) 329-343.

2231 (126) Tan, P. V.; Malpica, O.; Evans, G. J.; Owega, S.; Fila, M. S., Chemically-
2232 assigned classification of aerosol mass spectra. *Journal of the American Society for Mass*
2233 *Spectrometry* **2002**, *13*, (7) 826-838.

2234 (127) Toner, S. M.; Shields, L. G.; Sodeman, D. A.; Prather, K. A., Using mass
2235 spectral source signatures to apportion exhaust particles from gasoline and diesel
2236 powered vehicles in a freeway study using UF-ATOFMS. *Atmospheric Environment*
2237 **2007**, doi:10.1016/j.atmosenv.2007.08.005.

2238 (128) Toner, S. M.; Shields, L. G.; Prather, K. A., Source apportionment of
2239 freeway-side PM_{2.5} using ATOFMS. *Atmospheric Environment* **2007**, submitted for
2240 publication.

2241 (129) Song, X. H.; Hopke, P. K.; Ferguson, D. P.; Prather, K. A., Classification
2242 of single particles analyzed by ATOFMS using an artificial neural network, ART-2A.
2243 *Analytical Chemistry* **1999**, 71(4), 860-865.

2244 (130) *Software toolkit to analyze single-particle mass spectral data -*
2245 <http://www.yaada.org>, 2006.

2246 (131) Kim, E.; Hopke, P. K.; Kenski, D. M.; Koerber, M., Sources of Fine
2247 Particles in a Rural Midwestern U.S. Area. *Environmental Science and Technology* **2005**,
2248 39, (13) 4953-4960.

2249 (132) Zhao, W.; Hopke, P. K., Source identification for fine aerosols in
2250 Mammoth Cave National Park. *Atmospheric Research* **2006**, 80, (4) 309-322.

2251 (133) Ying, Q.; Kleeman, M. J., Source contributions to the regional distribution
2252 of secondary particulate matter in California. *Atmospheric Environment* **2006**, 40, (4)
2253 736-752.

2254 (134) Swietlicki, E.; Puri, S.; Hansson, H.-C.; Edner, H., Urban air pollution
2255 source apportionment using a combination of aerosol and gas monitoring techniques.
2256 *Atmospheric Environment* **1996**, 30, (15) 2795-2809.

2257 (135) Querol, X.; Alastuey, A.; Rodriguez, S.; Plana, F.; Ruiz, C. R.; Cots, N.;
2258 Massague, G.; Puig, O., PM₁₀ and PM_{2.5} source apportionment in the Barcelona
2259 Metropolitan area, Catalonia, Spain. *Atmospheric Environment* **2001**, 35, (36) 6407-6419.

2260 (136) Ward, T.; Rinehart, L.; Lange, T., The 2003/2004 Libby, Montana PM_{2.5}
2261 source apportionment research study. *Aerosol Science and Technology* **2006**, 40, (3) 166-
2262 177.

2263 (137) Park, S. S.; Kim, Y. J., Source contributions to fine particulate matter in an
2264 urban atmosphere. *Chemosphere* **2005**, 59, (2) 217-226.

2265 (138) Pastor, S. H.; Allen, J. O.; Hughes, L. S.; Bhawe, P.; Cass, G. R.; Prather,
2266 K. A., Ambient single particle analysis in Riverside, California by aerosol time-of-flight
2267 mass spectrometry during the SCOS97-NARSTO. *Atmospheric Environment* **2003**, 37,
2268 (Suppl. 2) 239-258.

2269 (139) Liu, D. Y.; Wenzel, R. J.; Prather, K. A., Aerosol time-of-flight mass
2270 spectrometry during the Atlanta Supersite experiment: 1. Measurements. *Journal of*
2271 *Geophysical Research-Atmospheres* **2003**, 108, (D7) 8426.

2272 (140) Dall'Osto, M.; Harrison, R. M., Chemical characterisation of single
2273 airborne particles in Athens (Greece) by ATOFMS. *Atmospheric Environment* **2006**, 40,
2274 (39) 7614-7631.

2275 (141) Moffet, R. C.; de Foy, B.; Molina, L. T.; Molina, M. J.; Prather, K. A.,
2276 Characterization of ambient aerosols in northern Mexico City by single particle mass
2277 spectrometry. *Atmospheric Chemistry and Physics Discussion* **2007**, 7, 6413-6457.

2278 (142) Hodzic, A.; Madronich, S.; Bohn, B.; Massie, S.; Menut, L.; Wiedinmyer,
2279 C., Wildfire particulate matter in Europe during summer 2003: meso-scale modeling of

2280 smoke emissions, transport and radiative effects. *Atmospheric Chemistry and Physics*
2281 **2007**, 7, (15) 4043-4064.

2282 (143) Ault, A. P.; Furutani, H.; Dominguez, G.; Thiemens, M. H.; Prather, K.
2283 A., A mass spectral fingerprint of ship emission particles by aerosol time-of-flight mass
2284 spectrometry and applications for source apportionment. *In Preparation* **2007**.

2285 (144) Metzger, S.; Mihalopoulos, N.; Lelieveld, J., Importance of mineral
2286 cations and organics in gas-aerosol partitioning of reactive nitrogen compounds: case
2287 study based on MINOS results. *Atmospheric Chemistry and Physics* **2006**, 6, (9) 2549-
2288 2567.

2289 (145) Eleftheriadis, K.; Balis, D.; Ziomas, I. C.; Colebeck, I.; Manalis, N.,
2290 Atmospheric aerosol and gaseous species in Athens, Greece. *Atmospheric Environment*
2291 **1998**, 32, (12) 2183-2191.

2292 (146) Papayannis, A.; Balis, D.; Amiridis, V.; Chourdakis, G.; Tsaknakis, G.;
2293 Zerefos, C.; Castanho, A. D. A.; Nickovic, S.; Kazadzis, S.; Grabowski, J.,
2294 Measurements of saharan dust aerosols over the Eastern Mediterranean using elastic
2295 backscatter-Raman lidar, spectrophotometric and satellite observations in the frame of the
2296 EARLINET project. *Atmospheric Chemistry and Physics* **2005**, 5, (8) 2065-2079.

2297 (147) Imhof, D.; Weingartner, E.; Ordonez, C.; Gehrig, R.; Hill, M.; Buchmann,
2298 B.; Baltensperger, U., Real-world emission factors of fine and ultrafine aerosol particles
2299 for different traffic situations in Switzerland. *Environmental Science and Technology*
2300 **2005**, 39, (21) 8341-8350.

2301 (148) Kittelson, D. B.; Watts, W. F.; Johnson, J. P.; Schauer, J. J.; Lawson, D.
2302 R., On-road and laboratory evaluation of combustion aerosols-Part 2: Summary of spark
2303 ignition engine results. *Journal of Aerosol Science* **2006**, 37, (8) 931-949.

2304 (149) Zhao, W.; Hopke, P. K., Source apportionment for ambient particles in the
2305 San Gorgonio wilderness. *Atmospheric Environment* **2004**, 38, (35) 5901-5910.

2306 (150) Hu, C.-W.; Chao, M.-R.; Wu, K.-Y.; Chang-Chien, G.-P.; Lee, W.-J.;
2307 Chang, L. W.; Lee, W.-S., Characterization of multiple airborne particulate metals in the
2308 surroundings of a municipal waste incinerator in Taiwan. *Atmospheric Environment*
2309 **2003**, 37, (20) 2845-2852.

2310 (151) Kanias, G. D.; Viras, L. G.; Grimanis, A. P., Source identification of trace
2311 elements emitted into Athens atmosphere. *Journal of Radioanalytical and Nuclear*
2312 *Chemistry* **2004**, 260, (3) 509-518.

2313 (152) Vassilakos, C.; Veros, D.; Michopoulos, J.; Maggos, T.; O'Connor, C. M.,
2314 Estimation of selected heavy metals and arsenic in PM10 aerosols in the ambient air of
2315 the Greater Athens Area, Greece. *Journal of Hazardous Materials* **2007**, 140, (1-2) 389-
2316 398.

2317 (153) Karageorgos, E. T.; Rapsomanikis, S., Chemical characterization of the
2318 inorganic fraction of aerosols and mechanisms of the neutralization of atmospheric
2319 acidity in Athens, Greece. *Atmospheric Chemistry and Physics* **2007**, 7, (11) 3015-3033.

2320 (154) Valavanidis, A.; Fiotakis, K.; Vlahogianni, T.; Bakeas, E. B.;
2321 Triantafyllaki, S.; Paraskevopoulou, V.; Dassenakis, M., Characterization of atmospheric
2322 particulates, particle-bound transition metals and polycyclic aromatic hydrocarbons of
2323 urban air in the center of Athens (Greece). *Chemosphere* **2006**, 65, (5) 760-768.

2324 (155) Scheff, P. A.; Valiozis, C., Characterization and source identification of
2325 respirable particulate matter in Athens, Greece. *Atmospheric Environment, Part A:*
2326 *General Topics* **1990**, *24A*, (1) 203-211.

2327 (156) Guazzotti, S. A.; Suess, D. T.; Coffee, K. R.; Quinn, P. K.; Bates, T. S.;
2328 Wisthaler, A.; Hansel, A.; Ball, W. P.; Dickerson, R. R.; Neususs, C.; Crutzen, P. J.;
2329 Prather, K. A., Characterization of carbonaceous aerosols outflow from India and Arabia:
2330 biomass/biofuel burning and fossil fuel combustion. *Journal of Geophysical Research,*
2331 *[Atmospheres]* **2003**, *108*, (D15) ACL13/11-ACL13/14.

2332 (157) Sodeman, D. A.; Toner, S. M.; Prather, K. A., Determination of single
2333 particle mass spectral signatures from light duty vehicle emissions. *Environmental*
2334 *Science & Technology* **2005**, *39*, (12) 4569-4580.

2335 (158) Guazzotti, S. A.; Whiteaker, J. R.; Suess, D.; Coffee, K. R.; Prather, K. A.,
2336 Real-time measurements of the chemical composition of size-resolved particles during a
2337 Santa Ana wind episode, California USA. *Atmospheric Environment* **2001**, *35*, (19) 3229-
2338 3240.

2339 (159) Qin, X.; Prather, K. A., Impact of biomass emissions on particle chemistry
2340 during the California Regional Particulate Air Quality Study. *International Journal of*
2341 *Mass Spectrometry* **2006**, *258*, (1-3) 142-150.

2342 (160) Formenti, P.; Elbert, W.; Maenhaut, W.; Haywood, J.; Andrae, M. O.,
2343 Chemical composition of mineral dust aerosol during the Saharan Dust Experiment
2344 (SHADE) airborne campaign in the Cape Verde region, September 2000. *Journal of*
2345 *Geophysical Research, [Atmospheres]* **2003**, *108*, (D18) SAH 3/1-SAH 3/15.

2346 (161) Ganor, E., The composition of clay minerals transported to Israel as
2347 indicators of Saharan dust emission. *Atmospheric Environment, Part A: General Topics*
2348 **1991**, *25A*, (12) 2657-2664.

2349 (162) Fast, J. D.; de Foy, B.; Rosas, F. A.; Caetano, E.; Carmichael, G.;
2350 Emmons, L.; McKenna, D.; Mena, M.; Skamarock, W.; Tie, X.; Coulter, R. L.; Barnard,
2351 J. C.; Wiedinmyer, C.; Madronich, S., A meteorological overview of the MILAGRO field
2352 campaigns. *Atmospheric Chemistry and Physics* **2007**, *7*, (9) 2233-2257.

2353 (163) Salcedo, D.; Onasch, T. B.; Dzepina, K.; Canagaratna, M. R.; Zhang, Q.;
2354 Huffman, J. A.; DeCarlo, P. F.; Jayne, J. T.; Mortimer, P.; Worsnop, D. R.; Kolb, C. E.;
2355 Johnson, K. S.; Zuberi, B.; Marr, L. C.; Volkamer, R.; Molina, L. T.; Molina, M. J.;
2356 Cardenas, B.; Bernabe, R. M.; Marquez, C.; Gaffney, J. S.; Marley, N. A.; Laskin, A.;
2357 Shutthanandan, V.; Xie, Y.; Brune, W.; Leshner, R.; Shirley, T.; Jimenez, J. L.,
2358 Characterization of ambient aerosols in Mexico City during the MCMA-2003 campaign
2359 with aerosol mass spectrometry: results from the CENICA Supersite. *Atmospheric*
2360 *Chemistry and Physics* **2006**, *6*, (4) 925-946.

2361 (164) Chow, J. C.; Watson, J. G.; Crow, D.; Lowenthal, D. H.; Merrifield, T.,
2362 Comparison of IMPROVE and NIOSH carbon measurements. *Aerosol Science &*
2363 *Technology* **2001**, *34*, (1) 23-34.

2364 (165) Doran, J. C.; Barnard, J. C.; Arnott, W. P.; Cary, R.; Coulter, R.; Fast, J.
2365 D.; Kassianov, E. I.; Kleinman, L.; Laulainen, N. S.; Martin, T.; Paredes-Miranda, G.;
2366 Pekour, M. S.; Shaw, W. J.; Smith, D. F.; Springston, S. R.; Yu, X. Y., The T1-T2 study:
2367 evolution of aerosol properties downwind of Mexico City. *Atmospheric Chemistry and*
2368 *Physics* **2007**, *7*, (6) 1585-1598.

2369 (166) Volkamer, R.; Jimenez, J. L.; San Martini, F.; Dzepina, K.; Zhang, Q.;
2370 Salcedo, D.; Molina, L. T.; Worsnop, D. R.; Molina, M. J., Secondary organic aerosol
2371 formation from anthropogenic air pollution: rapid and higher than expected. *Geophysical*
2372 *Research Letters* **2006**, *33*, (17) L17811/17811-L17811/17814.

2373 (167) Zavala, M.; Herndon, S. C.; Slott, R. S.; Dunlea, E. J.; Marr, L. C.;
2374 Shorter, J. H.; Zahniser, M.; Knighton, W. B.; Rogers, T. M.; Kolb, C. E.; Molina, L. T.;
2375 Molina, M. J., Characterization of on-road vehicle emissions in the Mexico City
2376 Metropolitan Area using a mobile laboratory in chase and fleet average measurement
2377 modes during the MCMA-2003 field campaign. *Atmospheric Chemistry and Physics*
2378 **2006**, *6*, 5129-5142.

2379 (168) Baumgardner, D.; Raga, G. B.; Kok, G.; Ogren, J.; Rosas, I.; Baez, A.;
2380 Novakov, T., On the evolution of aerosol properties at a mountain site above Mexico
2381 City. *Journal of Geophysical Research-Atmospheres* **2000**, *105*, (D17) 22243-22253.

2382 (169) Moya, M.; Grutter, M.; Baez, A., Diurnal variability of size-differentiated
2383 inorganic aerosols and their gas-phase precursors during January and February of 2003
2384 near downtown Mexico City. *Atmospheric Environment* **2004**, *38*, (33) 5651-5661.

2385 (170) Chow, J. C.; Watson, J. G.; Edgerton, S. A.; Vega, E., Chemical
2386 composition of PM_{2.5} and PM₁₀ in Mexico City during winter 1997. *Science of the Total*
2387 *Environment* **2002**, *287*, (3) 177-201.

2388 (171) Vega, E.; Mugica, V.; Reyes, E.; Sanchez, G.; Chow, J. C.; Watson, J. G.,
2389 Chemical composition of fugitive dust emitters in Mexico City. *Atmospheric*
2390 *Environment* **2001**, *35*, (23) 4033-4039.

2391 (172) San Martini, F. M.; Dunlea, E. J.; Volkamer, R.; Onasch, T. B.; Jayne, J.
2392 T.; Canagaratna, M. R.; Worsnop, D. R.; Kolb, C. E.; Shorter, J. H.; Herndon, S. C.;
2393 Zahniser, M. S.; Salcedo, D.; Dzepina, K.; Jimenez, J. L.; Ortega, J. M.; Johnson, K. S.;
2394 McRae, G. J.; Molina, L. T.; Molina, M. J., Implementation of a Markov Chain Monte
2395 Carlo method to inorganic aerosol modeling of observations from the MCMA-2003
2396 campaign - Part II: model application to the CENICA, Pedregal and Santa Ana sites.
2397 *Atmospheric Chemistry and Physics* **2007**, *6*, (12, Pt. 3) 4889-4904.

2398 (173) Robinson, A. L.; Subramanian, R.; Donahue, N. M.; Bernardo-Bricker, A.;
2399 Rogge, W. F., Source apportionment of molecular markers and organic aerosol. 3. Food
2400 cooking emissions. *Environmental Science & Technology* **2006**, *40*, (24) 7820-7827.

2401 (174) Rogge, W. F.; Hildemann, L. M.; Mazurek, M. A.; Cass, G. R.; Simoneit,
2402 B. R. T., Sources of fine organic aerosol. 1. Charbroilers and meat cooking operations.
2403 *Environmental Science and Technology* **1991**, *25*, (6) 1112-1125.

2404 (175) Shields, L. G.; Suess, D. T.; Prather, K. A., Determination of single
2405 particle mass spectral signatures from heavy duty diesel vehicle emissions for PM_{2.5}
2406 source apportionment. *Atmospheric Environment* **2007**, *41*, (18) 3841-3852.

2407 (176) Noble, C. A.; Prather, K. A., Real-time measurement of correlated size
2408 and composition profiles of individual atmospheric aerosol particles. *Environmental*
2409 *Science and Technology* **1996**, *30*, (9) 2667-2680.

2410 (177) Tolocka, M. P.; Lake, D. A.; Johnston, M. V.; Wexler, A. S., Number
2411 concentrations of fine and ultrafine particles containing metals. *Atmospheric Environment*
2412 **2004**, *38*, (20) 3263-3273.

2413 (178) Hsieh, Y. M.; Tsai, M. S., Physical and chemical analyses of unburned
2414 carbon from oil-fired fly ash. *Carbon* **2003**, *41*, (12) 2317-2324.

2415 (179) Suarez, A. E.; Ondov, J. M., Ambient aerosol concentrations of elements
2416 resolved by size and by source: Contributions of some cytokine-active metals from coal-
2417 and oil-fired power plants. *Energy & Fuels* **2002**, *16*, (3) 562-568.

2418 (180) Wenzel, R. J.; Liu, D.-Y.; Edgerton, E. S.; Prather, K. A., Aerosol time-of-
2419 flight mass spectrometry during the Atlanta Supersite Experiment: 2. Scaling procedures.
2420 *Journal of Geophysical Research, [Atmospheres]* **2003**, *108*, (D7) SOS 15/11-SOS 15/18.

2421 (181) Buzcu-Guven, B.; Brown Steven, G.; Frankel, A.; Hafner Hilary, R.;
2422 Roberts Paul, T., Analysis and apportionment of organic carbon and fine particulate
2423 matter sources at multiple sites in the midwestern United States. *Journal of the Air &*
2424 *Waste Management Association* **2007**, *57*, (5) 606-619.

2425 (182) Kleinman, L. I.; Daum, P. H.; Lee, Y.-N.; Senum, G. I.; Springston, S. R.;
2426 Wang, J.; Berkowitz, C.; Hubbe, J.; Zaveri, R. A.; Brechtel, F. J.; Jayne, J.; Onasch, T.
2427 B.; Worsnop, D., Aircraft observations of aerosol composition and ageing in New
2428 England and Mid-Atlantic States during the summer 2002 New England Air Quality
2429 Study field campaign. *Journal of Geophysical Research, [Atmospheres]* **2007**, *112*, (D9)
2430 D09310/09311-D09310/09318.

2431 (183) Williams, B. J.; Goldstein, A. H.; Millet, D. B.; Holzinger, R.; Kreisberg,
2432 N. M.; Hering, S. V.; White, A. B.; Worsnop, D. R.; Allan, J. D.; Jimenez, J. L.,
2433 Chemical speciation of organic aerosol during the International Consortium for
2434 Atmospheric Research on Transport and Transformation 2004: results from in situ
2435 measurements. *Journal of Geophysical Research, [Atmospheres]* **2007**, *112*, (D10)
2436 D10S26/11-D10S26/14.

2437 (184) Weber, R. J.; Sullivan, A. P.; Peltier, R. E.; Russell, A.; Yan, B.; Zheng,
2438 M.; de Gouw, J.; Warneke, C.; Brock, C.; Holloway, J. S.; Atlas, E. L.; Edgerton, E., A
2439 study of secondary organic aerosol formation in the anthropogenic-influenced
2440 Southeastern United States. *Journal of Geophysical Research, [Atmospheres]* **2007**, *112*,
2441 (D13) D13302/13301-D13302/13313.

2442 (185) Zhang, Q.; Worsnop, D. R.; Canagaratna, M. R.; Jimenez, J. L.,
2443 Hydrocarbon-like and oxygenated organic aerosols in Pittsburgh: Insights into sources
2444 and processes of organic aerosols. *Atmospheric Chemistry and Physics* **2005**, *5*, (12)
2445 3289-3311.

2446 (186) Pratt, K. A.; Prather, K. A., Real-time, single-particle volatility, size, and
2447 chemical composition measurements of aged urban aerosols. *Environ. Sci. Technol.* **2009**,
2448 *In Preparation*.

2449
2450
2451

2452 **E. Publications produced**

- 2453 1. Gaston, C. J.; Pratt, K. A.; Qin, X. Y.; Prather, K. A., Real-Time Detection and
2454 Mixing State of Methanesulfonate in Single Particles at an Inland Urban Location during
2455 a Phytoplankton Bloom. *Environ. Sci. Technol.* **2010**, *44*, (5) 1566-1572.
- 2456 2. Pratt, K. A.; Prather, K. A., Real-Time, Single-Particle Volatility, Size, and
2457 Chemical Composition Measurements of Aged Urban Aerosols. *Environ. Sci. Technol.*
2458 **2009**, *43*, (21) 8276-8282.